UNIVERSITY OF NAPLES FEDERICO II

Thesis submitted for the Degree of Doctor of Philosophy on

PHARMACEUTICAL SCIENCE

XXVIII cycle

Coordinator: Prof. Maria Valeria D'Auria

BIOENGINEERED POROUS SILICA DEVICES FOR BIOMEDICAL APPLICATIONS

Dr. Monica Terracciano

Supervisor: Ilaria Rea, PhD

Nicola Borbone, PhD

Naples, Italy

March, 2016

"Non est quod timeas ne operam perdideris, si tibi didicisti."

L. A. Seneca

ACKNOWLEDGEMENTS

I would like to extend my sincere gratitude to my supervisor Dr. Ilaria Rea for all her trust, constant support and valuable guidance. Her positive attitude towards life and science made my PhD a great experience.
I am also very grateful to my supervisor Dr. Nicola Borbone for his scientific support and guidance.
My appreciation to Professor Maria Valeria D'Auria, coordinator of the Doctoral School, for her kindness.
I would like to express my deepest grateful to Dr. Luca De Stefano for all his trust, enthusiastic encouragement, kindly support and precious advice.
My grateful thanks to the director Dr. Mario Iodice, Dr. Ivo Rendina, all the researchers and colleagues of the Institute for Microelectronics and Microsystems of National Research Council for the pleasant working atmosphere, especially, Dr. Annalisa D'Arco and Dr. Maurizio Indolfi for their precious support and friendship.
My sincere gratitude to the research group of Professor Gennaro Piccialli of the Department of Pharmacy, and the group of Professor Annalisa Lamberti of the Department of Molecular Medicine and Medical Biotechnology for their remarkable scientific input and collaboration during my PhD work.
I would like to thank Dr. Claudia Tortiglione and Dr. Angela Tino of the Institute of Applied Science and Intelligent Systems of National Research Council for their important suggestions and help with *in vivo* experiments.
Special thanks to Dr. Hèlder A. Santos of the Division of Pharmaceutical Chemistry and Technology of University of Helsinki, for his scientific enthusiasm, valuable suggestions and support during my time at Helsinki.
My heartfelt thanks go to my family and Giovanni for their trust, precious understanding and encouragement. I would not have made it this far without their fundamental support.

Monica Terracciano

ABSTRACT

This thesis summaries three years of research on the development of innovative porous silica based devices for biosensing and drug delivery purposes. Porous silicon (PSi), is one of most exploited nanostructured material in biomedicine. Due to its optical and electrical properties, high specific surface area, tailorable morphology and surface chemistry, PSi is an ideal transducer material for the realization of high sensitive and selective biosensors. In this work, different porous silica structures have been explored for the development of label-free oligonucleotide-biosensor realized by *in situ* synthesis of bioprobe on porous platform. Different functionalization strategies have been also explored in order to make PSi surface more chemically stable. The realization of label-free aptamer-PSi sensor, with great stability, fast response time, high sensitivity and specificity for the detection of human α-thrombin, has been successfully demonstrated. Diatomite, an emerging natural porous silica material of sedimentary origin, with similar physiochemical properties of man-made porous silicon, has been also exploited as potential platform for biomedical applications. Its non-toxicity, biocompatibility, high specific surface area, tailorable surface chemistry, as well as thermal and chemical stability make diatomite a viable cheap surrogate to synthetic porous silica for realization of nano-based drug delivery system. In this thesis work the potentialities of diatomite nanoparticles (DNPs) as safe nanovectors for drug delivery in cancer cells have been successfully demonstrated. Since the silica surface of diatomite is covered by silanol groups, it can be easily modified with functional reactive groups for the conjugation of biomolecules (e.g., DNA, antibodies, enzymes) in order to realize advanced healthcare devices. Different approaches of functionalization based on covalent bond for preparation of bioengineered diatomite NPs for therapeutic molecules transport into cancer cells were developed. Preliminary *in vitro* and *in vivo* studies endorsed this cheap, natural and biocompatible nanomaterial for drug delivery applications.

LIST OF PUBLICATIONS

The following papers have been published on the results described in this thesis.

Journals

J1. L. De Stefano, G. Oliviero, J. Amato, N. Borbone, G. Piccialli, L. Mayol, I. Rendina, **M. Terracciano**, I. Rea, "Aminosilane functionalizations of mesoporous oxidized silicon for oligonucleotide synthesis and detection", *Journal of The Royal Society Interface* **83**, 20130160 (2013).

J2. M. Terracciano, I. Rea, J. Politi, L. De Stefano, "Optical characterization of aminosilane-modified silicon dioxide surface for biosensing", *Journal of the European Optical Society Rapid Publications* **8**,13075 (2013).

J3. M. Terracciano, I. Rea, L. De Stefano, I. Rendina, G. Oliviero, F. Nici, S. D' Errico, G. Piccialli, N. Borbone, "Synthesis of mixed-sequence oligonucleotides on mesoporous silicon: chemical strategies and material stability", *Nanoscale Research Letters* **1,** 317 (2014).

J4. I. Rea, L. Sansone, **M. Terracciano**, L. De Stefano, P. Dardano, M. Giordano, A. Borriello, M. Casalino, "Photoluminescence of graphene oxide infiltrated into mesoporous silicon", *The Journal of Physical Chemistry C* **118**, 27301 (2014).

J5. I. Ruggiero, **M. Terracciano**, N. M. Martucci, L. De Stefano, N. Migliaccio, R. Tatè, I. Rendina, P. Arcari, A. Lamberti, I. Rea, "Diatomite silica nanoparticles for drug delivery", *Nanoscale Research Letters* **1**,329 (2014).

J6. I. Rea, N. M. Martucci, L. De Stefano, I. Ruggiero, **M. Terracciano**, P. Dardano, N. Migliaccio, P. Arcari, R. Tatè, I. Rendina, A. Lamberti, "Diatomite biosilica nanocarriers for siRNA transport inside cancer cells", *Biochimica et Biophysica Acta* **12**, 1840 (2014).

J7. N. M. Martucci, I. Rea, I. Ruggiero, **M. Terracciano**, L. De Stefano, N. Migliaccio, C. Palmieri, G. Scala, P. Arcari, I. Rendina, A. Lamberti, "A new strategy for label-free detection of lymphoma cancer cells", *Biomedical Optics Express* **6**, 1353 (2015).

J8. M. Terracciano, M. A. Shahbazi, A. Correia, I. Rea, A. Lamberti, L. De Stefano, H. A. Santos, "Surface bioengineering of diatomite based nanovectors for efficient intracellular uptake and drug delivery", *Nanoscale* **47**, 20063 (2015).

J9. Q. Shabir, **M. Terracciano**, K. Webb, E. Caffull, I. Rea, D. K. Nadarassan, L. De Stefano, A. Loni, L. T. Canham. "Quantification and reduction of the residual chemical reactivity of passivated biodegradable porous silicon for drug delivery applications", *Silicon* (2016), in press.

J10. J. Politi, I. Rea, F. Nici, P. Dardano, **M. Terracciano**, G. Oliviero, N. Borbone, G. Piccialli, L. De Stefano, "Nanogravimetric and optical characterizations of thrombin interaction with a self-assembled thiolated aptamer", *Journal of Sensors* (2016), in press.

Proceedings

P1. I. Rea, A. Caliò, **M. Terracciano**, J. Politi, L. De Stefano, "Porous silicon based photonic structures for optical monitoring of biochemical interactions", IEEE Conference Publications: Photonics Technologies, AEIT Italian Conference, May 21–23 2013, Milan, Italy.

P2. **M. Terracciano**, L. De Stefano, I. Rendina, G. Oliviero, G. Piccialli, N. Borbone, I. Rea, "Aminosilane-modified mesoporous oxidized silicon for in situ oligonucleotides synthesis and detection", IEEE Conference Publications: Photonics Technologies, AEIT Italian Conference, May 12–14 2014, Naples, Italy.

P3. N. M. Martucci, I. Rea, N. Migliaccio, I. Ruggiero, **M. Terracciano**, R. Tatè, L. De Stefano, I. Rendina, P. Arcari, A. Lamberti, "Diatomite nanoparticles as new promising biocompatible nanomaterial for drug delivery", Extended Abstracts of International Conference and Exhibition on Pharmaceutics and Novel Drug Delivery Systems, March 16–18 2015, Crowner Plaza, Dubai, UAE.

P4. M. Casalino, I. Rea, L, Sansone, **M. Terracciano**, L. De Stefano, P. Dardano, M. Giordano, A. Borriello, G. Coppola, I. Rendina, "Photoluminescence of graphene oxide integrated with silicon substrates", Proc. SPIE Optics and Optoelectronics, April 13–16 2015, Prague, Czech Republic.

P5. N. M. Martucci, I. Rea, I. Ruggiero, **M. Terracciano**, L. De Stefano, N. Migliaccio, P. Dardano, I. Rendina, A. Lamberti, "A silicon-based peptide biosensor for label-free detection of cancer cells", Proc. SPIE Optics and Optoelectronics, April 13–16 2015, Prague, Czech Republic.

P6. I. Rea, L. Sansone, **M. Terracciano**, L. De Stefano, P. Dardano, M. Giordano, A. Borriello, M. Casalino, "Graphene oxide-based mesoporous silicon as tunable platform for optical applications", IET Conference Publications: Photonics Technologies, AEIT Italian Conference, May 6–9 2015, Turin, Italy.

P7. **M. Terracciano**, A. Lamberti, H. A. Santos, N. M. Martucci, M. A. Shahbazi, A. Correira, I. Ruggiero, I. Rendina, L. De Stefano, I. Rea, "Diatomite nanoparticles as potential drug delivery systems", IEEE Conference Publications: International Conference BioPhotonics, May 20–22 2015, Florence, Italy.

P8. I. Rea, **M. Terracciano**, J. Politi, A. Caliò, P. Dardano, M. Gioffrè. A. Lamberti, I. Rendina. L. De Stefano, "Natural and synthetic nanostructured materials for biomedical applications", IEEE Conference Publications: AEIT International Annual Conference, October 14–16 2015, Naples.

Book Chapter

B1. L. De Stefano, I. Rea, A. Caliò, **M. Terracciano**, J. Politi, G. Korotcenkov, "Porous Silicon-based Optical Chemical Sensors." Porous Silicon: from Formation to Application: Biomedical and Sensor Applications (2015).

B2. N. M. Martucci, I. Rea, I. Ruggiero, **M. Terracciano**, L. De Stefano, N. Migliaccio, P. Arcari, I. Rendina, A. Lamberti "Bioengineered surfaces for real time label-free detection of

cancer cells" Lab-on-a-Chip: InTech Open Access Publisher (2016).

B3. M. Terracciano, L. De Stefano, H. A. Santos, N. M. Martucci, A. Tino, I. Ruggiero, I. Rendina, N. Migliaccio, C. Tortiglione, A. Lamberti, I. Rea. "Silica-based nanovectors: from Mother Nature to biomedical applications" Algae Biotechnology: InTech Open Access Publisher (2016).

TABLE OF CONTENTS

1 INTRODUCTION

1.1 Nanostructured porous silicon based devices for biomedical applications

Nanotechnology has allowed the development of innovative nanostructured materials characterized by enhanced properties with respect to their correspondent bulk materials. In recent years, nanomaterials have been used for a wide range of applications, including electronics, medicine, food, pharmaceutics, energy production, consumer products, and so on [1–3]. Application of nanostructured materials in biomedicine offers several advantages compared to traditional materials, due to the possibility to radically change and tune their physicochemical properties [4]. For example, the porosification of materials at the nanoscale results in the enhancement of their biochemical properties such as bioactivity, biocompatibility, avoiding the triggering of immune responses and inflammatory processes into human body, typical of bulk materials [5]. Over the last decades, several types of organic, inorganic and natural materials have been used for biomedical applications. One of these that has highly impacted biomedical field is porous silicon (PSi) [6]. PSi obtained by electrochemical etching of doped crystalline silicon, is one of the most exploited synthetic nanostructured material due to its peculiar properties [5, 6]. Morphology, pore size and surface chemistry can be easily changed and controlled, making it a very versatile material [7]. Due to its optical and electrical properties, and to its sponge-like morphology characterized by a high specific surface area, PSi has been largely used in fabrication of innovative biosensors [8–11]. Moreover, thermal stability, chemical inertness, biocompatibility, high loading capability, adaptable dissolution kinetic, made this material suitable for development of nanodevices for drug delivery applications [5, 12, 13]. In recent years, emerging natural porous materials have also been suggested to overcome the shortcomings of synthetic porous materials, finding in diatomite one of the most outstanding surrogate [14]. Diatomite, also known as diatomaceous earth, is a fossil material of sedimentary origin formed over centuries by siliceous skeleton (called “frustule”) of aquatic unicellular microalgae diatoms, with similar physicochemical properties of man-made fabricated PSi [15, 16]. The unique properties of this inexpensive material have found application in several fields including optics, photonics, sensing, biosensing, filtration, immunoprecipitation, microfluidics, catalysis and nanofabrication [17–21]. Due to ordered pore structure, high surface area, tailorable surface chemistry, high permeability, biocompatibility, non-toxicity, low cost, low density, optical and photonic properties, diatomite has been exploited as an innovative platform in several biotechnological

applications resulting as a viable and promising cheap alternative to synthetic porous silica [14, 22, 23].

1.2 Synthetic oligonucleotides for bioengineering of nanostructured devices

Surface modification of nanostructured devices with biomolecules (i.e., bioengineering) is one of the most challenging and fastest growing component of nanotechnology, which transforms inert materials in advanced ones for medical purpose. [24]. Among different biomolecules used for this function (i.e., enzymes, proteins, antibodies, peptides) DNA and its derivatives, are considered suitable as construction materials in nanoscience due to their peculiar properties [25]. DNA is a double stranded helical molecule, that can be separated into single-stranded DNA (ssDNA) units complementary to one other. When these ssDNA structures are brought together, they form again the duplex structure. Despite its simplicity, the enormous specificity of the adenine–thymine (A–T) and guanine–cytosine (G–C) Watson–Crick hydrogen bonding allows the development of high selective bioprobes for the development of specific DNA-devices. The power of DNA as a molecular tool is enhanced by the ability to synthesize DNA sequences with peculiar properties by automated methods [26]. Engineered synthetic nucleic acids, different from the canonical DNA can fold into various other secondary structures such as G-quadruplexes [27]. G-quadruplexes are unusual nucleic acids that can form within specific repetitive G rich DNA or RNA sequences, characterized by the stacking of units (G-tetrads), consisting of four guanines organized in a square planar arrangement. Each guanine is linked to the two adjacent ones by Hoogsteen hydrogen bonds, involving the amino and imino protons and the nitrogen N7 and oxygen O6 atoms (Figure 1.1). Many reports suggest that G-quadruplex structures have important applications in several and different areas, ranging from medicinal chemistry to the nanotechnologies [28, 29]. An interesting property of G-quadruplex structures is that they may serve as scaffold of aptamers. Aptamers are an emerged class of single-stranded RNA or DNA oligonucleotides able to fold into well specific three-dimensional (3D) structures, generated from SELEX technique [30, 31]. This process relying on DNA or RNA libraries allows automatic synthesis of a large variety of nucleic acid sequences with great selectivity for non-nucleic acids molecules. In contrast to other nucleic acid molecules, aptamers are able to interact with their targets through a structural recognition similar to an antibody-antigen reaction with dissociation constant in the range of pico- to nano-molar, thus referred to as chemical antibodies [32].

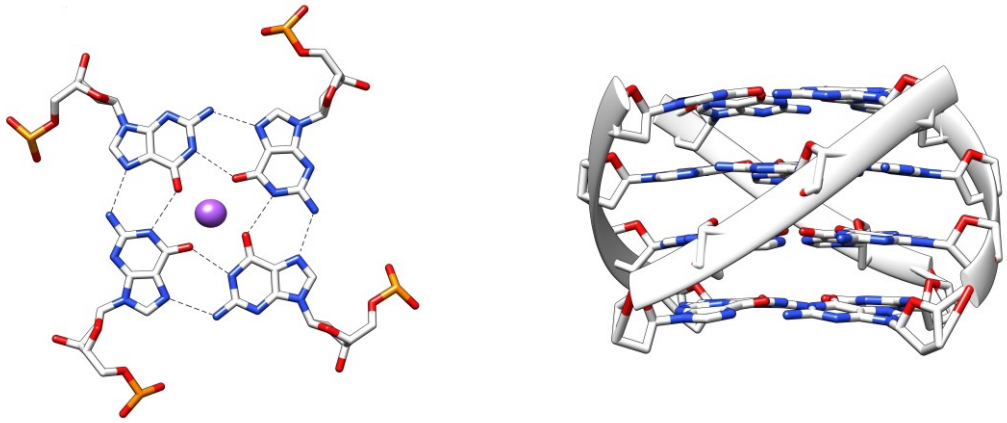

Fig. 1.1. *Graphical representation of a G-tetrad and a G-quadruplex.*

However, different from antibodies, the chemical nature of nucleic acids allows easy synthesis and various feasible ways to engineer aptamers with extended bioavailability, regulating ability, and multi-functional properties. Aptamers can be easily obtained by automatic synthesis with good reproducibility contrary to antibodies which are obtained by *in vivo* immunization of animals. [30–32]. Aptamers are thermally stable, even after a 95 °C denaturation they can refold into their correct 3D conformation once cooled to room temperature, unlike protein-based antibodies which permanently lose their activity at high temperatures [30]. The targets of aptamers range from small molecules, to proteins, virus-infected cells, stem cells, and cancer cells. Chemical features and biological functions have made aptamers a very attractive tool in biomedical applications ranging from bioassays to targeted therapy. Moreover, aptamer technology has shown a great potential for bioengineering of nanostructured devices. In the past few years, integration of functional aptamers into nanomaterials has become a new interdisciplinary field that aims at providing new hybrid sensing systems for specific and sensitive molecular recognition [33, 34]. Aptamer used as bioprobe for the development of biosensor, opened new generation of DNA biosensors called aptasensors [35]. Due to their unique properties, aptamers hold many advantages over antibodies, which have been widely used as recognition elements in biosensing. To date, aptamer-based biosensors have successfully detected a large number of analytes of interest, including small organic molecules, metal ions, and proteins, by taking advantages of the highly selective interactions of the aptamer with the target analytes and high signals amplification by the unique optical, electrical, and magnetic properties of various sensing platform used [35]. This novel integration, highlighted the potentiality of aptamers as

emerging tools for fabrication of new sensing devices for selective and sensitive detection of a wide range of analytes with great advances in healthcare applications.

1.3 Porous silica optical biosensors for human disease diagnosis

A growing need for small, fast, efficient and portable devices able to detect a specific analyte has meant biosensing one of the most rapidly expanding research field, ranging from a broad of applications including clinical diagnostics, environmental monitoring, veterinary and food quality control. A biosensor is an hybrid device constituted by a biomolecular probe, employed to selectively recognize a biochemical target, immobilized on a transducer surface which converts the target recognition into an analytical signal [36–38]. The porous silicon (PSi) obtained by electrochemical partial dissolution of doped crystalline silicon, is by far one of the most intriguing optical transducer for developing of a wide variety of chemical and biological sensors [6, 7]. The potential application of the PSi structures to molecular screening for biomedical applications has gained widespread attention of scientific community, as demonstrated by several papers which proved the potentiality of PSi-based biosensors to detect analytes in heterogeneous mixture and in low concentrations [39]. PSi biosensors are label-free devices relying on electrical, electrochemical and optical mechanisms [40–42]. Optical biosensors are the most prevalent PSi biosensors, characterized by very short analysis time and high sensitivity. Moreover, opto-instruments used for measurements are non-invasive and safe also in harsh conditions such as *in vivo* monitoring inside a patient body where, for example, electrical-based devices could be harmful [43]. The label-free sensing mechanism of PSi optical structures is based on the change of their refractive index on exposure to the substances to be detected, due to their infiltration in the pores and air replacement. The consequence of the refractive index variation is a change in the reflectivity spectrum of the device (Figure 1.2). The selectivity of PSi device is obtained by a proper chemical surface functionalization (i.e., covalent immobilization) with biomolecular probes able to detect the target molecule from a complex mixture. The achievement of PSi as biosensor depends on the stability of its surface chemistry. Unfortunately, the freshly prepared hydrogen terminated (Si–H) PSi structures suffer instability in ambient air and aqueous solutions due to an uncontrolled oxidation of the surface [44]. The uncontrolled oxidation of PSi is a major problem in biosensor development, due to the continuous change in the refractive index of device which falsifies the signal transduction [45]. Many thermal and chemical strategies have been developed to stabilize PSi, thus preserving its optical properties for biosensing.

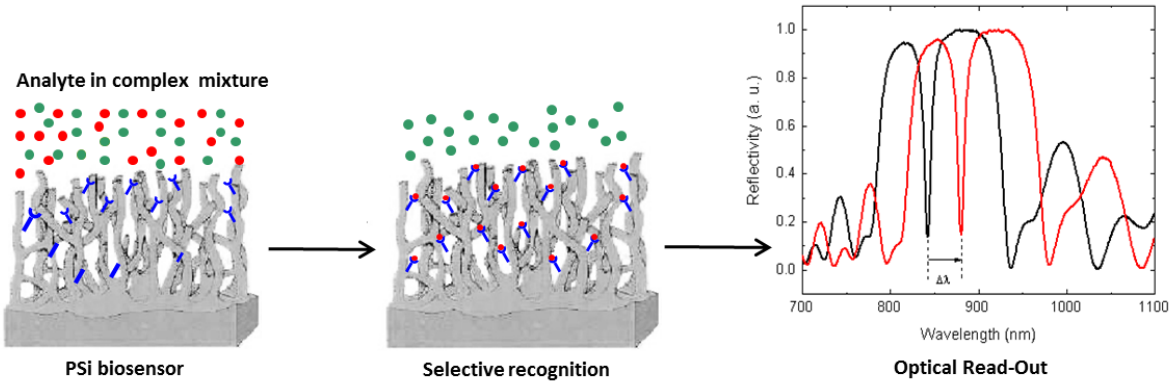

Fig. 1.2. *Scheme of label-free sensing mechanism of PSi optical biosensor.*

Once passivated the PSi surface, the functionalization with biomolecular probes can be achieved, thus realizing a specific biosensor. Chapter 2, based on preliminary studies for the development of DNA-PSi biosensor by *in situ* solid phase oligonucleotides (ON) synthesis, describes the fabrication process, passivation and characterization of mesoporous silicon based oligonucleotide sensor. Since the chemistry used for the solid phase synthesis and deprotection of ON is quite aggressive for the PSi supports, the surface was stabilized by a thermal oxidation followed by a silanization. The *in situ* synthesis of single-stranded polythymine ON bioprobe, has been used as strategy to biofunctionalize the transducer's surface. The advantages of *in situ* synthesis with respect to conventional *ex situ* immobilization are not only the increasing of DNA probe density but also the process automation, and the possibility of surface local functionalization [43]. Finally, the ON deprotection and label-free optical detection of DNA-DNA hybridization with a complementary ON sequence have been demonstrated, thus opening the prospective for the development of more specific DNA-PSi biosensors through solid phase synthesis without any restriction on the ON sequence composition and limitation of PSi surface stability. The development of a PSi aptasensor by *in situ* synthesis of anti-thrombin aptamer (TBA) bioprobe for label-free optical detection of human thrombin, is described in Chapter 3. The TBA is a well characterized chair-like antiparallel quadruplex structure that specifically binds the thrombin. Thrombin, a serine protease, plays important role in the coagulation cascade, thrombosis and haemostasis. The high nanomolar range of thrombin in blood was known to be associated with diseases, therefore, it is important to assess this protein at trace level with high sensitivity. TBA aptamer has been synthetized in macroporous (pore size > 50 nm) amino-modified PSi structure which allowed a correct synthesis of the macroprobe with proper yield, with respect to mesoporous (10 < pore size < 50 nm) one. Further, it was proved

the stability, selectivity, reversibility and low limit of detection of PSi-aptasensor, resulting as a promising device for vascular diseases early diagnosis.

1.4 Diatomite as natural porous silica material for drug delivery

The application of nanotechnology in medicine for human disease diagnosis, treatment, and control of biological systems has been referred to as nanomedicine [46, 47]. This new emerging research field, paving the way for medical innovations, seeks to deliver a valuable set of research tools and clinically helpful nanostructured devices for human health [48, 49]. During the last decades, great efforts have been made in the development of innovative drug delivery systems, thus overcoming the drawbacks of conventional drug therapies [50−52]. Nanoparticle (NP)-based drug delivery systems have provided many advantages over conventional drug formulations such as selective drugs delivery to pathological sites, enhanced solubility of poorly-water soluble drugs, improved pharmacokinetics and short half-lives of degradable molecules (e.g., peptides, proteins, DNA), simultaneous delivery of drugs for combination therapy to reduce the drug resistance. Despite the vast assortment of nanomaterials to develop nanocarriers, porous silicon/silica based devices are the most used drug delivery platforms due to the remarkable properties of this material. The most popular example among them are synthetic mesoporous silica-NPs (MPS-NPs) [53−55]. Due to excellent biocompatibility, high surface area, thermal stability, chemical inertness and diffusion controlled drug-release mechanism, MPS has been considered an ideal material for drug delivery applications [5, 6, 53–55]. However, the synthesis of MPS-NPs is time-consuming and costly, involving high-energy consumption and toxic materials [56]. Therefore, to address some of these disadvantages, it was suggested to explore alternative natural porous silica materials for drug-delivery applications [14, 23]. The cheap fossil compound diatomite appears to be the most outstanding example of 3D structures biologically derived porous silica, given by Mother Nature, as shown in Figure 1.3. Diatomite possesses a combination of structural, mechanical and chemical features that can overcome challenges associated with conventional delivery of therapeutic agents and offer several advantages over existing synthetic delivery systems [14, 15]. Although, due to its peculiar properties diatomite is surprisingly still scarcely used in nanomedicine. In Chapter 4, the realization of silica-based nanoparticles from diatomite powder and the exploration of their potentialities as nanovectors for drug delivery in cancer cells are described. A purification procedure based on thermal treatments in strong acid solutions to make diatomite safer material for medical applications, fabrication techniques to reduce the micrometric diatomite powder to nanoparticles (DNPs),

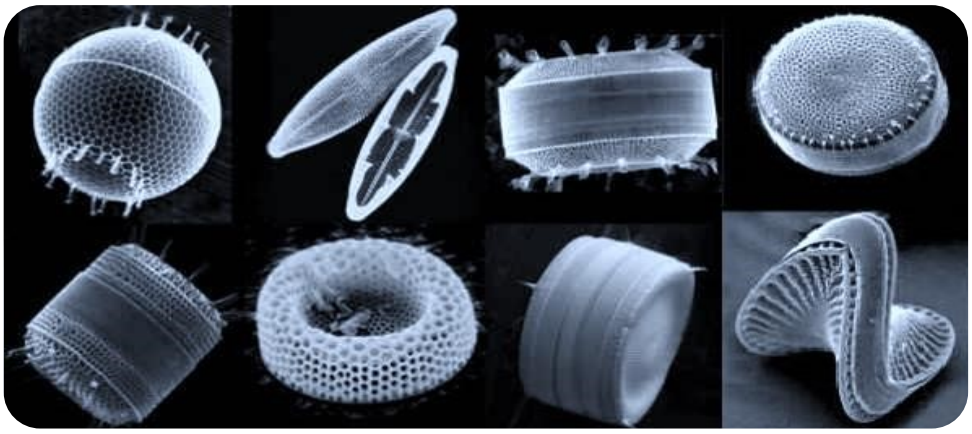

Fig. 1.3. *Frustules from some different diatom algae species.*

morphological and chemical characterization of the nanomaterial, as well as preliminary tests of cytotoxicity and cellular uptake, are presented in detail. Since the silica surface of diatomite is covered by silanol (SiOH) groups, it can be easily modified with functional reactive groups (−NH_2, −COOH, −SH, −CHO) for the conjugation of biomolecules (e.g., DNA, antibodies, enzyme) in order to prepare bioengineered devices. In Chapter 5, different functionalization procedures for the preparation of biofunctionalized DNPs as non-toxic carriers for transport through cellular membranes of therapeutic molecules (i.e., small interfering RNA and sorafenib) and the results on the effective enhancement of the DNPs' physicochemical properties, biocompatibility and cellular uptake, are described. In Chapter 6, a preliminary *in vivo* toxicity study of diatomite NPs was evaluated by using *Hydra vulgaris* as new simple *in vivo* model.

References

1. W. R. Sanhai, J. H. Sakamoto, R. Canady, M. Ferrari, *Nat. Nanotechnol.*, 2008, **3**, 242−244.
2. M. Ineke, C. Emond, *Nanotechnology and Human Health*., CRC Press, 2013.
3. V. Wagner, A. K. Bock, A. Zweck, *Nat Biotechnol*., 2006, **24**, 1211–1217.
4. C. C. Koch, *Nanostructured materials: processing, properties and applications*, William Andrew, 2006.
5. H. A. Santos, *Porous silicon for biomedical applications*, Elsevier, 2014.
6. L. T. Canham, *Properties of porous silicon*, Institution of Electrical Engineers, 1997.
7. M. J. Sailor, *Porous Silicon in practice: preparation, characterization and applications*, John Wiley & Sons, 2012.
8. K. P. S. Dancil, D. P. Greiner, M. J. Sailor, *J. Am. Chem. Soc.*, 1999, **121**, 7925−7930.
9. L. De Stefano, I. Rendina, L. Moretti, A. M. Rossi, *Mater. Sci. Eng. B,* 2003,**100**, 271−274.
10. A. Jane, R. Dronov, A. Hodges, N. H. Voelcker, *Trends Biotechnol*., 2009, **27**, 230−239.
11. J. Salonen, L. Vesa-Pekka, *J. Chem. Eng.*, 2008, **137**, 162−172.
12. L. M. Bimbo, L. Peltonen, J. Hirvonen, H. A. Santos, *Curr. Drug Metab*., 2012, **13**,

1068−1086
13. E. J. Anglin, L. Cheng, W. R. Freeman, M. J. Sailor, *Adv. Drug Deliv. Rev.*, 2008, **60**, 1266−1277.
14. D. Losic, J. G. Mitchell, N. H. Voelcker, *Adv. Mater*., 2009, **21**, 2947−2958.
15. M. S. Aw, S. Simovic, Y. Yu, J. Addai-Mensah, D. Losic, *Powder Technol*., 2012, **223**, 52−58.
16. M. A. Ferrara, P. Dardano, L. De Stefano, I. Rea, G. Coppola, I. Rendina, R. Congestri, A. Antonucci, M. De Stefano, E. De Tommasi, *PLoS ONE*, 2014, **9**, 103750.
17. J. Parkinson, R. Gordon, *Trends Biotechnol.*, 1999, **17**, 230−232.
18. T. Fuhrmann, S. Landwehr, M. El Rharbi-Kucki, M. Sumper, *Appl. Phys. B*, 2004, **78**, 257−260.
19. P. J. Lopez, J. Descles, A. E. Allen, *Curr. Opin. Biotechnol.*, 2006, **16**, 180−186.
20. S. Lettieri, A. Setaro, L. De Stefano, M. De Stefano, P. Maddalena, *Adv. Funct. Mater.*, 2008, **18**, 1257−1264.
21. F. Xu, Y. Wang, X. Wang, Y Zhang, Y. Tang, P. Yang, *Adv. Mater.*, 2003, **15**, 1751−1753.
22. M. S. Aw, M. Barian, D. Losic, *Powder Technol*., 2013, **24**, 757−763.
23. H. Zhang, M. A. Shahbazi, E. Mäkilä, T. H. da Silva, R. L. Reis, J. Salonen, J. T. Hirvonen, H. A. Santos, *Biomaterials*, 2013, **34**, 9210−9219.
24. N. H. Malsch, *Biomedical nanotechnology*, Crc Press, 2005.
25. D. Smith, V. Schüller, C. Engst, J. Rädler, T. Liedl, *Nanomedicine*, 2013, **8**, 105−121.
26. M. D. Adams, C. Fields, J. C. Venter, *Automated DNA sequencing and analysis*, Elsevier. 2012.
27. M. L. Bochman, K. Paeschke, V. A. Zakian, *Nat. Rev. Genet*., 2013, **13**, 770−780.
28. G. Oliviero, J. Amato, N. Borbone, S. D'Errico, A. Galeone, L. Mayol, S. Haider, O. Olubiyi, B. Hoorelbeke, J. Balzarini, G. Piccialli, *Chem. Commun*., 2010, **46**, 8971−8973.
29. G. Oliviero, N. Borbone, J. Amato, S. D'Errico, A. Galeone, G. Piccialli, M. Varra, L. Mayol, *Biopolymers* , 2009, **91**, 466−477.
30. D. Jayasena, S. Sumedha, *Clin. Chem*., 1999; **45**, 1628−1650.
31. W. Tan, X. Fang, *Aptamers selected by cell-SELEX for theranostics*, Springer, 2015.
32. H. Sun, X. Zhu, P. Lu, R. Rosato, W. Tan, Y. Zu, *Mol. Ther. Nucleic Acids*, 2014, **3**, 182.
33. S. Song, L. Wang, J. Li, C. Fan, J. Zhao, *Trends Anal. Chem*., 2008, **27**, 108−117.
34. C. Sun, Q. Han, D. Wang, W. Xu, W. Wang, W. Zhao, M. Zhou, *Anal. Chim. Acta*, 2014, **850**, 33−40.
35. A. K. Deisingh, *Aptamer-based biosensors: biomedical applications*, Springer, 2006.
36. M. A Anderson, A. Tinsley-Brown, P. Allcock, E. A. Perkins, P. Snow, M. Hollings, S. Nicklin,. *Phys. Stat.*, 2003, **197**, 528−533.
37. K. P. S. Dancil, D. P. Greiner, M. J. Sailor, *J. Am. Chem.*, **121**,7925−7930.
38. B. Sciacca, E. Secret, S. Pace, P. Gonzalez, F. Geobaldo, F. Quignar, F. Cunin, *J. Mat. Chem*., 2011, **21**, 2294−2302.
39. K. A. Kilian, T. Bocking, J. J. Gooding, *Chem. Commun*., **40**, 2009,630–640.
40. J. H. Park, L. Gu, G. von Maltzahn, E. Ruoslahti, S. N. Bhatia, M. J. Sailor, *Nat. Mater*. 2009, **8**, 331–339.
41. L. De Stefano, I. Rea, P. Giardina, A. Armenante, I. Rendina, *Adv. Mater.*, 2008, **20**, 1529.
42. S. P. Low, N. H. Voelcker, L. T. Canham, K.A. Williams, *Biomaterials*, 2009, **30**, 2873–

2880.
43. I. Rea, E. Orabona, I. Rendina, L. De Stefano, *Porous silicon integrated photonic devices for biochemical optical sensing*, InTech Open Access Publisher, 2011.
44. K. H. Beckmann, *Surf. Science*, 1965, **3**, 314.
45. J. Wu, M. J. Sailor, *Adv. Funct. Mat*., 2009, **19**, 733−741.
46. M. Ferrari, *Nat. Rev. Cancer*, 2005, **5**, 161−171.
47. O. C. Farokhzad, R. Langer, *ACS Nano*, 2009, **3**, 16−20.
48. P. Parhi, C. Mohanty and S. K. Sahoo, *Drug Discov. Today*, 2012, **17**, 1044−1052.
49. R. van der Meel, L. J. Vehmeijer, R. J. Kok, G. Storm, E. V. van Gaal, *Adv. Drug. Deliv. Rev*., 2013, **65**, 1284−1298.
50. J. Shi, A. R. Votruba, O. C. Farokhzad, R. Langer, *Nano Lett*., 2010, **10**, 3223−3230.
51. S. M. Moghimi, A. C. Hunter, J. C. Murray, *FASEB J*., 2015, **19**, 311−330.
52. M. Ding, N. Song, X. He, J. Li, L. Zhou, H. Tan, Q. Fu, Q. Gu, *ACS Nano*, 2013, **7**, 1918−1928.
53. E. J Anglin, L. Cheng, W.R. Freeman, M. J. Sailor, *Adv. Drug Del. Rev*., 2008, **60**, 1266−1277.
54. C. E. Hamm, R. Merkel, O. Springer, P. Jurkojc, C. Maier, K. Prechtel, V. Smetacek, *Nature*, 2003, **421**, 841.
55. D. Losic, K. Short, J. G. Mitchell, R. Lal, N. H. Voelcker, *Langmuir*, 2007, **23**, 5014.
56. M. Sumper, E. Brunner, *Adv. Funct. Mater.*, 2006, **16**, 17−26.

2 OLIGONUCLEOTIDES-MODIFIED POROUS SILICA OPTICAL DEVICES FOR LABEL-FREE BIOSENSING

(Papers J1, J2, P1)

Significant efforts are being devoted to the development of more efficient DNA chip technology for applications in areas of social interest, such as gene expression analysis, medical diagnostics, and human therapies [1]. Commercial DNA chips use probes or targets labelled with chromophores or radioisotopes where the molecular recognition events (i.e., the hybridization of probes with targets) are monitored by fluorescence microscopes. Even if the fluorescence based technique is a standard in genomic applications, this method is strongly dependent on the labelling procedures, which sometimes can give undesirable effects on the molecular interactions [2, 3]. Moreover, reading and quantifying hundreds of thousands of fluorescence spots in a single run is not straightforward nor always precise. To overcome these limitations, a new class of label-free DNA chip has been proposed, which uses direct electrical or optical detection methods [4–6]. The label-free optical PSi devices promise to offer sensitivity, selectivity, and low cost method for the detection of DNA hybridization [7]. DNA chips can be classified as a special class of biosensors since they are realized by immobilization of single stranded oligonucleotide (ON) bioprobe, on a transducer surface. Each molecular interaction between the bioprobe and its ligand, such as hybridization to the complementary DNA sequence, is then transduced into an analytical signal by an electrochemical-, optical-, surface plasmon resonance-based or electrical device, depending on the specific technology used. Porous silicon (PSi) is by far one of the most popular transducer material due to its peculiar physical and chemical properties [8]. PSi is fabricated by electrochemical etching of crystalline silicon in aqueous hydrofluoric acid. Depending on etch time, current density and acid concentration, several porous morphologies can be obtained, from micropores (average pores size < 5 nm) to macropores (average pores size > 50 nm) [9]. The resulting sponge-like matrix is characterized by a very large specific surface area (up to 300 m^2/cm^2). Even if electrochemical etching induces silicon dissolution, the PSi surface results smooth enough to get very good quality optical devices, also in the case of multilayered structures [10]. Periodic, or quasi-periodic, alternation of high and low porosity layers is used for fabrication of Bragg reflectors, microcavities, Thue-Morse sequences: all these photonic devices exhibit resonance wavelengths that can be used as monitoring peak in quantifying biomolecular interaction from the optical point of view [11–13]. Unfortunately, the PSi structures suffer instability from oxidation and corrosion in aqueous solutions,

especially simulating biological conditions. Lots of chemical protocols have been reported in literature in order to passivate and functionalize surfaces. The immobilization of biological species should not prevent their functions, and thus should also assure their correct organization and orientation. PSi surface can be properly functionalised in order to covalently bind biological molecules such as single or double stranded DNA, proteins, enzymes, antibodies, aptamers and so on, which act as bioprobes. There are many routes to achieve surface functionalization which are based on proper chemical or biological processes. PSi surface can be activated by specific chemical groups, namely –SH, $–NH_2$ or –COOH, that could form very stable bonds, such as sulphide or peptide bond, with the biological molecule considered [14]. For some biomolecules that are usually synthesized *ex situ* and then coupled on PSi surface, there is also the possibility of directly growing the molecules (i.e., *in situ* synthesis) using PSi as support in the so-called solid phase synthesis [13, 15]. In this chapter, the realization of label-free DNA-PSi devices by *in situ* ON synthesis, is described. Since the chemistry used for the solid phase synthesis of ON can be quite aggressive against the PSi solid support, chemical stability of PSi supports is a key issue for the biosensor realization. In particular, it is well known that PSi suffers on exposure to alkaline solutions (commonly used for the deprotection of ON) which easily corrode the silicon skeleton; so a trade-off between PSi surface passivation and suitable solid-phase synthesis chemistry is strictly required. The fabrication, passivation and functionalization of PSi devices by using two different siloxanes, a comparison of their effectiveness for *in situ* ON synthesis and hybridization with complementary ON sequence, are described in detail.

2.1 Porous silicon fabrication by electrochemical etching

PSi is a very versatile material due to its peculiar morphological, physical, and chemical properties: evidence of this is the huge number of papers about PSi features and devices based on this nanostructured material, that appear in the literature every year [16–19]. One reason for this clear success is the easy fabrication of sophisticated optical multilayers by a simple, but not trivial, computer-controlled electrochemical etching process. The PSi structure is formed by electrochemical dissolution of doped crystalline silicon wafers in hydrofluoric acid (HF) based solution. The cell used for the electrochemical etching is schematized in Figure 2.1. The silicon wafer is the anode; it is placed in back-side contact on an aluminum plate while the front side is sealed with an O-ring and exposed to the anodising electrolyte. The cathode is made of platinum. The anodisation cell is made of a highly-acid resistant polymer such as polyvinylidene fluoride (PVDF) or polytetrafluoroethylene (PTFE).

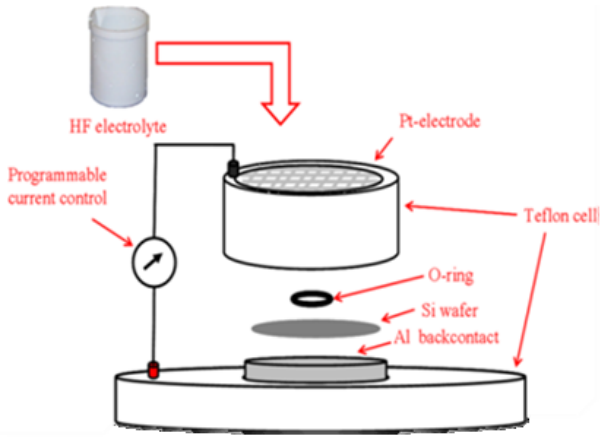

Figure 2.1. *Electrochemical etching setup.*

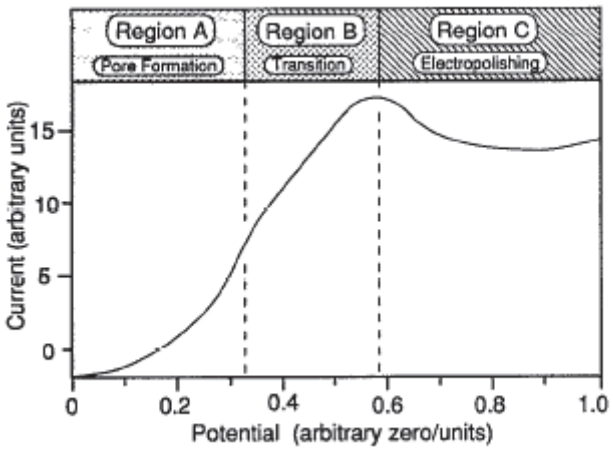

Fig. 2.2. *Anodic I-V curve for silicon in HF. In the region A pore formation occurs. In region C there is the silicon electropolishing. The region B is a transition zone where pore formation and electropolishing compete [19].*

For highly resistive silicon substrate (> few mΩ/cm) an evaporated metal backside contact is necessary to ensure the Schottky contact between the aluminum plate and the semiconductor. Figure 2.2 shows the anodic I-V curve of cristaline silicon (*n*- or *p*-type) in HF based solution; the different dissolution regions of the curve are labeled A-C. Pore formation takes place in region A. At anodic overpotentials in excess of the current "peak," region C, silicon electropolishes. At intermediate overpotentials, region B, a "transition" zone exists where pore formation and electropolishing compete for control over the surface morphology. The resulting structure within this region is generally porous in nature but the pore diameters increase rapidly as the electropolishing potential is approached. The exact dissolution chemistries of silicon are still in question, although it is generally accepted that holes are

required in the initial steps for both electropolishing and pore formation [19]. The Figure 2.3 illustrates the chemical dissolution mechanism suggested by Lehmann and Gösele, that has received great attention [17]. If a hole of the silicon substrate has the sufficient energy to reach the surface, a nucleophilic attack on Si–H bond by fluoride ion can occur and a Si–F bond is formed (step 1 in Figure 2.3).

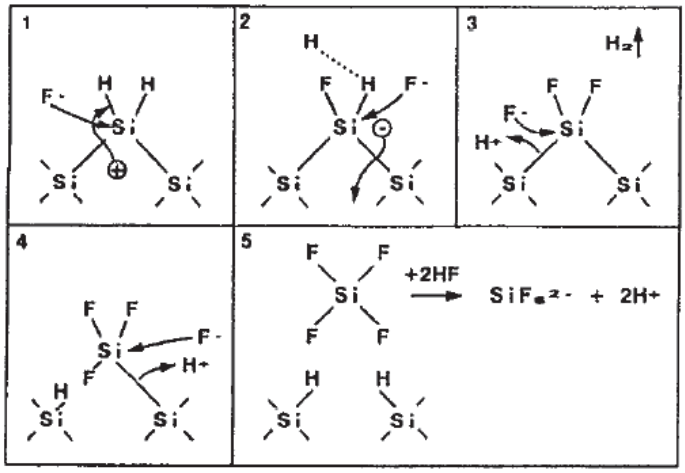

Fig. 2.3. *Dissolution mechanism of silicon in hydrofluoridric acid (HF) [17].*

Due to the polarizing influence of the Si–F bond, another F^- ion can attack and bond under generation of an H_2 molecule and injection of one electron into the substrate (steps 2 and 3). The polarization induced by the Si–F groups reduces the electron density of the Si–Si backbonds; these weakened bonds will now be attacked by HF or H_2O (step 4) in a way that the silicon surface atoms remain bonded to hydrogen atoms (step 5). The silicon tetrafluoride molecule reacts with the HF to form the highly stable H_2SiF_6. In this work, microcavities constituted by a λ/2 layer (optical thickness) sandwiched between two 9.5 period Bragg reflectors (BRs), were obtained alternating low (L) and high (H) refractive index layers whose thicknesses satisfy the Bragg relationship $n_H d_H + n_L d_L = m\lambda_B/2$ where *m* is an integer and λ_B is Bragg wavelength. The microcavities were prepared by electrochemical etching of highly doped p^+ crystalline silicon (0.001 Ω cm resistivity, <100> oriented, 500 μm thick) in HF solution (HF:ethanol 1:1) in dark at room temperature (RT) [6–9]. Before the anodization process the silicon substrates were immersed in HF solution for 2 min to remove the native oxide layer. Since the PSi fabrication process is self-stopping, it is possible to obtain adjacent layers with different porosities by changing the current density during the electrochemical etching [20]. A current density of 200 mA cm^{-2} for 1.2 s was applied to obtain low refractive index layers (n_L=1.542; d_L =125 nm) while a current density of 100 mA cm^{-2} was applied for 1.4 s for high refractive index layers (n_H=1.784; d_H = 108 nm). After electrochemical process,

pores dimension was increased to favour the infiltration of biological matter by rinsing the fresh-made PSi microcavities in a KOH ethanol solution (1.5 mM) for 15 min [9]. Figure 2.4 shows scanning electron microscope (SEM) top view images of PSi structure and histogram of pores size distribution, which reveals a mesoporous morphology constituted by pores with an average value of 30 nm. PSi is a material characterized by a high chemical reactivity; if stored in ambient air, the texture becomes partially oxidized and the refractive index changes [21]. To stabilize the PSi and eliminate the problem of aging, the thermal oxidation of the structure is generally used. The thermal oxidation was performed in pure O_2 by a two-step process: pre-oxidation at 400 °C for 30 min followed by oxidation at 900 °C for 15 min. The oxidation reduces or completely removes the Si–H from the skeleton substituting it by SiO_2, that isotropically grows also into the pores [22].

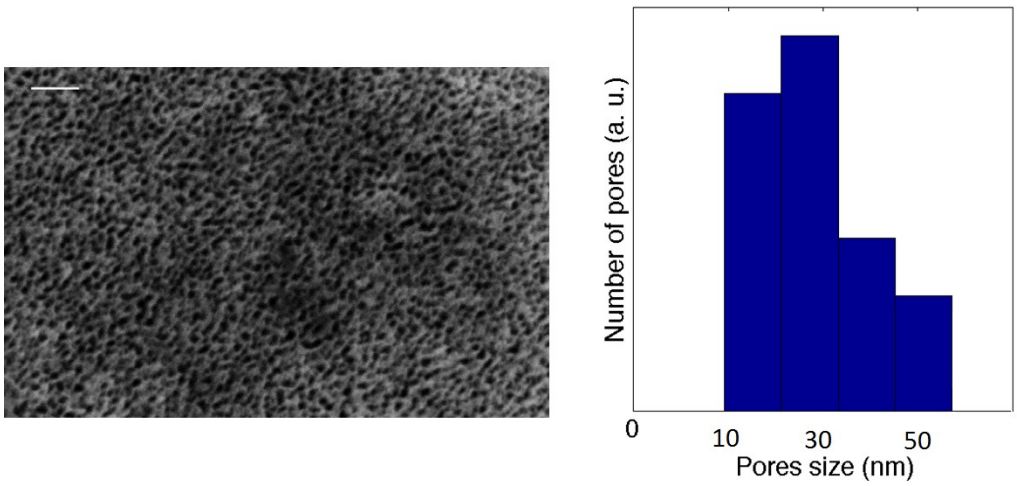

Fig. 2.4. *SEM image of mesoporous silicon and corresponding histogram of pores size distribution. Scale bar corresponds to 200 nm.*

2.2 Aminosilane-modified porous silica devices

A key requirement of PSi use in biosensing is the high stability of the material during experiments in biological solutions, avoiding the degradation of the biosensor and/or possible alteration of measurement results [23]. Moreover, for biosensor development the PSi surface should provide coupling points for the immobilization of biomolecules, preserving their specific functionalities through a good control of their orientation and organization on the surface. There are many strategies for modifying PSi surfaces, among them self-assembled monolayers-modified PSi surfaces is the most attractive one [24]. For biosensing applications of PSi, self-assembled monolayers generate layers with well-defined packing that improve the surface stability and coupling points for the immobilization of bioprobes [25]. The two most popular silane coupling agents are 3-amino-propyl-triethoxysilane (APTES) and 3-amino-

propyl-dimethyl-ethoxysilane (APDMES) able to form an aminosilane layer on PSi surface through the formation of Si–O–Si covalent bonds. Both reagents contain a short 3-aminopropyl group and provide a distal amine group for biomolecule attachment. Before functionalizing PSi with aminosilane, the reaction conditions were optimized on crystalline silicon to this aim. Eight different silane films, namely S1–S8, were prepared by incubating silicon substrates at room temperature (RT) for 30 or 60 min, into 5% silane solutions prepared by direct solution of silane compounds in ethanol or anhydrous toluene, (Table 2.1).

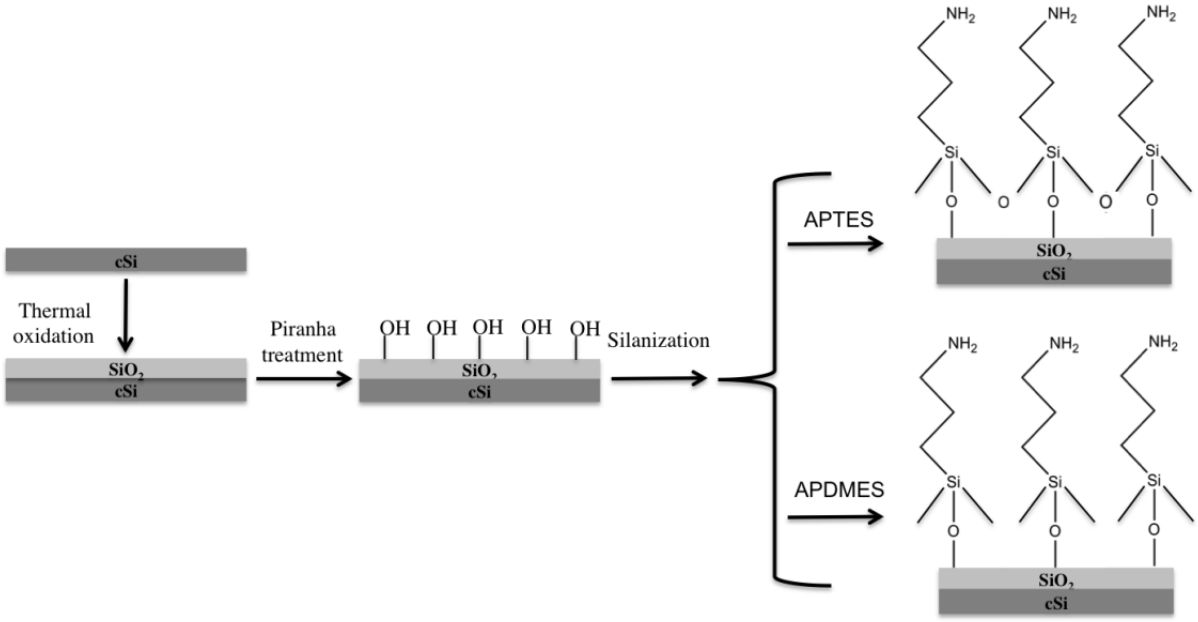

Fig. 2.5. *Scheme of cristalline silicon surface modification by APTES and APDMES.*

The scheme of silanization process performed on silicon surface is illustrated in Fig. 2.5. The thickness and uniformity of APTES and APDMES layers were investigated by spectroscopic ellipsometry (SE). Table 2.1 reports SE values: film thickness of siloxanes increases with time deposition; 60 min samples are always thicker than 30 min samples in every combination of solute (APTES and APDMES) and solvent (ethanol and toluene). Moreover, APTES thin films are thicker than APDMES ones, since APTES is able to reticulate, while APDMES is not. Best results in terms of aminosilane films homogeneity, also assessed by atomic force microscopy analysis (data non shown), were obtained on samples incubated in solutions containing 5% aminosilane in dry toluene for 30 min. These conditions were used to graft the silane molecules on the PSi surfaces. The surface of PSi microcavities were hydroxylated by Piranha solution (H_2O_2:H_2SO_4 1:4 at RT, 30 min) thus increasing their reactivity by

introduction of –OH groups. After Piranha treatment, samples were extensively washed in milli-Q® water flow and then silanized by immersion in different 5% aminosilane solutions, APTES or APDMES, in dry toluene for 30 min at RT. Excess of ungrafted silanes was removed by rinsing samples three times in dry toluene for 2 min. Measurement of transducer optical spectra by spectroscopic reflectometry is very useful to give quantitative information about PSi stability, chemical functionalization and analyte biomolecular recognition.

Sample	Silane	Solvent	Incubation time (min)	Silane thickness (Å)
S1	**Aptes 5%**	**Ethanol**	**30**	**5.5±0.3**
S2	Aptes 5%	Ethanol	60	17.3±0.3
S3	**Aptes 5%**	**Toluene**	**30**	**26.4±0.3**
S4	Aptes 5%	Toluene	60	81.3±0.8
S5	**Apdmes 5%**	**Ethanol**	**30**	**0.2±0.2**
S6	Apdmes 5%	Ethanol	60	3.0±0.3
S7	**Apdmes 5%**	**Toluene**	**30**	**4.2±0.3**

Tab. 2.1. *Sample preparation conditions and ellipsometry data.*

Optical transducers respond to refractive index change associated with the binding of inorganic/organic matter as a result of surface chemical functionalization and/or recognition of analyte [26]. The replacement of air in the pores increases the average refractive index of PSi layers, resulting in a shift of reflectivity spectra towards greater wavelengths. In Figure 2.6, reflectivity spectra of PSi microcavities before (i.e., PSi multilayers thermally oxidized) and after silanization process by APTES and APDMES are reported; in both cases, red shifts of spectra can be observed. The phenomenon is due to formation of a thin silane film on pore walls, which increases the average refractive indexes of PSi layers. In particular, a red shift of 21 nm has been registered for microcavity treated by APTES and of 6 nm in case of APDMES silanized structure. These different values are due to diverse thicknesses (t) of silane layers coating internal surface of pores, quantified applying the following equation [27]:

$$\Delta n_{pore} = n_{pore}^{after} - n_{pore}^{before} \approx 4\frac{t}{D}(n_{layer} - n_{pore}^{before}) \qquad [2.1]$$

where Δn_{pore} is the increase of pores refractive index due to presence of silane layer, D is the pores diameter, n_{layer} is the refractive index of silane layer, n_{pore}^{before} silanization process.

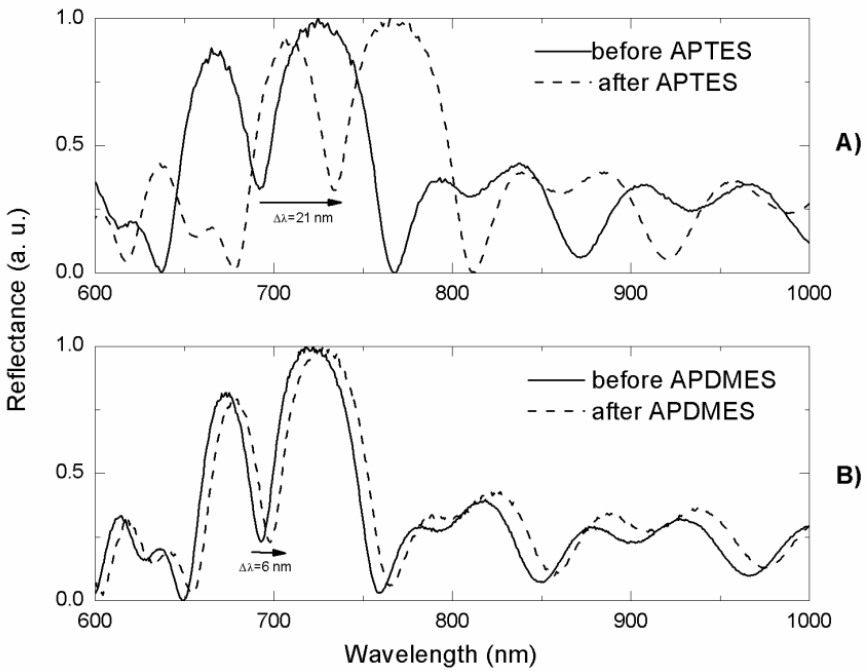

Fig. 2.6. *A) Reflectivity spectra of a PSi microcavity before (solid line) and after (dash line) the APTES functionalization. (B) Reflectivity spectra of a PSi microcavity before (solid line) and after (dash line) the APDMES functionalization.*

In our case, $n_{pore}^{before} = n_{air} = 1$ n_{layer}=n_{APTES}=n_{APDMES}=1.46(0.01), measured by spectroscopic ellipsometry, and D=15 nm (because oxidized structure) [6–8]. By changing thickness t (from 0.1 to 1 nm, by 0.1 step) in Eq. 2.1, a set of Δn_{pore} values, which have been used to calculate PSi microcavity spectrum red-shifts, were obtained [28]. Red-shift observed in case of APTES silanization (21 nm) corresponds to 0.7 nm thick layer computed (Δn_{pore}=0.086); the lower shift measured for APDMES treatment (6 nm) corresponds to a layer with a calculated thickness of 0.2 nm (Δn_{pore}==0.024). This result depends on the ability of APTES to polymerize, because it has three potential points to attach PSi substrate or other silane molecules, while APDMES cannot do it, since it has an only one point to attach substrate (see binding schemes in Figure 2.4) [29].

The variation of surface wettability before and after silanization processes was characterized by measurements of water contact angle (WCA), as shown in Figure 2.7. The control of surface wettability plays a key role in studies of biomolecules immobilization. The oxidized PSi is strongly hydrophilic, resulting in a WCA value of (12.6±0.8)°; APTES, with its alkyl chain and three ethoxy groups, induces an increase of the WCA to (34±1)° corresponding to a reduction in the degree of hydrophilicity; APDMES, characterized by the same alkyl chain but two methyl groups, creates a surface with a higher WCA (42±4)°.

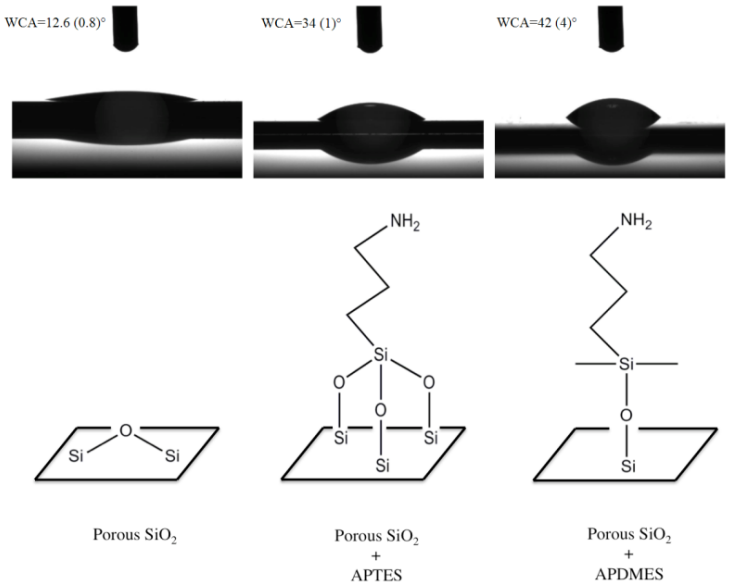

Fig. 2.7. *Water contact angle measurements performed on oxidized porous silicon before and after APTES and APDMES modifications .*

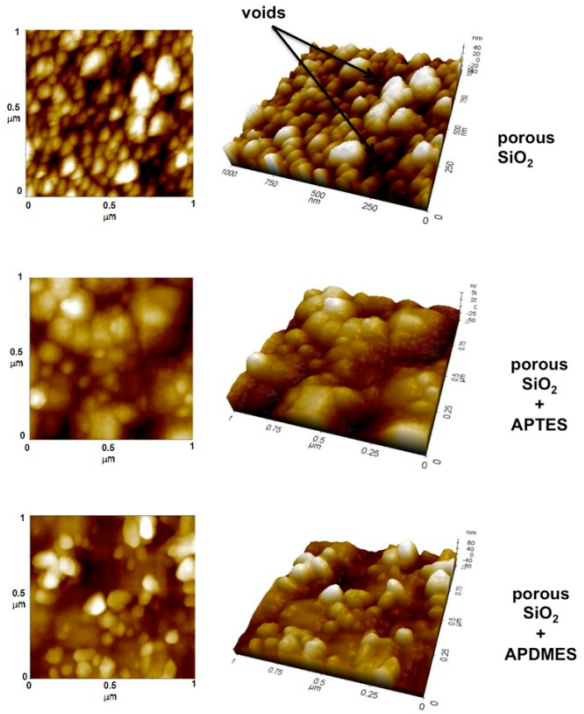

Fig. 2.8. *AFM images of bare oxidized PSi and aminosilane modified oxidized PSi surfaces .*

Atomic force microscopy (AFM) was used to characterize the samples surface before and after aminosilane modification. The AFM images of bare oxidized PSi, APTES- and APDMES-modified PSi surfaces are reported in Figure 2.8. AFM image of porous SiO_2 reveals a sponge-like structure characterized by hillocks and voids randomly distributed on the whole surface; pores size can be estimated to be on the order of 20 nm. After APTES

grafting (porous SiO_2+APTES), most voids disappear due to partial pore cloaking by silane layer coating the pore walls. Quite same result is obtained in the case of APDMES modification (porous SiO_2+APDMES): even if APDMES forms a thinner layer, voids in the porous matrix are strongly reduced.

2.3 *In situ* synthesis of oligonucleotide on porous silica

Fabrication of biosensors and microarrays, and more generally of each inorganic device coupled to a biomolecule, has its main issue in bioconjugation (i.e., the immobilization of a working biological probe onto a solid surface). Bioconjugation represents a current challenge crossing both material sciences and biomedical applications [30, 31]. In order to develop a DNA biosensor, the *in situ* oligonucleotide synthesis on PSi surfaces can be chosen as an alternative method to the traditional *ex situ* immobilization of DNA fragments. *In situ* technique allows to covalently biofunctionalize amino-modified PSi structure, directly growing oligonucleotide sequence on the surface, thus obtaining high ON surface coverage and flexibility in the choice of the probe sequence [32]. After a preliminary characterization of PSi-APTES (PSi-L_a) and PSi-APDMES (PSi-L_b) devices, a comparison of their effectiveness for *in situ* ON synthesis was evaluated by exposing the devices to the same synthesis. Solid phase ON syntheses were performed by a PerSeptive Biosystem Expedite 8909 DNA automated synthesizer. The 13-mer polythymine ON strand was assembled on the different aminosilane modified microcavities, following phosphoramidite chemistry by thirteen growing cycles [33, 34]. PSi structures, PSi-$L_{a,\,b}$-NH_2 (L_a = APTES, L_b = APDMES), were introduced in a suitable column reactor to be used in the automated synthesizer; the syntheses were performed according to the scheme reported in Figure 2.9. In all cases, the first reaction step involved the attachment of the 3'-ending nucleobase to the amino group of PSi-bound APTES or APDMES. This step required the activation of the protected phosphoramidite dissolved in dry acetonitrile via protonation by weakly acidic tetrazole (0.45 M in acetonitrile). Once the first nucleobase was installed on the solid support, the ON growth was obtained by repeating the following sequential steps of the automated ON synthesis:

Coupling: reaction of the protected phosphoramidite dissolved in dry acetonitrile and activated via protonation by weakly acidic tetrazole (0.45 M in acetonitrile) with the 5'-OH ON terminal group.

Oxidation: oxidation of the unstable phosphite triester linkage to the more stable phosphotriester by standard oxidizing solution of iodine in pyridine/acetonitrile.

Capping: acylation of the unreacted 5′-OH ON terminal groups by acetic anhydride in pyridine and tetrahydrofuran to minimize deletion products and simplify the purification process.

Detritylation: removal of the 5′-dimethoxytrityl (DMT) protecting group from the support-bound 5′-terminal nucleotide with the deblocking solution of trichloroacetic acid in dichloromethane (3% w/w).

The amount of DMT cation released by acid treatment was used as a direct measure of the efficiency of the ongoing synthesis. The release of the protecting group generates a bright red-orange colour solution in which the quantity of the DMT cation can be measured online by UV-Vis spectroscopy at 495 nm (ε = 71,700 $M^{-1}cm^{-1}$). At the end of each growing cycle the support was thoroughly washed with acetonitrile before the beginning of the successive cycle. The quantification of functionalization yield of each synthesis cycle by ultraviolet (UV) spectroscopy after detritylation of 5'-dimethoxytritil (DMT) group released in solution, was performed [15]. In the first one, yield is quite constant and high (approximately 100% ± experimental errors), while in the second one there is a dramatic decrease: each solid phase synthesis step involves an increasing inefficiency as oligonucleotide length is increased. Efficiency of coupling to PSi-APTES (Figure 2.10 (A)) falls just after the forth-base growth; this threshold is pushed after the seventh thymine in case of PSi-APDMES (Figure 2.10 (B)).

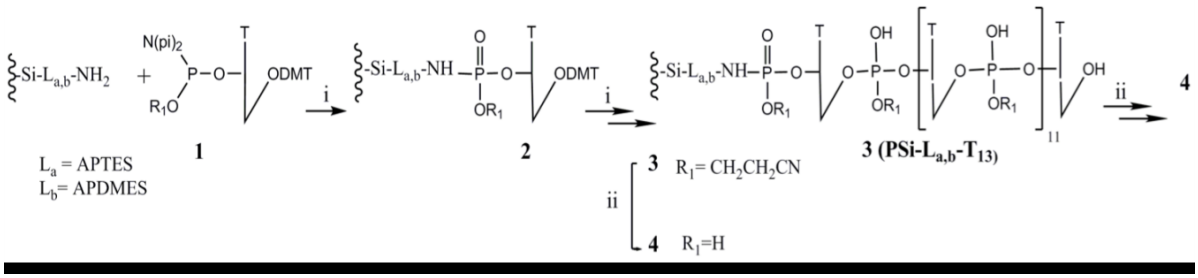

Fig. 2.9. *Synthetic procedure for solid phase synthesis of aminosilane PSi-T13 (PSi-$L_{a,b}$-T13), i) standard automatic synthetic cycle; ii) phosphates-deprotection, K_2CO_3 (0.05 M)/MeOH dry.*

Aminosilane	I_{T13}	F (mol/g)	SSA (m^2/g)	F (nmol/cm^2)
APTES	0.12±0.01	(2.6±0.2)x10^{-5}	39	0.067±0.005
APDMES	0.17±0.01	(3.7±0.2)x10^{-5}	43	0.086±0.005

Tab. 2.2. *Functionalization values calculated for the PSi structures modified with the two aminosilanes.*

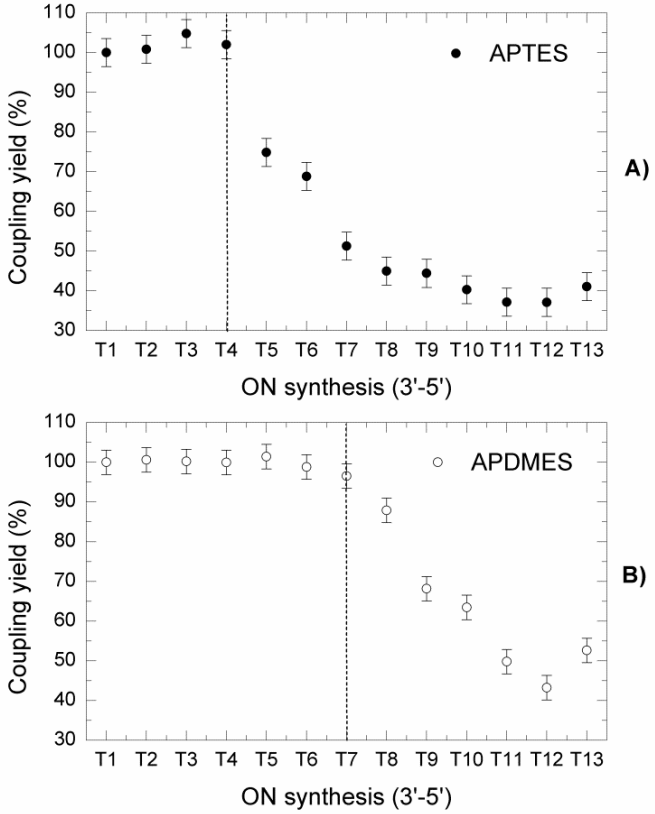

Fig. 2.10. *Coupling yield calculated by means of DMT measurements performed on the PSi samples silanized with APTES (A) and with APDMES (B).*

In general, coupling yield to PSi-APDMES is greater than that of PSi-APTES for all the synthesis cycles, up to the 13th thymine (T13). This experimental result can be reasonably ascribed to higher steric hindrance of pores caused by thicker APTES film with respect to APDMES one. UV intensity measurements at T13 (I_{T13}, first column of Table 2.2) also enable the quantification of functionalization *F* in terms of mol/g for both samples (PSi-$L_{a,b}$ weight about 0.3 mg) by using Lambert-Beer formula (molar absorptivity ε=71700 $M^{-1}cm^{-1}$). Data obtained are reported in Table 2.2 together with the specific surface area (*SSA*) of PSi-$L_{a,b}$. PSi samples "as etched" are characterized by *SSA* values of about 100 m^2/g measured by Brunauer-Emmett-Teller (BET) method [15]; the KOH process induces an increase of porosity of about 6% corresponding to an increase of *SSA* equal to 106 m^2/g, quantified by spectroscopic reflectivity (50 nm blue shift of the microcavities spectra, data not shown here). On the contrary, thermal oxidation decreases SSA to 60% (from 106 m^2/g to 43 m^2/g), due the isotropic silica growth also into the pores [35]. PSi-$L_{a,b}$ SSA values, shown in Tab. 2.2, have been calculated by applying a simplified model based on the cylindrical shape of the pores taking into account the thickness of silane layer on the pore walls (0.7 nm for APTES and 0.2 nm for APDMES). Samples functionalization in terms of $nmol/cm^2$, last column in Table 2.2,

is the ratio *F/SSA*. The better coupling yield obtained for APDMES-modified PSi results in higher number of moles per square centimetre with respect to the APTES one (about 0.09 *vs* 0.07). The results demonstrated the possibility of synthetizing oligonucleotide sequence on a silanized porous matrix without harming its structure, and monitoring ON synthesis by optical spectroscopy. Furthermore, chemical stability of the support material turns to be key issue for hybridization experiment. Since, APDMES-PSi sample shown an higher functionalization due to less steric hindrance of pores than APTES one, it was used for hybridization studies with complementary and not complementary sequence.

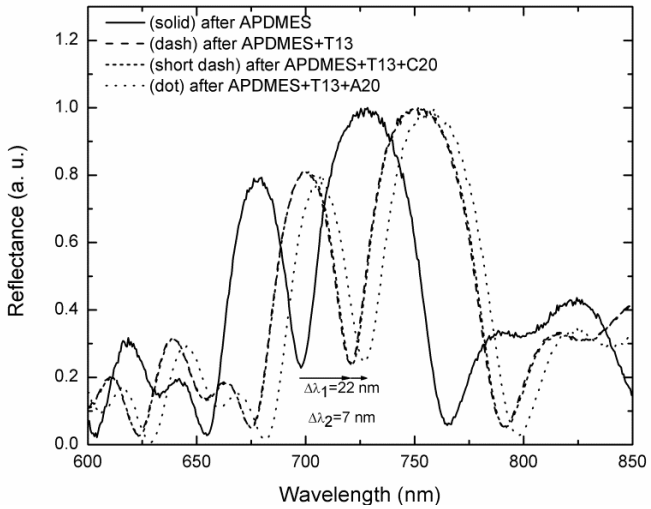

Fig. 2.11. *Reflectivity spectra of the PSi microcavity after the APDMES functionalization (solid line), after the T13 synthesis (dash line), after the C20 incubation (short dash line), and after the A20 incubation (dot line)*

2.4 Label-free optical detection of DNA-DNA hybridization

In molecular biology, hybridization (or hybridisation) is a phenomenon in which single-stranded deoxyribonucleic acid (DNA) or ribonucleic acid (RNA) molecules anneal to complementary DNA or RNA [36]. Hybridization is a basic property of nucleotide sequences and is the underlying mechanism of molecular recognition of DNA-biosensors. The hybridization of DNA-PSi (PSi-L_b-T13) biosensor to complementary (Fluo-dA20) and non-complementary (Fluo-dC20) oligonucleotide sequences has been monitored by spectroscopic reflectometry and, for comparison, also by fluorescence microscopy. Figure 2.11 shows reflectivity spectra of device before synthesis process, after T13 synthesis, and after complementary DNA interaction: a red shift of 22 nm has been detected after T13 synthesis, which is a value higher than 11 nm obtained in case of oxidized multilayer [15]. This red shift increase is due to a higher chemical stability of the PSi platform during the synthesis process. The spectrum shifts further of 7 nm after the complementary DNA exposure, thus

demonstrating the detection of DNA-DNA interaction. In Figure 2.11 it is also possible to observe how exposure to non-complementary sequence does not induce any shift, confirming specificity of biosensor. Optical monitoring of T13-A20 hybridization has also been proved by fluorescence analysis. In Figure 2.12, bright field (A) and fluorescence (B) images of PSi-L_b-T13 surface after incubation with labelled complementary (Fluo-dA20; left image) and non-complementary (Fluo-dC20; right image) sequences, are reported. While in bright field imaging surface samples appeared indistinguishable, switching from bright-light source to fluorescence-light source, a fluorescence (maximum peak value = 73 counts; average intensity =34 counts) on exposure to complementary ON sequence was observed. On the contrary, chip incubated with non-complementary sequence appeared completely dark (maximum peak value= 7 counts; average intensity = 5 counts), further confirming the specificity of the DNA-biosensor.

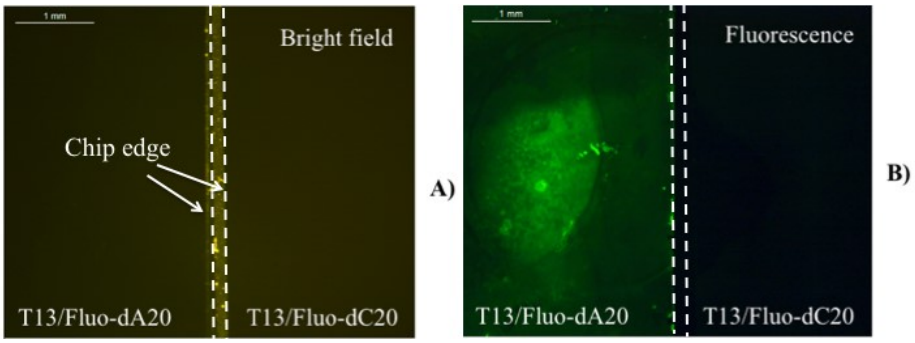

Fig. 2.12. *Bright field (A) and fluorescence (B) images of the PSi surface functionalized with T13 after the incubation with the solutions containing Fluo-dA20 (left) and Fluo-dC20 (right). Scale bar= 1 mm.*

References

1. D. K. Kim, K. Kerman, M. Saito, R. R. Sathuluri, T. Endo, S. Yamamura, E. Tamiya, *Electroanalysis*, 2007, **19**, 1239−1257.
2. F. Wei, B. Sun, Y. Guo, X. S. Zhao, *Biosens. Bioelectron*., 2003,**18**, 1157–1163.
3. M. Piliarik, H. Vaisocherova, J. Homola, *Sens. Actuators B-Chem*., 2007, **121**, 187–193.
4. P. Furbert, C. Lu, N. Winograd, L. De Louise, *Langmuir,* 2008, **24**, 2908–2915.
5. V. S. Y. Lin, K. Motesharei, K. P. S. Dancil, M. J. Sailor, M. R. Ghadiri, *Science*, 1997, **278**, 840−843.
6. V. Lehman, *Electrochemistry of Silicon*, Wiley-VCH, 2002.
7. L. Canham, *Properties of Porous Silicon*, Inspec/IEE, 1997.
8. L. Pavesi, *Porous silicon dielectric multilayers and microcavities*, La Rivista del Nuovo Cimento, 1997.
9. E. De Tommasi, I. Rendina, I Rea, V. Di Sarno, P. Arcari ,A. Lamberti, C. Sanges, L. De Stefano, *Sensors,* 2008, **8**, 6549-6556.

10. L. De Stefano, I. Rea, P. Giardina, A. Armenante, I. Rendina, *Adv. Mat*., 2008, **20**, 1529−1533.
11. L. Moretti, L. De Stefano, I. Rea, I. Rendina, *Appl. Phys. Lett.,* 2007, **90**, 191112.
12. J. M. Buriak, *Chem. Mater.,* 2013, **26**, 763−772.
13. I. Rea, G. Oliviero, J. Amato, N. Borbone, G. Piccialli, I. Rendina, L. De Stefano, *J. Phys. Chem*. *C*, 2010, **114**, 2617–2621.
14. K. A. Kilian, T. Bocking, J. Gooding, *Chem. Commun.,* 2009,**10**, 630–640.
15. J. H. Park, L. Gu, G. von Maltzahn, E. Ruoslahti, S. N. Bhatia, M. J. Sailor, *Nat. Mater.,* 2009, **8**, 331–339.
16. S. P. Low, N. H. Voelcker, L. T. Canham, K. A. Williams, *Biomaterials*, 2009, **30**, 2873–2880.
17. V. Lehmann, U. Gösele, *Appl. Phy. Lett*., 1991, **58**, 856–858.
18. M. J. Sailor*, Porous silicon in practice: preparation, characterization and applications*, John Wiley & Sons, 2012.
19. R. L. Smith, S. D. Collins, *J. Phys. Chem*., 1992, **71**, 1–22.
20. J. Salonen, V. P. Lehto, E. Laine, *Appl. Surf. Science*, 1997, **120**, 191−198.
21. L.T. Canham, C. L. Reeves, J. P. Newey, M. R Houlton, T. I. Cox, J. M. Buriak, M. P. Stewart, *Adv. Materials*, 1999, **11**, 1505−1507.
22. N. Aissaoui, L. Bergaoui, J. Landoulsi, J. F. Lambert, S. Boujday, *Langmuir*, 2012, **28**, 656-665.
23. J. J. Gooding, S. Ciampi, *Chem. Soc. Rev.*, 2011, **40**, 2704−2718.
24. W. Theiß, *Surf. Science Rep*., 1997, **29**, 91−192.
25. W. H. A. Kuijpers, J. Huskens, C. A. A. van Boeckel., *Tetrahedron Lett.* 1990, **31**, 6729−6732.
26. H. Ouyang,C. C. Striemer, P. M. Fauchet, *Appl. Phys. Lett.,* 2006, **88**, 163108.
27. P. Pirasteh, J. Charrier, A. Soltani, S. Haesaert, L. Haji, C. Godon, N. Errien, *Appl. Surf. Science,* 2006, **253**, 1999−2002.
28. B. Kasemo, *Surf. Sci.,* 2002, **500**, 656−677.
29. M. P. Schwartz, F. Cunin, R. Cheung, M. J. Sailor, *Phy. Stat. Solidi A*, 2005, **202**, 1380−1384.
30. X. Gao, E. Gulari, X. Zhou, *Biopolymers*, 2004, **73**, 579−596.
31. W. Pfleiderer, B. Markus, *Solid phase synthesis of oligonucleotides*, U.S. Patent No. 5,936,077, 1999.
32. J. Amato, B. Pagano, N. Borbone, G. Oliviero, V. Gabelica, E. De Pauw, S. D'Errico, V. Piccialli, *Bioconjugate Chem.*, 2011, **22**, 654−663.
33. .P. Pirasteh, J. Charrier, A. Soltani, S. Haesaert, L. Haji ,C. Godon, N. Errien, A*ppl. Surf. Science*, 2006, **253**, 1999−2002.
34. G. M. Blackburn, *Nucleic acids in chemistry and biology*, Royal Society of Chemistry, 2006.

3 LABEL-FREE PSI APTASENSOR FOR HUMAN THROMBIN DETECTION

(Papers J3, J4, P2, P4)

Aptamers are an emerged class of single-stranded oligonucleotides generated from SELEX techniques [1, 2]. Aptamers by folding into well-defined secondary or tertiary structures are able to specifically bind their target molecules with high affinity, and so are classified as powerful ligands for diagnostic and therapeutic applications [3]. Aptamers as bioprobes opened new generation of DNA biosensors called aptasensors [4]. Due to their unique properties, aptamers provide more advantages than conventional bioprobes (e.g., antibody) [3, 5]. One of the most studied G-quadruplex-based aptamer is thrombin-binding aptamer (TBA). It demonstrated able to bind α-thrombin, a key protein involved in the clotting process, preventing the pathological process of thrombosis [6, 7]. In this chapter, the realization of high sensitive and reversible PSi-based TBA biosensor by *in situ* synthesis for the detection of human α-thrombin molecule is described. Human thrombin is a serin protease, also known as coagulation factor II, that converts soluble fibrinogen (factor I) into insoluble strand of fibrin (factor Ia) with crucial role in coagulation and hemostatsis [6]. The equilibrium between production and inhibition of this enzyme prevents hemorrhagic or thrombotic phenomena. The concentration of thrombin in healthy subject can be almost absent until getting up from nM to μM level in the coagulation process [7]. High level of thrombin in the blood (beyond the normal coagulation phenomenon) could determine pathological coagulation giving thrombotic disorder such as thromboembolism, ischemic stroke etc., fatal for human health [8]. Moreover, some disorders on central nervous system (SNC), such as Alzheimer, could be potentially related to high levels of thrombin, which involves degeneration of neurons and cell death; as well as an involvement of this serin-protease in cancer disease [9, 10]. In this chapter, preliminary studies on mixed-ON *in situ* synthesis and PSi stability to new deprotection ON condition are reported. Then, the fabrication and characterization of a selective, sensitive and reversible PSi-aptasensor through *in situ* synthesis for thrombin molecule detection is described.

3.1 Mixed oligonucleotide-modified porous silica

The high selectivity of oligonucleotides and derivatives is a crucial aspect for DNA-biosensors development [11]. The use of mixed-sequence of oligonucleotides and an increasing of probe length have been shown to enhance the selectivity of DNA-biosensor,

particularly for the detection of non-nucleic acid targets [12]. The 19-mer mixed sequence oligonucleotide 5'-GATTGATGTGGTTGATTTT-3' was assembled on two different aminosilane modified microcavities, following phosphoramidite chemistry by nineteen growing cycles. The fabrication and aminosilane-modification of PSi microcavities by APTES or APDMES were performed following the procedures described in Chapter 2. Before the synthesis of mixed ON sequence the stability of amino-modified-structures to standard deprotection condition of nucleobases, was evaluated. Alkaline solutions are commonly used for the standard deprotection of nucleobases with drawback to easily corrode the silicon skeleton; so a trade-off between PSi surface passivation and PSi-friendly ON deprotection conditions of mixed ON on PSi supports is required. The reflectivity spectra and graphs of peak-shift *vs* incubation time for APTES- and APDMES- modified PSi before and after treatment with 33% aqueous ammonia (17 h, 55 °C) used in the standard deprotection condition are reported in Figure 3.1. The stability of the surfaces were tested by a full dip in ammonia solution for different times (30, 60, 90, 120 min). The results showed that the destructive effect of ammonia solution was about the same for both samples: a blue shift of 25 or 50 nm was detected after 30 min or 1 h, respectively, and the complete dissolution of the silicon matrices occurred after 2 h. Because aqueous ammonia could not be used in deprotection steps, the saturated methanolic ammonia dry solution as an alternative strategy was tested [13]. Both the two aminosilane-modified PSi structures were highly stable at this condition. In both devices a perfect overlap of spectra before and after the treatment was observed, thus confirming the feasibility of this deprotection strategy (data not shown). Once deprotection conditions were checked and set up for PSi samples, amino-modified PSi structures, were used as supports for automated *in situ* solid phase mixed-ON synthesis using the standard phosphoramidite chemistry. The amount of 5'-dimethoxytrityl released after the detritylation step was used to quantify the functionalization yield of each synthesis cycle by UV/Vis spectroscopy (Figure 3.2). Up to the fourth coupling cycle almost the same coupling yield for both aminosilane-functionalized PSi supports was observed. From the fifth cycle on, the coupling yields dropped for both supports, even if higher functionalization yields were generally observed for PSi supports functionalized with APTES. Both PSi microcavities gave a medium yield process, mainly due to average pore size (about 20 nm). PSi photonic devices with pore dimensions greater than that value, but always compatible with high optical quality response in the visible-near infrared, could be suitable to maximize yield of mixed-ON synthesis. Figure 3.2 also shows the reflectivity spectra of devices before and after the *in situ* synthesis process: red shifts of 60 nm and 70 nm were detected respectively for APTES- and

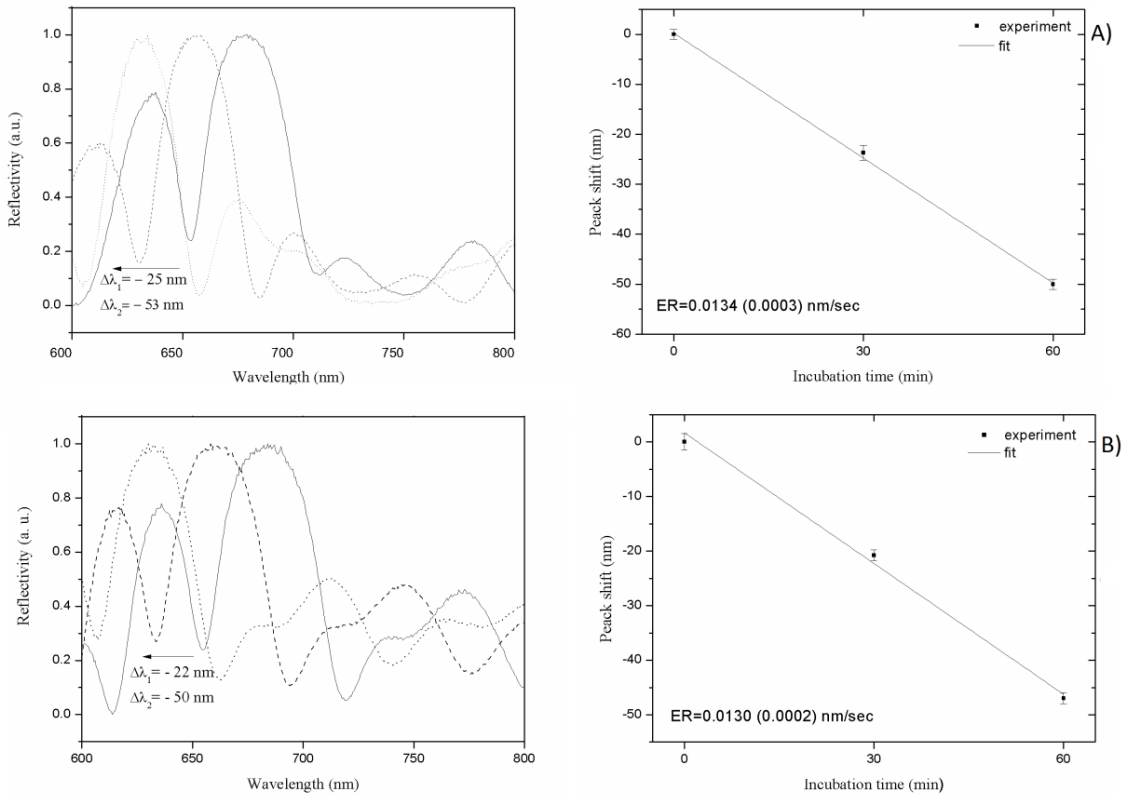

Fig. 3.1. *A) Reflectivity spectra of APTES modified PSi microcavity before (solid line) and after 30 (dashed line) and 60 min (dotted line) of incubation in 33% NH_3 at 55°C. Corresponding peak shift vs incubation time. B) Reflectivity spectra of APDMES modified PSi microcavity before (solid line) and after 30 (dashed line) and 60 min (dotted line) of incubation in 33% NH_3 at 55°C. Corresponding peak shift vs incubation time.*

APDMES-modified devices, thus indicating that more ON had grown on the latter device with respect to the first one. This experimental result is ascribed to the less steric hindrance of pores due to thinner APDMES film, as previously described in Chapter 2. After to *in situ* synthesis, the samples were exposed to dry NH_3/MeOH solution in order to deprotect the mixed-ON sequence. A blue shift of only 2 and 4 nm, attributed to the removing of bound N-2 isobutyryl (on G), N-6 benzoyl (on A) and N-4 benzoyl (on C) from PSi-APTES and PSi-APMES was observed, respectively (data not shown). The ability of dry NH_3/MeOH solution to completely deprotect the PSi-aminosilane-bound ON, was also confirmed by chromatographic analysis, proving complete cleaving of the amide bound N-2, N-4 and N-6 groups after 3 hours at RT. Furthermore, the ammonia in dry MeOH is able to quickly remove the 2-cyanoethyl phosphate protecting group [13]. This data, together with findings on the compatibility with the silicon structure, indicate the dry NH_3/MeOH solution as the best choice to deprotect mixed-ON sequence, giving the possibility of realizing more specific DNA-PSi biosensor without promoting the basic hydrolysis on the support, which instead occurs in aqueous conditions.

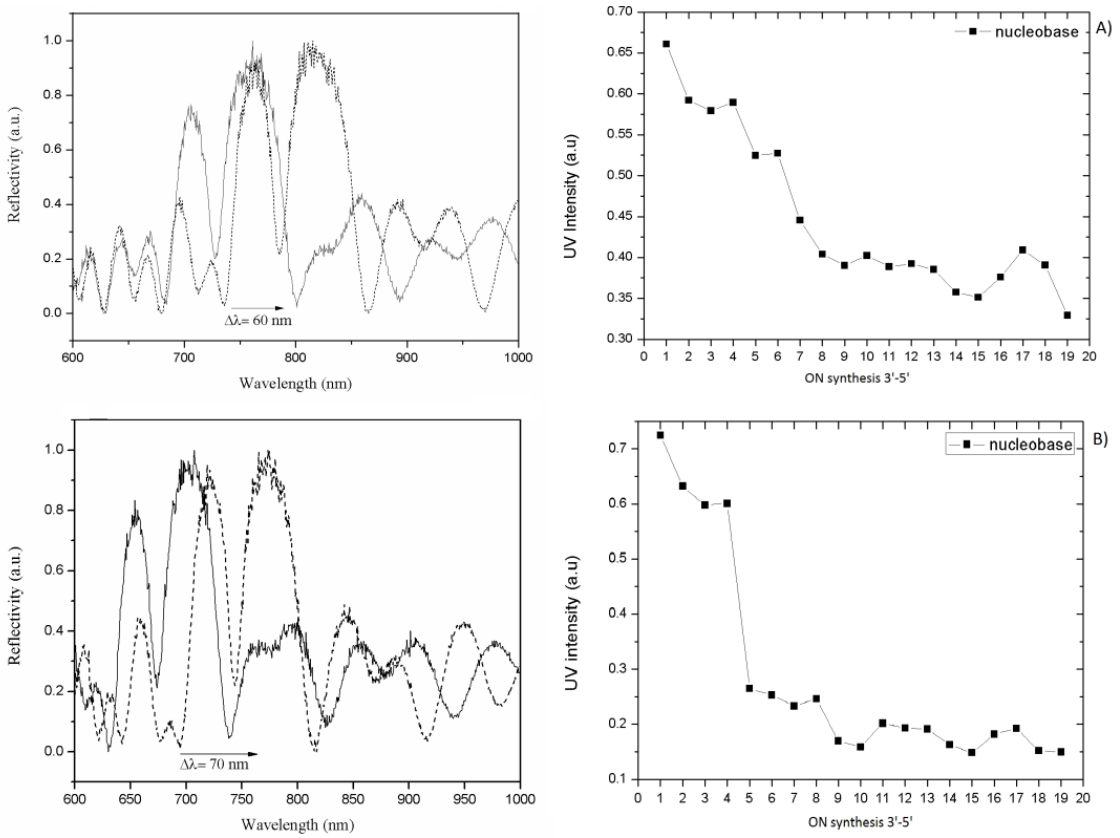

Fig. 3.2. *A) Reflectivity spectra of APTES modified PSi microcavity before (solid line) and after ON synthesis (dashed line). Corresponding UV intensity vs ON synthesis. B) Reflectivity spectra of APDMES modified PSi microcavity before (solid line) and after ON synthesis (dashed line). Corresponding UV intensity vs ON synthesis.*

The mixed-ON sequences were detached form PSi solid supports, purified by High Performance Liquid Chromatography (HPLC) and compered to control ON mixed sequence, respectively (data not shown). The results showed an incomplete synthesis of both ON sequences, confirming the need of a macroporous structure as solid support, in order to optimize the mixed-ON synthesis.

3.2 Anti-thrombin aptamer -modified porous silica biosensor

TBA PSi aptasensor for label-free thrombin detection was developed via solid phase synthesis on macroporous silicon device. Macroporous silicon structure with pore size included between 100 and 200 nm (Figure 3.3) was fabricated by electrochemical etching of n-crystalline silicon (0.01-0.02 Ω cm resistivity, ⟨100⟩ oriented and 500 μm thick) in hydrofluoric acid (HF 5% in weight)/ethanol solution at room temperature (RT). A current density of 20 mA/cm^2 was applied for 90 s to produce a single layer of PSi with a porosity of 52% (n = 1.54) and a thickness of 2 μm.

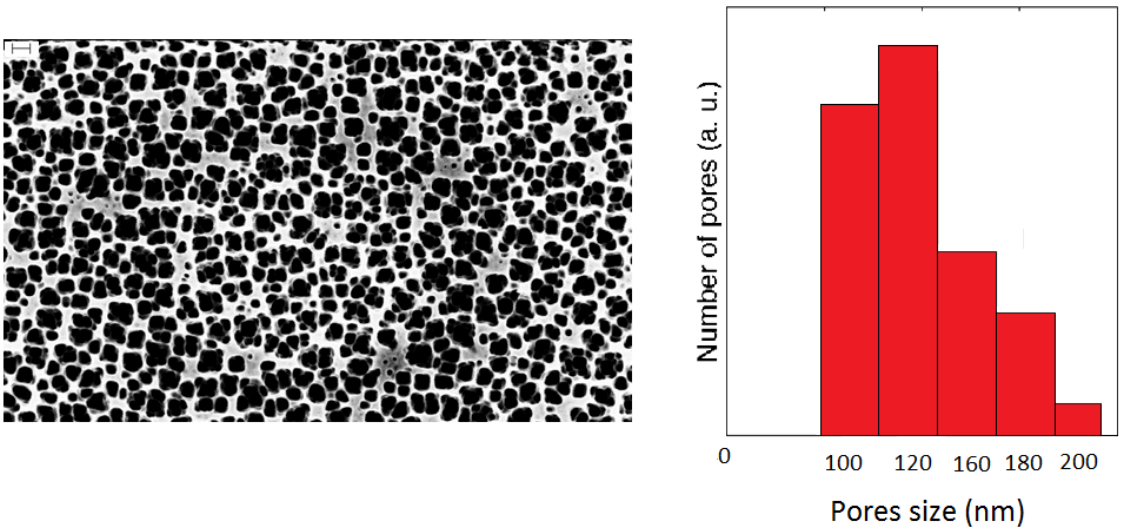

Fig. 3.3. *SEM image of macroporous silicon and corresponding histogram of pores size distribution. Scale bar corresponds to 200 nm.*

Before the etching procedure, the silicon substrate was immersed in HF solution for 2 min to remove the native oxide layer. Subsequently the thermal oxidation was performed to passivate the PSi surface. The PSi structure used acts as a Fabry−Perot interferometer [14]. The optical path (nPSiL) of the PSi layer was calculated from the reflectivity spectrum by fast Fourier transform (FFT) which displays a peak whose position along the x-axis corresponds to two times the optical path (2nPSiL) of the layer [15]. As previously demonstrated, both aminosilane compounds (i.e., APTES and APDMES) shown a good protection of PSi structures against reagents used for *in situ* synthesis. In this case, the silanization procedure was developed by using APTES thus obtaining a better coating of PSi pores, due to the property of the aminosilane to polymerize. Moreover, macroporous silicon structure used for the realization of TBA-aptasensor, has a less steric hindrance of pores than mesoporous one which requires, on the contrary, aminosilane thin film.

In Figure 3.4 (A), normal incidence reflectivity spectra are shown for oxidized-PSi layer before and after aminosilane-modification and corresponding Fourier transforms (FFT) are reported, in Figure 3.4 (B). The FFT peak shift of about 30 nm is due to an increase of the PSi layer average refractive index as result of APTES coating of pore walls. PSi-APTES device has been exposed to synthesis of TBA based on phosporamidite chemistry, quantifying the functionalization yield of each synthesis cycle by UV spectroscopy after detritylation of 5'-dimethoxytritil (DMT) group released in solution. In Figure 3.5 the synthesis yield for PSi–APTES kept fairly constant throughout all TBA synthesis contrary to what was previously observed for 19-mer mixed ON synthesis.

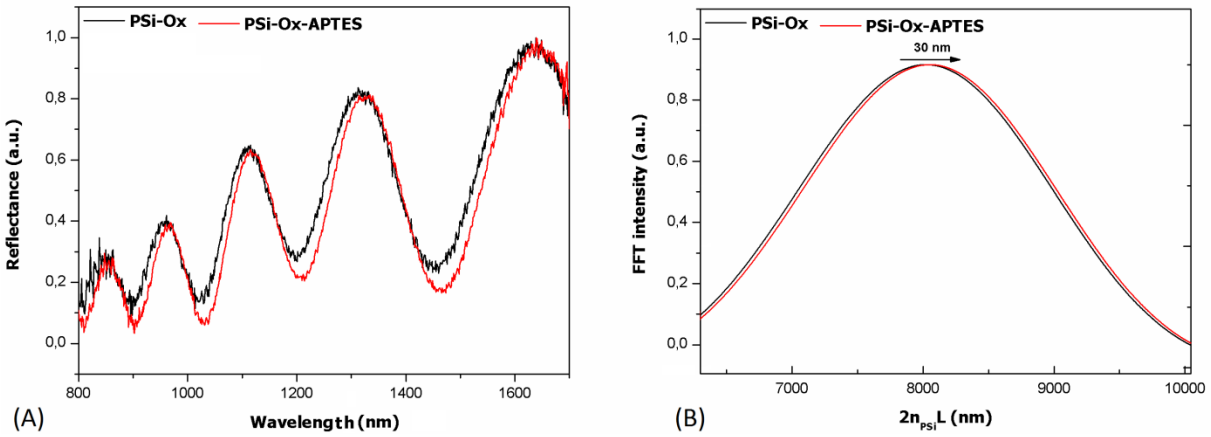

Fig. 3.4. *Reflectivity spectra (A) and correspondent FFT (B) of a PSi oxidized structure before (black line) and after (red line) the APTES functionalization.*

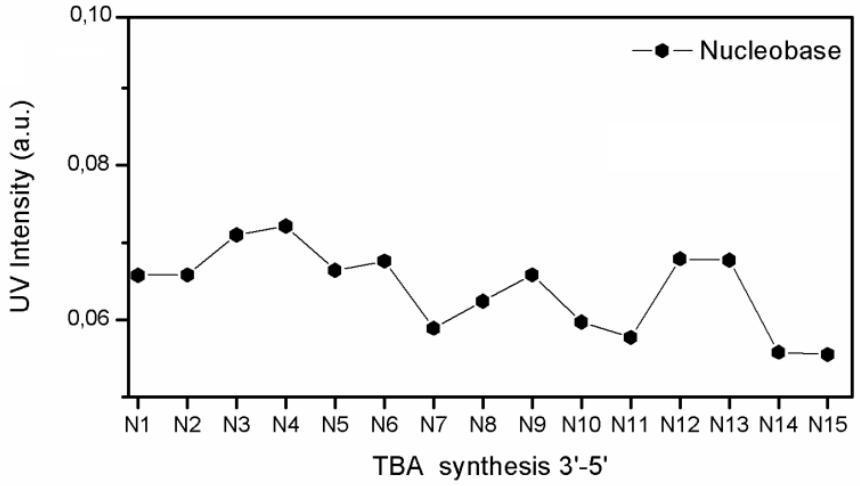

Fig. 3.5. *Coupling yield calculated by means of DMT measurements performed on the silanized PSi sample with APTES.*

The maximized yield synthesis of TBA macromolecule was ascribed to less steric hindrance of macroporous structure than mesoporous one allowing the correct and complete bioprobe growth [16]. Figure 3.6. shows reflectivity spectra (A) with corresponding FFTs (B) of PSi–APTES before and after the *in situ* synthesis process: a calculated FFT peak shift of 36 nm confirmed the successful of TBA growth on device making the PSi structure sensitive to thrombin detection. The target molecular recognition of DNA-biosensor requires the deprotection of each base constituting the ON grown on the PSi. The PSi-aptasensor (PSi-TBA) was deprotected by ammonia solution under anhydrous conditions (NH_3/dry methanol) which promotes the effective deprotection of the phosphate and exocyclic amino groups of nucleobases without the basic hydrolysis of the PSi .

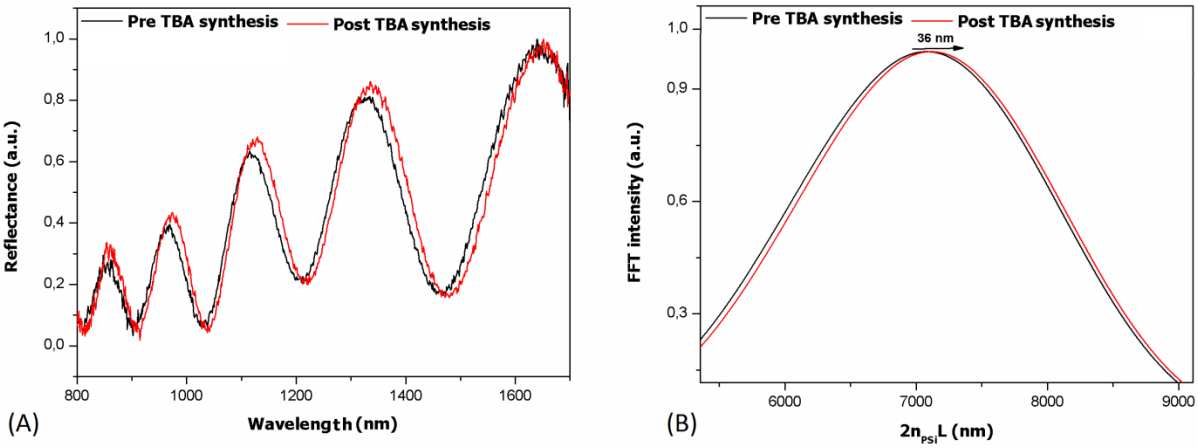

Fig. 3.6. *Reflectivity spectra (A) and corresponding Fourier transforms (B) of aminosilane modified PSi before (black line) and after the TBA synthesis (red line).*

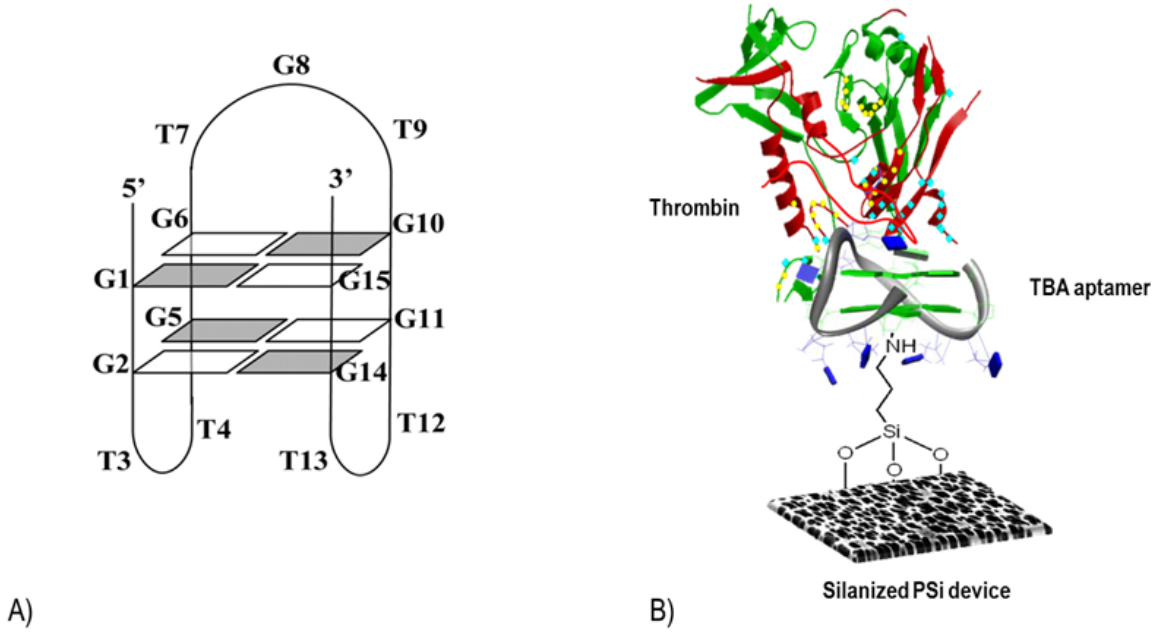

Fig. 3.8. *Scheme of TBA structure (A) and TBA-PSi biosensor (B). In presence of thrombin, TBA folds into an antiparallel unimolecular G-quadruplex dictating its thrombin-binding affinity.*

3.2.1 Human thrombin detection

Because of TBA capability of inhibiting the activity of thrombin, extensive studies on the structure of TBA were carried out to know and demonstrate the binding mode between TBA and thrombin [6]. In presence of thrombin and/or monovalent cations, TBA folds into an antiparallel unimolecular G-quadruplex dictating its thrombin-binding affinity [7] (Fig. 3.8). After the deprotection process, the PSi-aptasensor was exposed to different molar

concentration of thrombin solutions (13, 27, 54 and 109 nM). Figure 3.9 shows the optical spectra of label-free PSi-aptasensor (A) after interaction with different thrombin concentration and corresponding FFTs (B). FFT peak shift is proportional to the amount of analyte (i.e. human thrombin). When the control solution of albumin (HSA) at different molar concentrations was incubated with PSi-aptasensor surface no obvious peak shift was observed, confirming specificity of the aptasensor (Fig 3.10).

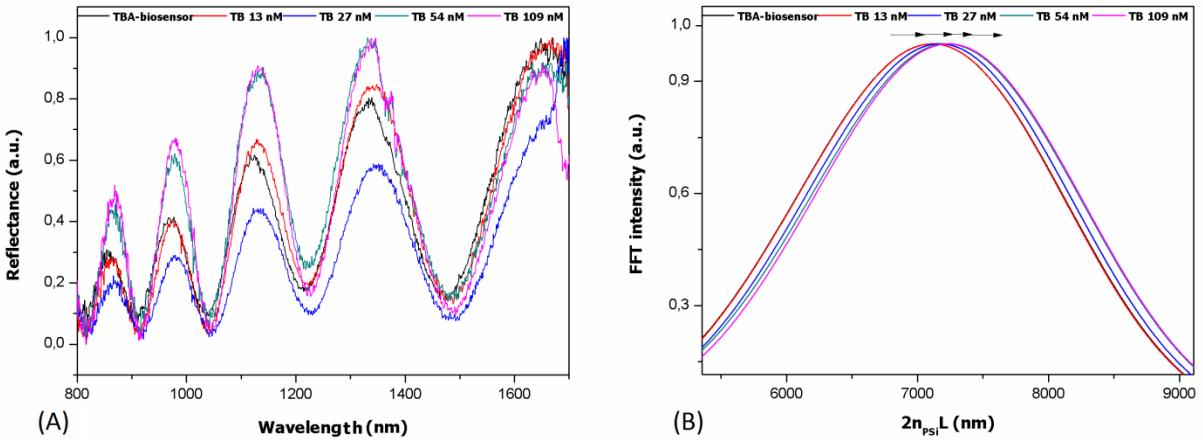

Fig. 3.9. *Reflectivity spectra (A) and corresponding Fourier transforms (B) of TBA-biosensor after exposure to thrombin solutions (13, 27, 54 and 109 nM).*

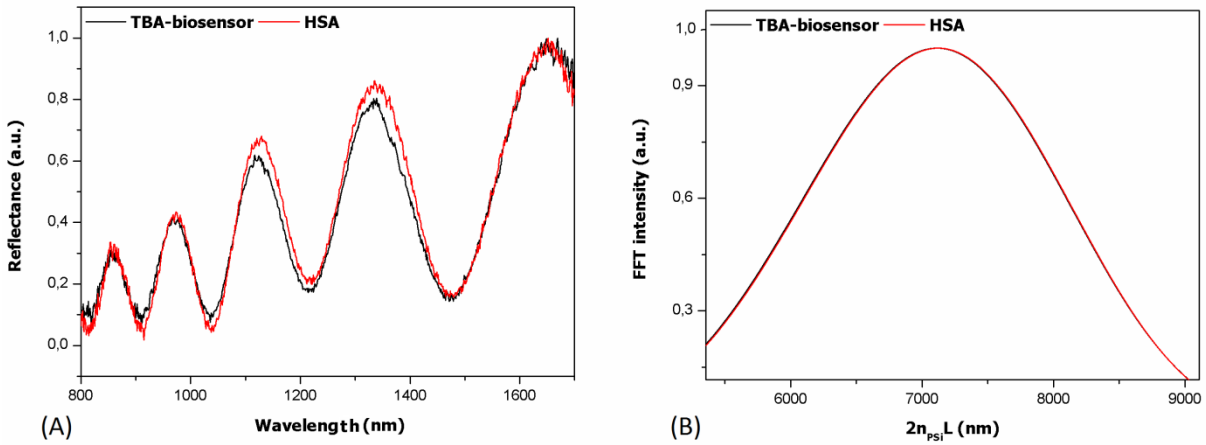

Fig. 3.10. *Reflectivity spectra (A) and corresponding Fourier transforms (B) of TBA-biosensor after exposure to the control HSA solutions (13, 27, 54 and 109 nM).*

3.2.2 Reversibility, sensitivity, and limit of detection of PSi aptasensor

The reversibility of biosensor is an advantageous requirement due to the continuous sensing measurement by the same device, resulting beneficial in terms of money and time consuming [17]. The reversibility of TBA-biosensor was proved by exposing the device to melting temperature of TBA. DNA melting, also called DNA denaturation, is the process by which

double-stranded deoxyribonucleic acid unwinds and separates into single-strand through the breaking of hydrogen bonds between the bases [18]. At melting temperature of 53 °C, TBA straightening loses the typical G-quadruplex structure and then thrombin binding affinity. However, the process is reversible thus cooling the temperature the aptamer comes back in the form it was originally [19]. The Figure 3.11 reports reflectivity spectra (A) with corresponding FFTs (B) of TBA-biosensor before (i.e. analyte saturated) and after restore, and after exposure to thrombin. The results showed that spectrum of restored-aptasensor (R-TBA-biosensor) coincides to that of TBA-biosensor before thrombin detection, confirming the reversibility of the aptasensor. A FFT peak shift of 68 nm was measured after exposure of R-TBA-biosensor to thrombin solution (109 nM) demonstrating a preserved functionality of the biosensor to recognize thrombin.

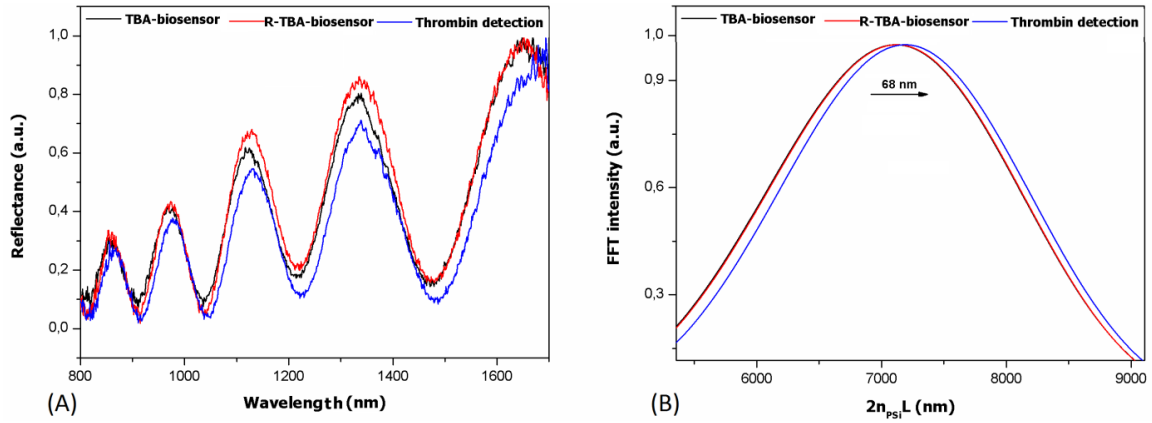

Fig. 3.11. *Reflectivity spectra (A) and corresponding Fourier transforms (B) of TBA-biosensor after TBA synthesis (black line), after recondition (red line), and after exposure to solution of thrombin (blu line).*

Since TBA acts as inhibitor of enzymatic activity of the thrombin, Michaelis–Mentens-like equation was used as model of enzyme kinetic to describe TBA–thrombin interaction [20]. The optical thickness of TBA-biosensor as function of thrombin concentration is reported in Figure 3.12; data were fitted by OriginLab Software™ by using Michaelis and Mentens-like equation:

$$y = \Delta\lambda max \frac{[TB]}{Km + [TB]}$$

where Δλmax represents the maximum rate achieved by the system at maximum (saturating) substrate concentrations; the affinity constant K_m is the substrate concentration at which the reaction rate is half of Δλmax [20]. K_m constant gives information about the affinity of the enzyme toward the substrate: a low value of K_m indicates a high affinity for the substrate. The

calculated K_m value for PSi-aptasensor is 18.6 ± 9.2 nM, sensitivity of 1.3 ± 0.3nm nM^{-1} (calculated in the range of linearity of system response) and limit of detection (LOD) of 4.0 ± 0.9 nM are comparable to accurate methods for thrombin detection [20–22].

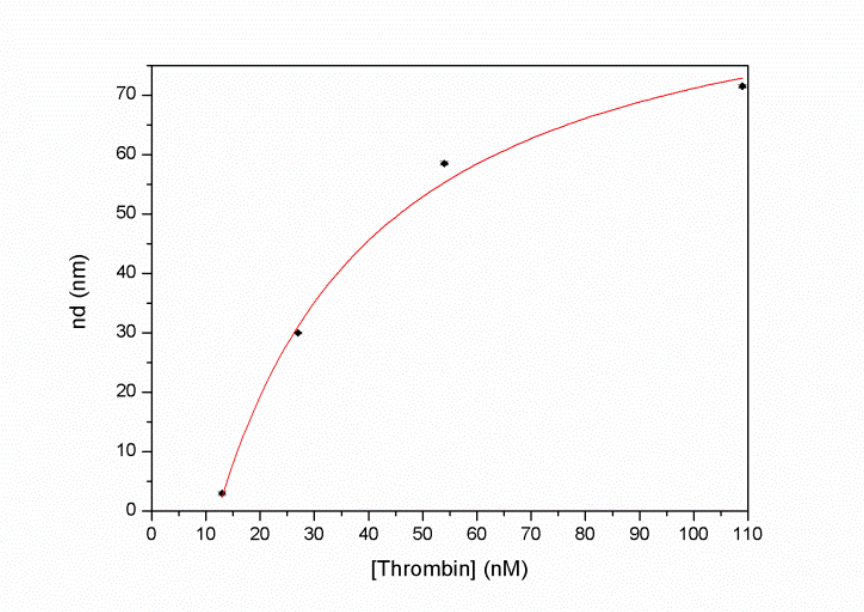

Fig. 3.12. *Optical thickness of TBA-biosensor vs thrombin concentration. Experimental data (black symbols) were fitted using Michaelis-Menten-like kinetic model.*

References

1. S. D. Jayasena, *Clin. Chem*., 1999, **45**, 1628–1650.
2. T. Hermann, D. J. Patel, *Science*, **287**, 820–825.
3. M. Mascini, *Aptamers in bioanalysis*. John Wiley & Sons, 2009.
4. T. C. Chiu, C. C. Huang, *Sensors*, 2009, **9**,10356–10388
5. E. Baldrich, A. Restrepo, C. K. O'Sullivan, *Anal. Chem*., 2004, **76**, 7053–7063.
6. T. Coppola, M. Varra, G. Oliviero, A. Galeone, G. D'Isa, L. Mayol, N. Borbone, *Bioorg. Med. Chem*, 2008, **16**, 8244–8253.
7. N. Borbone, M. Bucci, G. Oliviero, E. Morelli, J. Amato, V. D'Atri, S. D'Errico, V. Vellecco, G. Cirino, G. Piccialli, C. Fattorusso, M. Varra, L. Mayol, M. Persico, M. Scuotto, *J. Med. Chem*., 2012, **55**, 10716–10728.
8. D. M Tasset, M. F. Kubik, W. Steiner, *J. Mol. Biol.*, 1997, **272**, 688–698.
9. H. Yang, J. Ji, Y. Liu, J. Kong, B. Liu, *Electrochem. Commun*., 2009, **11**, 38–40.
10. J. Zain, Y. Q. Huang, X. Feng, M. L. Nierodzik, J. Li, S. Karpatkin, *Blood,* 2000, **95**, 3133–3138.
11. E. T. Kool, *J. Chem. Soc*., 1991, **113**, 6265–6266.
12. T. Mairal, V. C. Özalp, P. L. Sánchez, M. Mir, I. Katakis, C. K. O'Sullivan, *Anal. Bioanal. Chem.*, 2008, **390**, 989–1007.
13. R. P Iyer, D. Yu, J. Xie, W. Zhou, S. Agrawal, *Bio Med Chem Lett* 1997,**11**,1443.
14. C. Pacholski, M. Sartor, M. J. Sailor, F. Cunin, G. M. Miskelly, *J. Am. Chem. Soc*., 2005, **127**, 11636–11645.
15. M. Casalino, G. Coppola, M. Iodice, I. Rendina, L. Sirleto, *Opt. Express*, 2012,

20,12599−12609.
16. M. R. Lee, P. M. Fauchet. *Opt. Express*, 2007, **15**, 4530–4535.
17. K. P. S Dancil, D. P. Greiner, M. J. Sailor, J. *Am. Chem. Soc.*, 1999,**121**, 7925–7930.
18. G. W. Lehman, J. P. McTague, *J. Chem. Phys*., 1968, **49**, 3170–3179.
19. I. R. Krauss, A. Merlino, A. Randazzo, E. Novellino, L. Mazzarella, F. Sica, *Nucleic Acids Res*., 2012,**512**, 1–8.
20. M. B. Gu, K. Hak-Sung, *Biosensors based on aptamers and enzymes*, Springer, 2014.
21. M. Lee, D. R. Walt, *Anal. Biochem.*, 2000, **282**, 142–146.
22. D. K Kim, K. Kerman, H. M. Hiep, M. Saito, S. Yamamura, S. Takamura, E. Tamiya, *Anal. Biochem*., 2008, **379**, 1–7.

4 DIATOMITE: A NATURAL NANOSTRUCTURED MATERIAL FOR BIOMEDICAL APPLICATIONS

(Papers J5, P3)

In recent years, emerging natural porous materials for biomedical applications have been suggested to overcome the shortcomings of the synthetic porous materials, finding in diatomite a viable surrogate [1−3]. Diatomite is a cheap fossil compound formed by fragments of diatom siliceous skeletons, with similar physicochemical properties of man-made fabricated PSi [4, 5]. Due to its peculiar properties such as ordered pore structures, amorphous silica, high surface area, tailorable surface chemistry, high permeability, biocompatibility, non-toxicity, low cost, optical and photonic properties, diatomite has been used in different applications, including optics, photonics, filtration, sensing, biosensing, and protein separation [6−12]. The main constituent of diatomite is amorphous silica, approved by Food and Drug Administration (FDA) as Generally Recognized as Safe (GRAS, 21 CFR Section 573.340) for foods and pharmaceuticals production, and classified in the 3th group of "Not classifiable as to its carcinogenicity to humans" by the International Agency for Research on Cancer (IARC) [13]. Surprisingly, its use in nanomedicine is still undervalued, and only recently diatom frustules have been explored as microcapsules for oral drug delivery, resulting in a non-cytotoxic biomaterial with high potential to improve the bioavailability of loaded oral drugs by sustaining the drug release and enhancing the drug permeability [11]. In this Chapter, the fabrication of diatomite nanoparticles (DNPs) is described. A multistep chemical procedure to purify the NPs from organic and inorganic impurities, is also reported. The potentialities of DNPs as nanocarrier for drug delivery applications through *in vitro* cytotoxicity and cellular internalization studies, are investigated.

4.1 Diatomite powder from mining industries to nanovectoring: morphological and composition analysis

Diatomite is a fossil material of sedimentary origin formed by fragments of diatom skeletons, called frustules. Frustules of diatoms, single-cell photosynthetic algae largely diffused in aquatic environments, are mainly constituted by amorphous silica and are characterized by a specific surface area up to 200 m^2/g [14]. In nature, there are different kinds of diatoms (about 110,000 species) varying in size (from 2 μm to 2 mm) and morphology [15]. The low cost, abundance, easy availability, excellent biocompatibility, non-toxicity, thermal stability, and chemical inertness make diatomite an intriguing material for several applications ranging from filtration to pharmaceutics [16−19]. Diatomite powder, due to its sedimentary origin, can

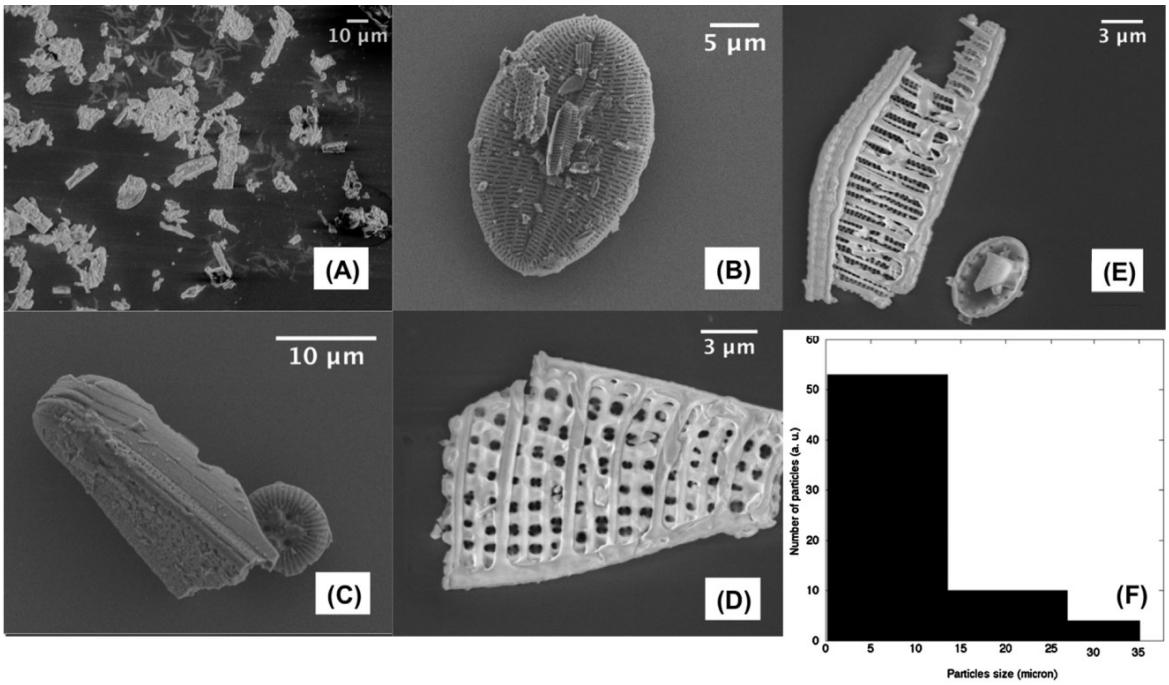

Fig. 4.1. *SEM images of purified diatomite structures (A–E) and particles size histogram (F) calculated from (A).*

contain some traces of impurities such as organic components and metallic oxides (MgO, Al_2O_3, Fe_2O_3) coming from the environment. A multistep procedure based on mechanical reduction of frustules to NPs and chemical purification treatments, were developed in order to make DNPs safer and more biocompatible vehicles for medical applications. About 5g of crashed diatomite powered (DEREF Spa, Italy) was resuspended into 250 mL of absolute ethanol and sonicated for 18 h to break large aggregates. The dispersion was sieved through a nylon net filter with pore size of 41 µm, and then filtered with pore size of 0.45 µm. The diatomite nanopowder was purified to remove the organic and inorganic impurities. First, the sample was centrifuged and the pellet treated with Piranha solution (2 M H_2SO_4, 10% H_2O_2) for 30 min at 80°C. Then, the NPs dispersion was centrifuged for 30 min at 13.500 rpm, washed twice with distilled water, resuspended in 5 M HCl, and incubated overnight at 80°C. DNPs were then centrifuged for 30 min at 13.500 rpm and washed twice with distilled water to eliminate HCl residues. The diatomite powder was morphologically characterized before and after the processing by scanning electron microscopy (SEM), transmission electron microscopy (TEM), and dynamic light scattering (DLS) analysis. Before the processing, diatomite resulted as a mixture of fragments with circular, elliptical, elongated, and squared shape, with dimension distribution ranging from few microns up to ~40 µm, as shown in Figure 4.1. After the mechanical and chemical treatments, diatomite powder appeared as an heterogeneous population constituted by nanostructures morphologically different in shape

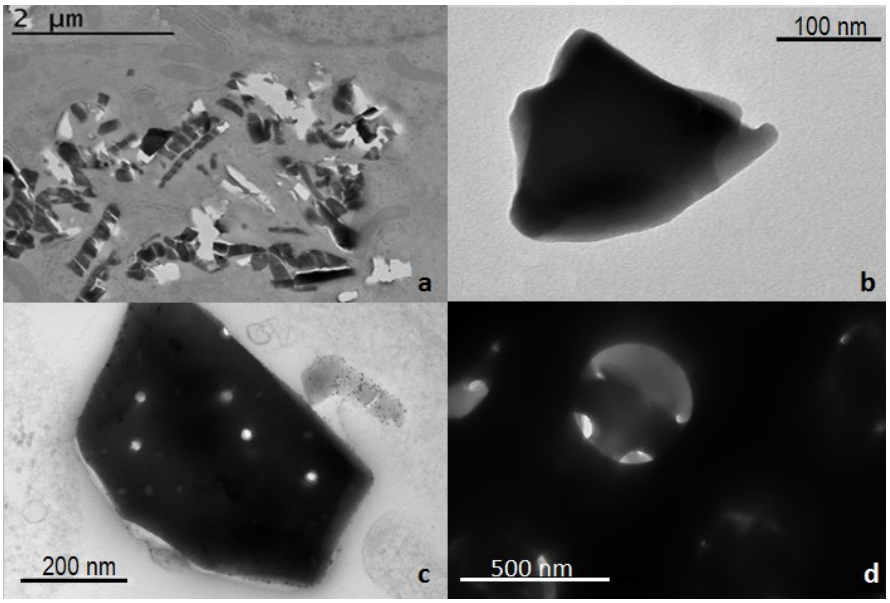

Fig. 4.2. *TEM images of bare (a-c) and increasing zoom of the pores of the NPs (d).*

and size. As shown in Figure 4.2 (C, D) the porous structure of the NPs is preserved even after the breaking of the diatomite powder in nanoparticles, where it is clearly visible the hierarchical pore organization on the surface of the diatomite NPs and the mesopores (10 nm < pores diameter < 50 nm) inside macropores (pores diameter > 50 nm). Due to their peculiar porous nature, diatomite NPs can be very promising for the loading of a wide size range of molecules from small molecules to peptides, oligonucleotides, proteins, and antibodies for the preparation of targeted NPs for drug delivery applications [20, 21]. Size and surface charge of purified DNPs dispersed in water (pH = 7) were determined by DLS. The average size and zeta-potential of NPs were 220 ± 90 nm and −19 ± 5 mV, respectively. The negative value of zeta-potential is due to the presence of silanol groups on NPs' surface due to treatment in Piranha solution. Compared to other nanocarriers, the nanometric size and morphology of these particles make them suitable in drug delivery applications [22].

The variation in the chemical composition of diatomite powder before and after purification treatments was evaluated by energy dispersive X-ray spectroscopy (EDS), photoluminescence (PL) and Fourier transform infrared spectroscopy (FTIR) analyses, confirming the improvement of the silica nanopowder quality due the removal of impurities. In Figure 4.3, EDS spectra show changes in chemical composition of the samples: after cleaning treatments, the intensities of peaks corresponding to calcium, iron and aluminum decreased, whereas the silica peak increased (Figure 4.3 C, D). Detailed chemical composition of diatomite before and after purification treatments is summarized in Table 4.1. In Figure 4.4, the FTIR spectra of untreated (A) and purified (B) diatomite, are reported.

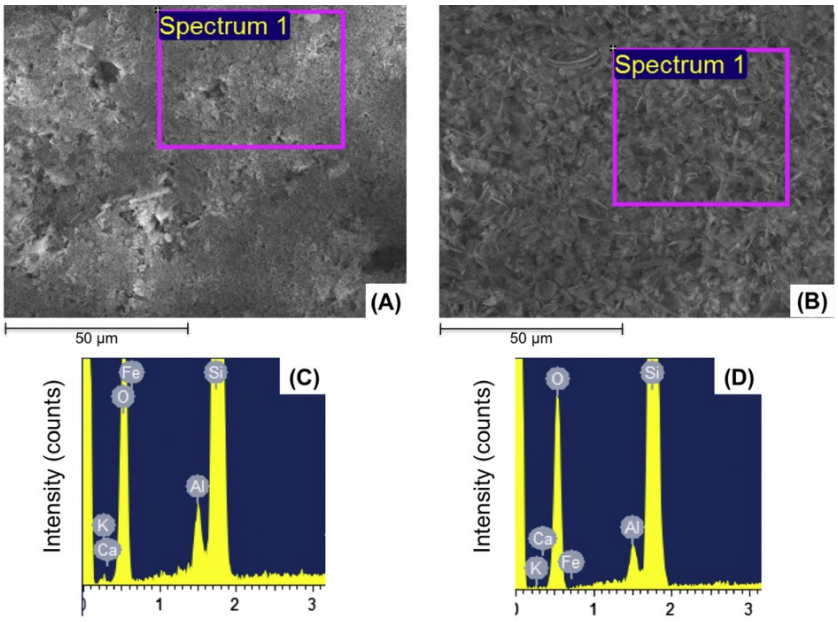

Fig. 4.3. *SEM images of diatomite deposited on silicon before (A) and after (B) purification treatments; corresponding EDS graphs (C–D).*

Compounds	Before Purification (%)	After Purification (%)
SiO_2	**92.1**	**94.6**
Al_2O_3	3.3	2.7
K_2O	**1.0**	**0.8**
CaO	1.8	0.9
Fe_2O_3	**1.8**	**1.0**

Tab. 4.1. *Chemical composition of frustules before and after purification treatments.*

After the chemical treatment in acid solutions, the peak at 680 cm^{-1} and the band at 620–580 cm^{-1} related to Si−O−Fe and Fe−O−Fe bonds, respectively, disappeared due to the removal of metallic impurities from the diatomite amorphous silica matrix. Under UV excitation (325 nm), diatomite samples showed a blue photoluminescence, clearly visible by naked eye. Even if the origin of this emission is not completely clear, it is commonly believed that it is mainly originated from surface defects including −OH groups and oxygen vacancies [23]. Laser pumping generates excited electrons whose radiative decay produces photoluminescence emission. Figure 4.4 A shows the comparison between photoluminescence spectra of diatomite before and after treatments. The untreated sample was characterized by a weak signal with three main features peaked at 390 nm (3.18 eV), 460 nm (2.7 eV), and 500 nm (2.48 eV). After treatment, the peak at 390 nm became weaker, another peak at 423 nm (2.93

eV) appeared, while the feature at 500 nm shifted to 490 nm (2.53 eV). These modifications were due to the removal of metallic impurities from the frustule surface, accordingly to FTIR characterization (Figure 4.4 B). The absence of impurities significantly modified the PL signal changing reactions of energy transfer by surface radiative recombination.

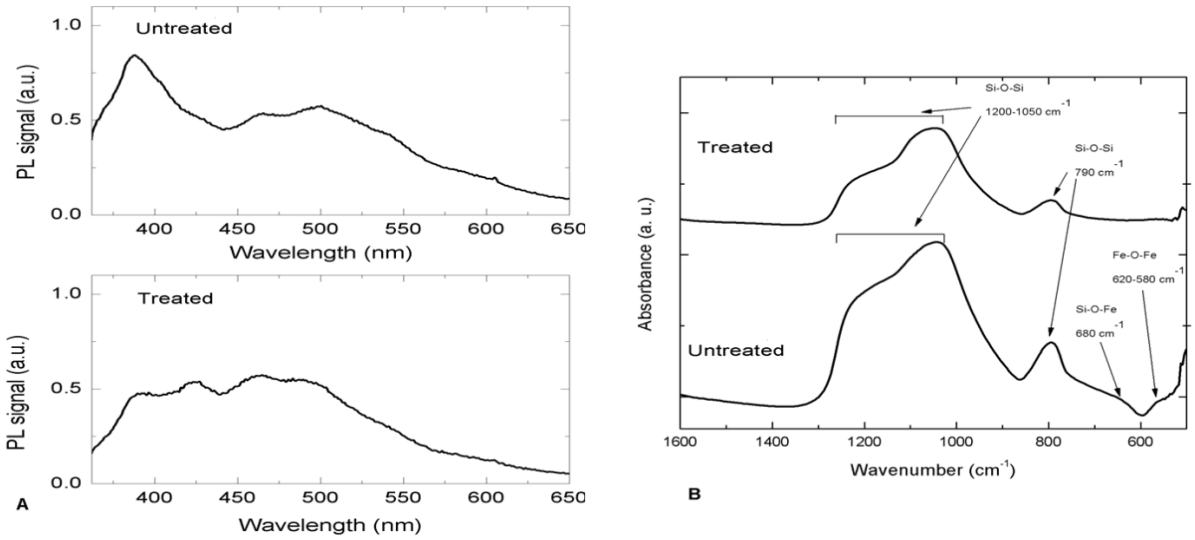

Fig. 4.4. *PL (A) and FTIR (B) spectra a of diatomite before (untreated) and after (treated) purification treatments.*

4.2 Diatomite nanoparticles: toxicity and cell internalization studies

A critical issue for biomedical applications of new nanocarriers for drug delivery is the evaluation of their potential toxicity and biocompatibility [24]. *In vitro* cytotoxicity of DNPs was evaluated by 3-(4,5-dimethylthiazol-2-yl)-2,5-diphenyltetrazolium bromide (MTT) assay, a method based on the reduction of MTT by cellular oxidoreductases of viable cells, that yield a crystalline blue formazan product. Human lung epidermoid carcinoma cells (H1355) were incubated with different concentrations of DNPs for 24, 48 and 72 h. The results obtained are reported in Figure 4.5. The exposure of H1355 cells to increasing nanoparticle concentrations (20 μg/mL, 100 μg/mL, 200 μg/mL and 300 μg/mL) induced very low toxicity being the average viability of the cells slightly lower than 100%. This result also demonstrated that the irregular shape of DNPs did not influence cell growth and morphology. In conclusion, the MTT assay showed that H1355 cell viability was not affected even after 72 h of exposure to DNPs concentration up to 300 μg/mL, thus confirming their usability as nanovectors in nanomedicine [25, 26]. NPs cell uptake was studied by using labelled-DNPs and confocal microscopy analysis. Purified NPs were amino modified with a 5% (v/v) APTES solution in absolute ethanol, stirring 1 h at room temperature. After this step, the sample was centrifuged

for 30 min at 13.500 rpm and supernatant discarded. The functionalized DNPs were washed twice with absolute ethanol and the collected pellet was incubated for 10 min at 100°C (curing process). The silanization of DNPs was evaluated by FTIR spectroscopy. The comparison between FTIR spectra of bare NPs (A) and APTES-functionalized powders (B) is reported in Figure 4.6. The peak of Si–O–Si bond at 1100 cm^{-1}, characteristic of diatomite frustules, is well evident in both spectra. Before APTES functionalization, it is also detected the peak at 3700 to 3200 cm^{-1} corresponding to Si–OH group. The spectrum of functionalized sample showed the silane characteristic peaks in the range between 1800 and 1300 cm^{-1} (see the inset of Figure 4.6); in particular, the peak at 1655 cm^{-1}, corresponding to imine group and the peak at 1440 cm^{-1}, corresponding to asymmetric deformation mode of the CH_3 group, were observed [27]. FTIR characterization clearly demonstrated the silanization of silica nanoparticles. Diatomite NPs were labelled by tetramethylrhodamine isothiocyanate (TRITC).

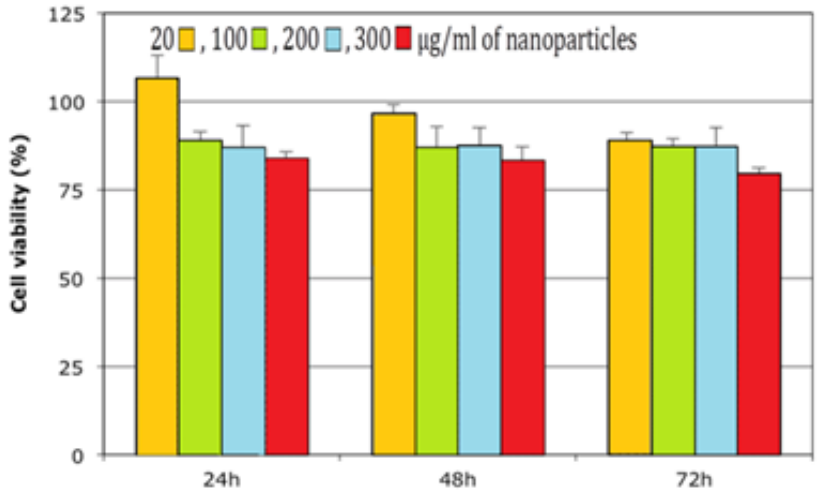

Fig. 4.5. *Cytotoxicity assessment of DNPs using MTT assay. Cell viability of H1355 cells treated with 20, 100, 200 and 300 µg/ml of NPs for 24, 48 and 72 h at 37 °C. Data represent the mean ± s.d. (n=3). Cell viability was expressed as the percentage of viable cells compared with cells cultured without nanoparticles as control (100%).*

H1355 cells have been incubated with the labelled NPs (DNPs*) at increasing concentrations (5, 10, 15, µg/mL) for 24 h. Figure 4.7 shows representative confocal microscopy images of cells treated with DNPs* compared to untreated cells as control. Cell nuclei were stained with Hoechst 33342 (blue), cell membranes were stained with WGA-Alexa Fluor 488 (green), and DNPs were labelled with TRITC (red). Images show an increase of fluorescence intensity at increasing labelled-DNPs concentration and a homogeneous particles distribution in the cytoplasm.

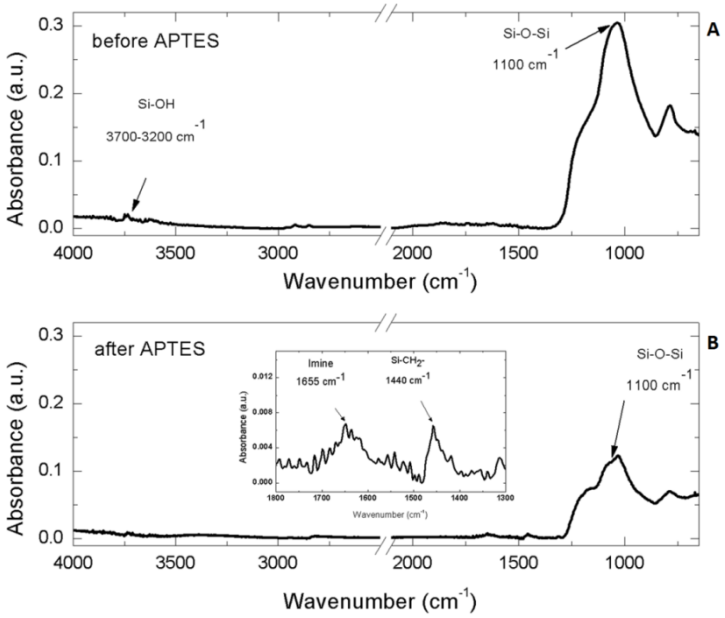

Fig. 4.6. *FTIR spectra of DNPs before (A) and after (B) APTES functionalization.*

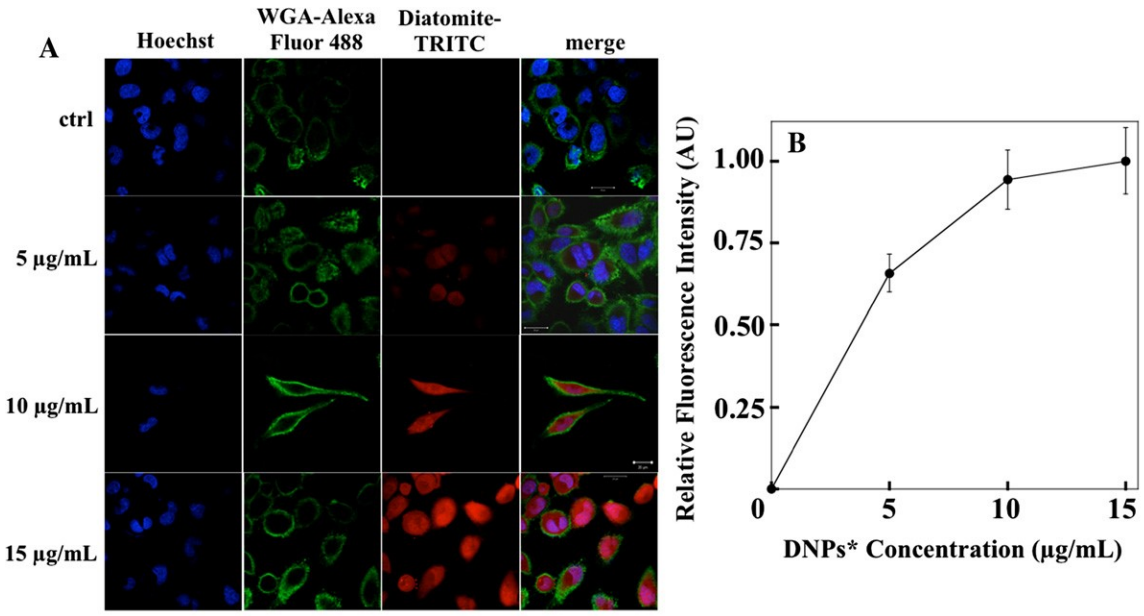

Fig. 4.7. *Confocal microscopy images of H1355 cells incubated with different concentrations of DNPs* (A), and cell fluorescence intensity analysis (B). Scale bar corresponds to 20 µm.*

The cell fluorescence intensity *vs* labelled NPs concentration is reported in Figure 4.7 B; fluorescence values were calculated for each cell from the TRITC images of Figure 4.7A. Data showed an increase of the fluorescence intensity up to about 10 µg/mL. A saturation of the signal can be observed for NP concentrations higher than 10 µg/mL. To prove the internalization of the carriers in the cells, images at different focal depth were recorded. Figure 4.8 shows that going from upper cell surface to the focus inside the cells, an increase

of red diatomite fluorescence can be observed thus indicating the uptake of labelled-DNPs by H1355 cells. These results showed that an efficient NPs uptake into the cytoplasm of cancer cells, demonstrating that DNPs could represent a promising tool for the delivery of anticancer molecules.

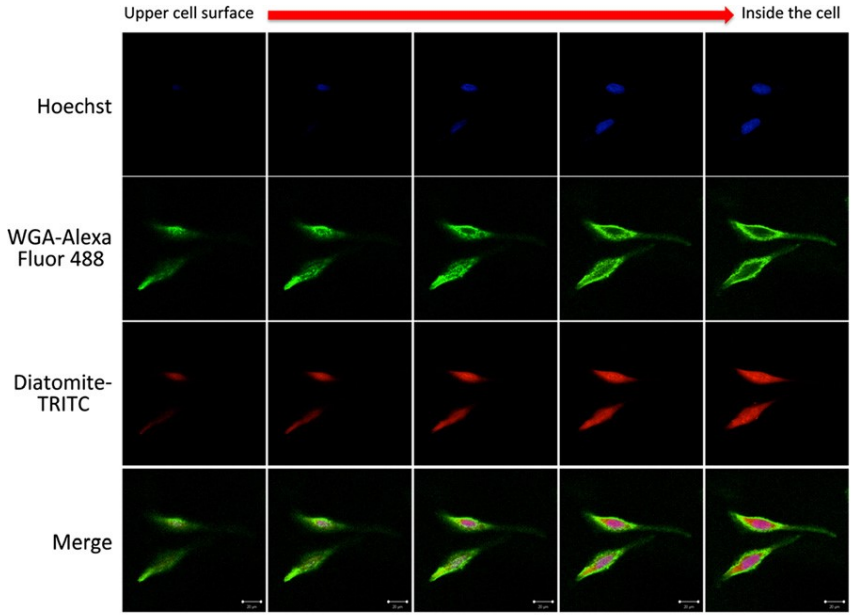

Fig. 4.8. *Confocal microscopy image with different focal depth of H1355 cells incubated with 10 μg/mL of DNPs*.*

4.3 References

1. D. Losic, J. G. Mitchell, N. H. Voelcker, *Adv. Mater.*, 2009, **21**, 2947–2958.
2. M. S. Aw, S. Simovic, Y. Yu, J. Addai-Mensah, D. Losic, *Powder Technol.*, 2012, **223**, 52–58.
3. M. Sumper, E. Brunner, *Adv. Funct. Mater.*, 2006, **16**, 17–26.
4. H. Zhang, M. A. Shahbazi, E. Mäkilä, T. H. da Silva, R. L. Reis, J. Salonen, J. T. Hirvonen, H. A. Santos, *Biomaterials*, 2013, **34**, 9210–9219.
5. M. A. Ferrara, P. Dardano, L. De Stefano, I. Rea, G. Coppola, I. Rendina, R. Congestri, A. Antonucci, M. De Stefano, E. De Tommasi, *PLoS ONE*, 2014, **9**, 103750.
6. L. De Stefano, I. Rendina, M. De Stefano, A. Bismuto, P. Maddalena, *Appl. Phys. Lett.*, 2005, **87**, 233902.
7. J. Parkinson, R. Gordon, *Trends Biotechnol.*, 1999, **17**, 230–232.
8. T. Fuhrmann, S. Landwehr, M. El Rharbi-Kucki, M. Sumper, *Appl. Phys. B*, 2004, **78**, 257–260.
9. P. J. Lopez, J. Descles, A. E. Allen, *Curr. Opin. Biotechnol.*, 2006, **16**, 180–186.
10. S. Lettieri, A. Setaro, L. De Stefano, M. De Stefano, P. Maddalena, *Adv. Funct. Mater.*, 2008, **18**, 1257–1264.
11. F. Xu, Y. Wang, X. Wang, Y Zhang, Y. Tang, P. Yang, *Adv. Mater.*, 2003, **15**, 1751–1753.
12. R. B Vasani, D. Losic, A. Cavallaro, N. H. Voelcker, 2015, *J. Mat. Chem. B,* **3**, 4325–4329.

13. IARC Monographs, No. 68, 1997.
14. O. Şan, R. Gören, C. Özgür, *Int. J. Miner. Process*., 2009, **93**, 6–10.
15. Y. Wang, J. Cai, Y. Jiang, X. Jiang, D. Zhang, *Appl Microbiol Biotechnol* 2013, **97**,453–462.
16. Q. Xiaohua, L. Mingzhu, C. Zhenbin, L. Rui, *Adv. Technol*., 2007,1**8**, 184–193.
17. E.M. Bens, C.M. Drew, *Nature,* 1967, **216**, 1046.
18. M. J. Carter, I. D. Milton, *Nucleic Acids Res.,*1993, **21**, 1044.
19. M. A. M. Khraisheh, M. A. Al-Ghouti, S. J. Allen, M. N. Ahmad, *Water Res.* 2005, **39** ,922–932.
20. L. De Stefano, P. Maddalena, L. Moretti, I. Rea, I. Rendina, E. De Tommasi, V. Mocella, M. De Stefano, *Super Lattice Microst*., 2009, **46**, 84–89.
21. J. O. Martinez, B. S. Brown, N. Quattrocchi, M. Evangelopoulos, M. Ferrari, E. Tasciotti, *Chin. Sci. Bull*., 2012, **57**, 3961–3971.
22. M. J. Sailor, J-H. Park, *Adv Mater* , 2012, **24**,3779–3802.
23. A. Setaro, S. Lettieri, P. Maddalena, L. De Stefano, *Appl. Phys. Lett.* 2007, **91**, 051921.
24. V. P. Torchilin, *Nanoparticulates as drug carriers*. Imperial college press, 2006.
25. R. E. Serda, J. Gu, J. C. Bhavane, X.W. Liu, C. Chiappini, P. Decuzzi, M. Ferrari, *Biomaterials*, 2009, **30**, 2440–2448.
26. R. E. Serda, B. Godin, E. Blanco, C. Chiappini, M. Ferrari, *Biochim. Biophys. Acta*, 2011, **1810**, 317–329.
27. G. Socrates, *Infrared and Raman characteristic group frequencies: tables and charts*, John Wiley & Sons, 2004.

5 BIONGINEERED DIATOMITE NANOVECTORS FOR DRUG DELIVERY IN CANCER THERAPY

(Papers J6, J7, P5)

The application of nanotechnology in the cancer therapy is expected to solve a number of issues associated with conventional therapeutic agents, including lack of targeting capability, nonspecific distribution, systemic toxicity, and low therapeutic index [1, 2]. Nanotechnology has provided the opportunity to get direct access of the cancerous cells selectively with increased drug localization and cellular uptake, making the therapy more patient compliance and efficient. Moreover, nano-based systems allow delivery of poor water solubile molecules (at least, most the anticancer drugs) difficult to administer and can also protect the new therapeutic molecules such oligonucleotide analogs (e.g., siRNA) from degradation, preserving their therapeutic efficacy while in blood circulation [3, 4]. Thus, the aim of nanomedicine in cancer therapy is the production of nanoscale devices to enhance the bioavailability of drug molecules, improving the tumor-targeting and reducing the systemic drug toxicity. In this Chapter the realization of biofunctionalized DNPs for drug delivery in cancer cells is described. Since the silica surface of diatomite is covered by silanol (SiOH) groups, it can be easily modified with functional reactive groups ($-NH_2$, −COOH, −SH, and −CHO) for the conjugation of biomolecules (e.g., DNA, antibodies, and enzymes) in order to prepare bioengineered devices. Different functionalization procedures for the preparation of bioengeneered DNPs are described, and the results on the effective enhancement of the DNPs'physicochemical properties, biocompatibility, cellular uptake and drug delivery, are presented.

5.1 Diatomite biosilica nanocarriers for siRNA transport inside cancer cells

The availability of the human genome sequence has revolutionized the strategy of employing nucleic acids with sequences complementary to specific target genes as new promising tools for therapeutic targets [5]. Development of sequence-specific DNA or RNA analogs that can block the activity of selected genetic sequences offers the possibility of rational design with high specificity, lacking in many current drug treatments for various diseases, at relatively inexpensive costs. Molecular therapy using small interfering ribonucleic acid (siRNA) has shown to be a powerful approach for silencing gene associated with a variety of pathologic conditions caused by abnormal gene overexpression or mutation, such as various cancers, viral infections, and genetic disorders [6]. However, siRNA require delivery carriers for

protection from nucleases and other environmental agents and to facilitate entry into the cell, thus improve its systemic delivery. Its conjugation to nanovectors (including liposomes, gold, magnetic and porous silicon nanoparticles, quantum dots) results to be possible strategies to overcome these challenging problems [7, 8].

5.1.1 Study of siRNA loading into diatomite nanoparticles (DNPs) and *in vitro* release

Porous diatomite nanocarriers were bioconjugated with siRNA in order to test their drug delivery capability. Labelled-siRNA (siRNA*) complexed with a poly D-Arg peptide, was loaded onto APTES-modified DNPs, following the functionalization procedure sketched in Figure 5.1.

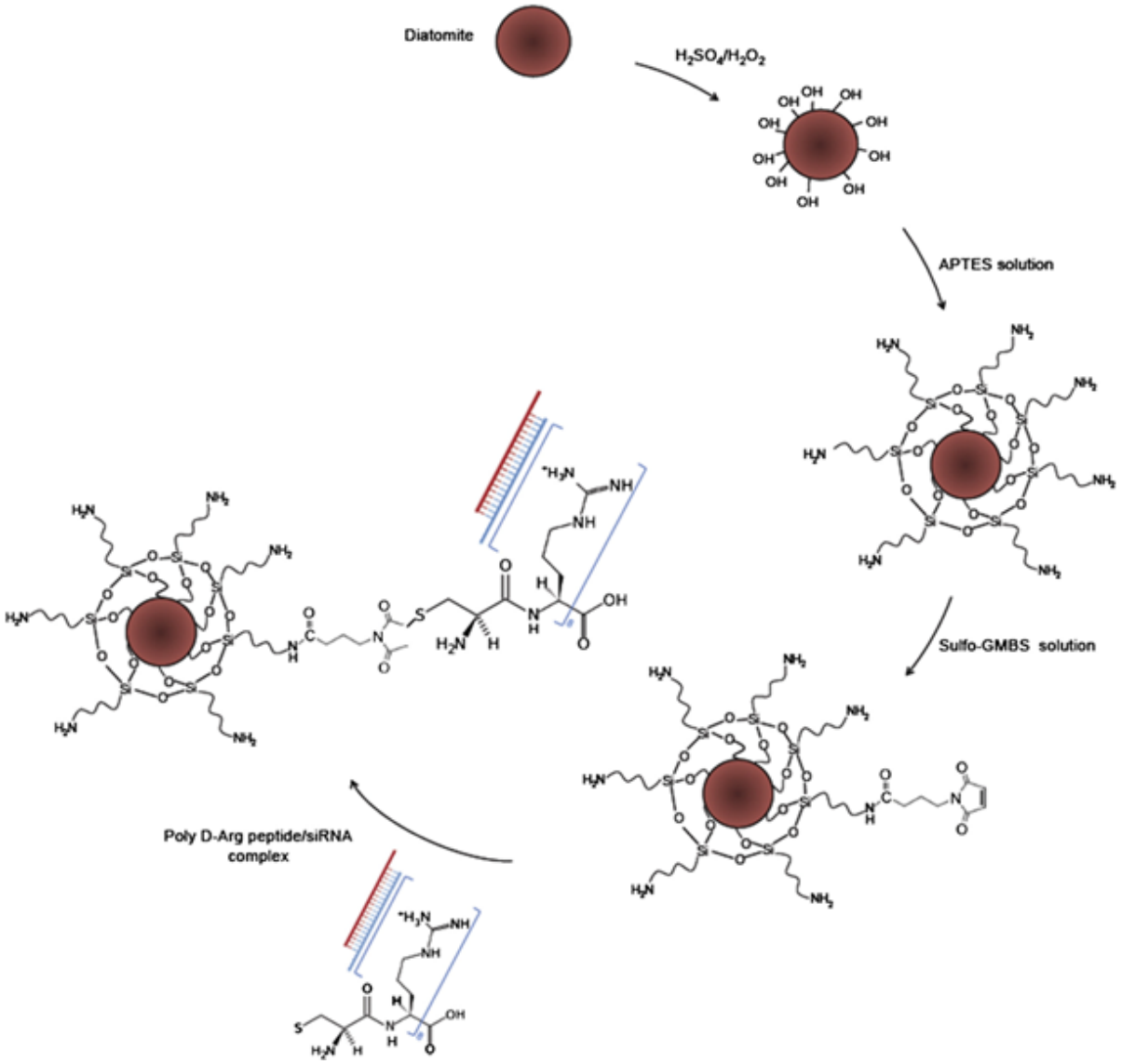

Fig. 5.1. *Functionalization scheme of diatomite NPs with labelled siRNA (siRNA*).*

Briefly, APTES-modified functionalized DNPs react with N-(γ-maleimidobutyryloxy) sulfosuccinimide ester (sulfo-GMBS), a heterobifunctional cross linker reactive to amino groups at one end and to sulfhydryl groups at the other. The N-hydroxysuccinimide (NHS) ester reacts with the amino-modified DNPs' surface as a nucleophile with release of the sulfo-NHS leaving the group forming an amide bond. Peptide/siRNA* complex (molar ratio 20:1) was immobilized on the DNPs' surface through the thioether bond between the sulfhydryl group of peptide cysteine residue and C\C bond of the maleimide ring of sulfo-GMBS. A nonpolar homopeptide was used as control for aspecific interactions with siRNA. The molar ratio peptide/siRNA* used in the functionalization procedure has been established by a gel shift assay, highlighting the complex electrostatic interaction as function of the positive peptide (NH_3^+)/negative RNA ($PO4^-$) charge ratios. siRNA (50 pmol) was mixed with arginine peptides at various N/P ratios (0–2). The results showed that the electrophoretic migration of RNA was retarded with an increasing ratio of peptide/RNA (Figure 5.2A). The intensity of the siRNA band decreased as the N/P ratio increased. No siRNA band was observed at the N/P ratio of 20. This absence of migration was probably due to the complete neutralization of nucleic acid charge by the arginine peptide and/or formation of a large complex between the arginine and siRNA. These results strongly suggest that an arginine peptide made of 8 residues could be sufficient to form a complex with a siRNA. In addition, the capability of the peptide/siRNA complex to protect siRNA from nuclease degradation was investigated. For this purpose, human pancreatic ribonuclease (HP-RNase) able to degrade double-strand RNA, was used [9].

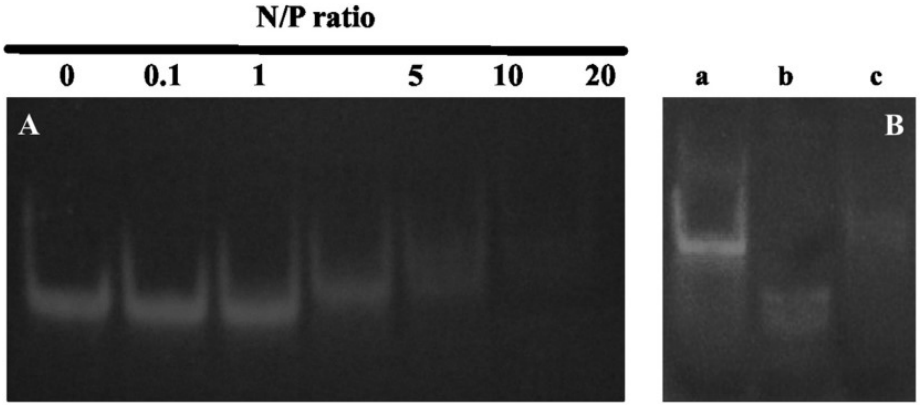

Fig. 5.2. *(A) Poly D-Arg peptide (N) and siRNA (P) were incubated at different molar ratios (range 0–20, as indicated above each lane) and the formed complex was analyzed by gel shift. (B) Effect of HP-RNase on siRNA degradation; siRNA alone (lane a), siRNA incubated with HP-RNase in absence (lane b) or in the presence (lane c) of poly D-Arg peptide.*

As shown in Figure 5.2 (B), siRNA was rapidly degraded by HP-RNase (lane b), while, when preincubated with peptide before adding RNase, no significant degradation was observed (lane c). The results confirmed that a poly D-Arg peptide strongly interacts with siRNA forming a highly stable complex [9, 10]. Furthermore, the formation of the peptide/siRNA complex improved the siRNA stability protecting it from nuclease degradation [11].

The capability of loaded DNPs to release siRNA* in solution was evaluated by fluorescence intensity measurement of both supernatant and DNPs as function of time (Figure 5.3). siRNA was released into supernatant in two phases: an initial phase of 12 h (burst release), followed by slow and sustained release phase over 48–72 h. The fluorescence profile of DNPs showed an opposite trend. The slow siRNA release observed was probably due to the progressive weakening of the electrostatic interactions between peptide and nucleic acid.

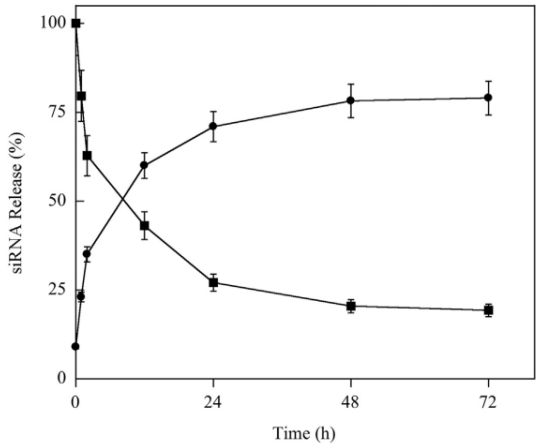

Fig. 5.3. *Fluorescent labelled siRNA bound to DNPs (DNPs–siRNA*) was incubated in 20mM Tris–HCl and 20mMNaCl, pH 7.5 at 37 °C and at time intervals the fluorescence intensity was measured in the sample supernatant (●) and diatomite (■).*

5.1.2 siRNA-modified DNPs: cellular internalization and gene silencing

H1355 cells were incubated with siRNA* modified DNPs (DNPs–siRNA*) to evaluate the siRNA uptake and cellular internalization. Figure 5.4 shows a representative confocal microscopy image of cells treated with DNPs–siRNA* compared to untreated cells as control. Fluorescence images show cell nuclei stained with Hoechst 33342 (blue) and cell membranes with WGA-Alexa Fluor 488 (green). Confocal microscopy analysis was performed after treatment with DNPs–siRNA* for 24 h. In Figure 5.4 the presence of siRNA (labelled with Dy547, red) into the H1355 cells treated with DNPs–siRNA* is evident. Merging the image shows that siRNA molecules are localized in the cytoplasm. Red fluorescence (siRNA*) was found as both spots and diffuse signal [12–14].

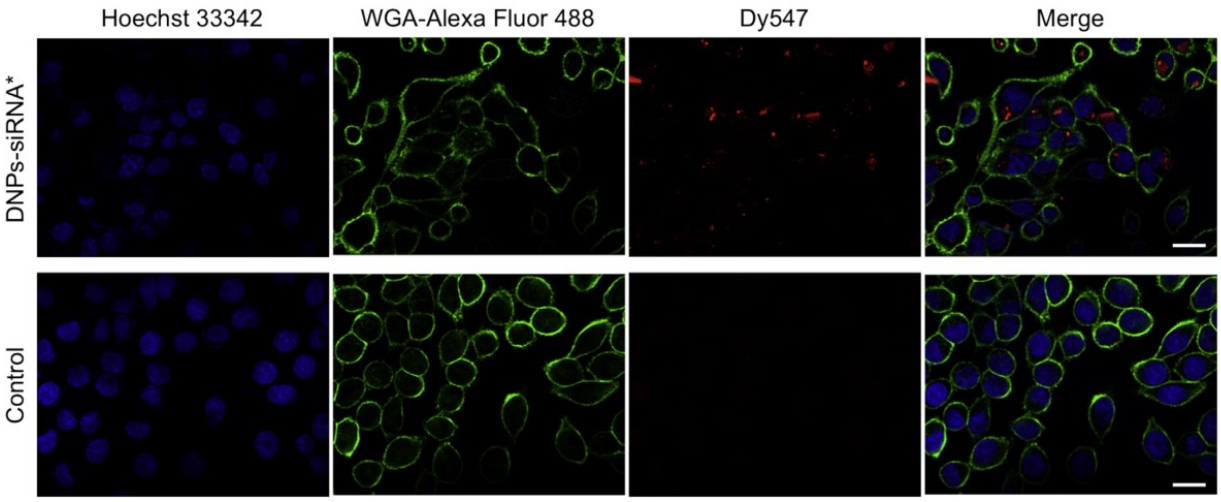

Fig. 5.4. *Confocal microscopy of cells treated with siRNA*modified DNPs. Scale bar corresponds to 20 μm.*

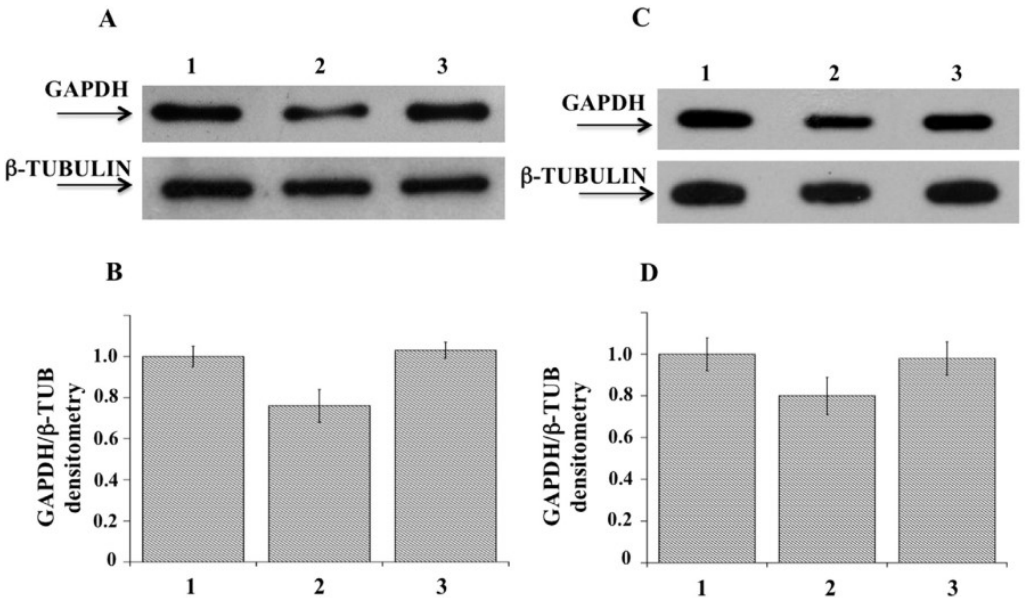

Fig. 5.5. *(A) Immunoblotting analysis of GAPDH (upper gel) and of β-tubulin (lower gel) of protein expression in DNPs–siRNA treated cells. Lanes: 1) control cells; 2)DNPs–GAPDH–siRNA; 3) DNPs–SCR–siRNA. (B) Densitometric intensity band ratio of GAPDH and β-tubulin used as internal control. The intensities of the bands were expressed in arbitrary units.(C) Immunoblotting analysis of GAPDH (upper gel) and of β-tubulin (lower gel) protein expression in lipofectamine-siRNA transfected cells. Lanes: 1) control cells; 2) GAPDH–siRNA; and 3) SCR–siRNA. (D) Densitometric intensity band ratio of GAPDH and β-tubulin used as internal control. The intensities of bands were expressed in arbitrary units. Each measurement and Western blot was carried out in triplicate. Error bars indicate the maximum deviation from the mean value of two independent experiments.*

The efficiency of DNPs–siRNA* internalization was quantified by fluorescence microscopy: counting the number of red fluorescent cells and the total number of cells (determined in bright field), a ratio of about 75% was calculated. Finally, the ability of the DNPs–siRNA complexes to silence in H1355 cells targeted mRNA was investigated by Western blot analysis. In particular, a siRNA against glyceraldehyde 3-phosphate dehydrogenase (GAPDH) and a scramble siRNA as control were used. Moreover, to compare the efficiency of the DNPs–siRNA delivery system with that of other system, the commercially available Lipofectamine 2000 transfection reagent was used. The obtained results are reported in Figure 5.5. Compared to untreated cells, GAPDH protein expression level after incubation of the cells with DNPs–siRNA complexes at 37 °C for 48 h was reduced (Panel A, upper gel) of about 22% (lane 2) as evaluated from the densitometric intensity of the bands (Panel B). Cells incubated with DNPs–SCR–siRNA (lane 3) showed instead almost identical protein expression level as control (lane 1), thus demonstrating the selective inhibition by siRNA. Panels C and D report the expression level and the densitometric analysis, respectively, of cells transfected with lipofectamine. In this case, GAPDH protein expression level (lane 2) was down-regulated of about 20%. Even if the delivery efficiency of DNPs and lipofectamine 2000 was similar, the use of diatomite as nanocarrier is more suitable for medical applications since it allows: (1) slow release of the loaded drug; (2) loading with one or more different molecules (e.g., siRNA + drug); (3) biocompatibility of the system; and (4) selective targeted functionalization to improve the delivery of anti-tumoral molecules to a specific cell population. The results obtained endorse DNPs as innovative nanocarriers for siRNA transport in cancer cells highlighted the non-toxic nature of the material, the effective cellular uptake and gene silencing in cancer cells.

5.2 Enhancement of DNPs stability, biocompatibility and cellular internalization in cancer cells

The main peculiarities of NPs as drug delivery systems are their low toxicity, high stability, biocompatibility, and suitability for cellular uptake. Several reports in the literature have demonstrated the enormous advantages arising from using polymers in the design of drug nanocarriers, such as the reduction of non-specific aggregation in aqueous medium and the increase of NPs stability, biocompatibility, drug loading, and cellular internalization [12–14]. The enhancement of the NPs' cellular uptake is one of the key issues in drug delivery; however, the cell membranes prevent drug carriers from entering the cells, unless an active transport mechanism is involved [15]. An efficient approach to deliver NPs or molecules

within the cells is to bind them to peptides that can cross the cellular membranes, enhancing their translocation inside the cells. Cell penetrating peptide (CPP) bioconjugation has been proved as a valid strategy to improve the intracellular drug delivery of conventional small drug molecules, NPs or oligonucleotide, and peptide-based therapeutics, increasing their systemic diffusion due to the CPP's property to overcome the lipophilic barrier of the cellular membranes and deliver these therapeutics inside the cells [16, 17]. Herein, for the first time, a valid biofunctionalization based on PEGylation and CPP biocongiugation able to improve the aqueous stability of DNPs, enhancing their hemocompatibility, minimizing their cytotoxicity, and increasing the solubility of a poorly water-soluble anticancer model drug, sorafenib was demonstrated. In order to obtain an effective DNPs PEGylation, the bare NPs were hydroxylated by Piranha solution, thus increasing the reactivity of their silica surface, by introduction –OH groups. Covalent bond between PEG and DNPs requires the DNPs salinization using an APTES solution, which introduces the highly reactive amino groups (–NH_2) onto the NPs surface (DNPs-APT) that can be covalent conjugated with the carboxyl groups of PEG molecules using 1-ethyl-3-(3-dimethylaminopropyl)carbodiimide (EDC)/NHS chemistry (Scheme 5.1, I) [18, 19]. Without this double-step chemical surface treatment, it would not be possible to obtain stable covalently-bonded PEG or CPP DNPs complexes. Due to the polymer solubility in water and in a wide variety of organic solvents used during the NPs modification, it is crucial that the polymer is covalently bound onto the NPs' surface in order to avoid its untimely detachment [18, 19] To improve the DNPs' cellular uptake, the free amino groups of DNPs-APT-PEG were further chemically conjugated with the carboxyl groups of CPP-peptide, known to highly facilitate the delivery of cargos (*e.g.*, peptides, proteins, genes, and even nanoparticles) across the cell membrane, by EDC/NHS chemistry (Scheme 5.1, II) [20].

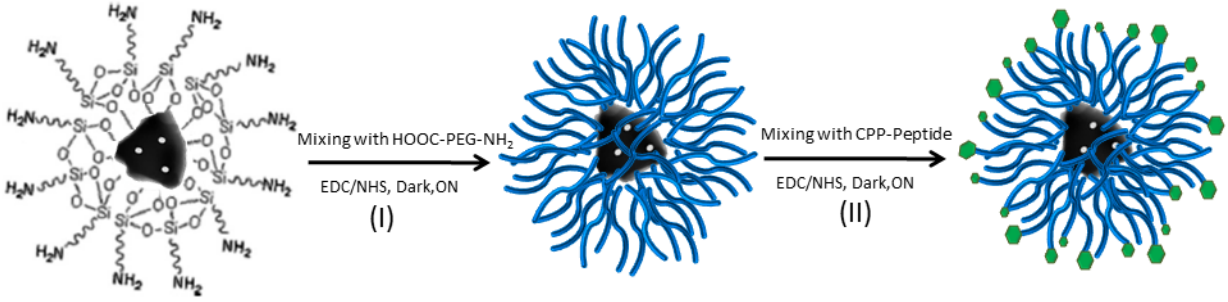

Scheme 1. *Schematic representation of the DNPs functionalization. Reaction I, the PEGylation of DNPs-APT (I) via EDC/NHS, under stirring ON at RT. Reaction II,CPP-peptide bioconjugation of DNPs-APT-PEG via EDC/NHS, under stirring ON at RT.*

The DNPs were characterized before and after the surface modification by DLS, analysing the hydrodynamic diameter, the PDI, and the surface charge ζ-potential of the particles. An increase of the particles' size from 317 ± 8 nm to 364 ± 3 nm (DNPs-APT) after the APTES solution treatment was observed, confirming the successful of silanization process. A progressive decrease of the nano-aggregates' size was observed after PEGylation and CPP bioconjugation. The NPs' size decreased from 364 ± 3 nm (DNPs-APT) to 346 ± 4 nm after PEGylation (DNPs-APT-PEG), and to 340 ± 8 nm after CPP-conjugation (DNPs-APT-PEG-CPP). This result is due to an increase of the DNPs' surface repulsion forces of the modified surface (DNPs-bare, −19.2 ± 2.0 mV; DNPs-APT, +19.8 ± 3.0 mV; DNPs-APT-PEG, +35.6 ± 1.5 mV; DNPs-APT-PEG-CPP, +40 ± 2 mV), which can be attributed to the positive charge of PEG and CPP-peptide onto the NPs' surface. As a result, the DNPs stability was improved in aqueous solution and a decrease in the PDI of the NPs was also observed (data not shown).

The chemical silanization, PEGylation and CPP-conjugation of DNPs were further analysed by ATR–FTIR spectroscopy. Figure 5.6 shows the progressive change of DNPs FTIR spectra after each modification step. All spectra of DNPs showed an intense band at 1100 cm^{-1} that corresponds to Si-O-Si bonds, because silica is the main constituent of the diatomite frustules.

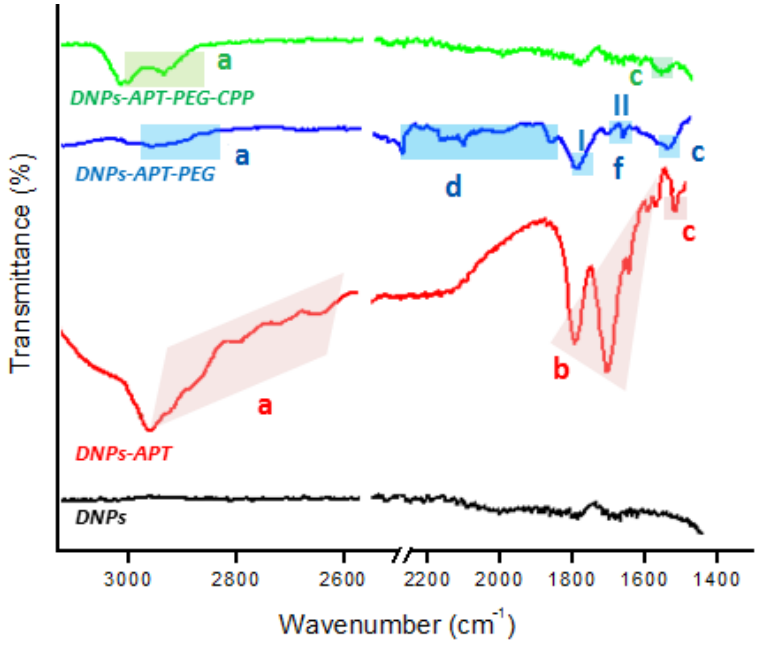

Fig. 5.6. *ATR–FTIR spectra of modified-DNPs. DNPs were characterized before the biofunctionalization (black line), after the silanization process (red line), after the PEGylation (blue line), and also after the CPP-peptide bioconjugation (green line). The* ***a*** *indicates* CH_x *stretching vibration,* ***b*** *the bending mode of the free* NH_2*,* ***c*** *the C–N stretching,* ***d*** *the C–H bending vibrations, and* ***f-I*** *and* ***f-II*** *N–H bending vibration and the C–N stretching vibration, respectively.*

After the silanization process, the DNPs-APT displayed the typical bands of APTES corresponded to the CH_x stretching at 2941–2570 cm^{-1}, the bending mode of the free NH_2 at 1630–1470 cm^{-1}, and the C-N stretching at 1385 cm^{-1}[21, 22]. After the PEGylation, the DNPs-APT-PEG showed the stretching bands of CH_x at 2960–2849 cm^{-1}, the C-H bending vibrations at 2160–1722 cm^{-1}, the amide I band at 1640 cm^{-1} associated to the C=O stretching vibration, the amide II resulted from the N–H bending vibration, and the C–N stretching vibration at 1580 and 1360 cm^{-1}, respectively, thus confirming the covalent binding of the PEG molecules onto the NPs' surface [22]. After incubation with the CPP-peptide, the DNPs-APT-PEG-CPP displayed a band at 2984–2881 cm^{-1}corresponding to the CH_x stretching, and at 1930 cm^{-1}assigned to the C–N stretching of amide II, confirming the successful CPP-peptide bioconjugation to the surface of the NPs [23, 24].

5.2.1 Hemocompatibility test of modified-DNPs

The hemotoxicity, based on the %-lysed red blood cells (RBCs), is an important preclinical study to evaluate the level of the NPs hemocompatibility, in order to avoid serious risks to human health (e.g., after intravenous injection of NPs), considering that the erythrocytes constitute a large volume portion of the blood. Moreover, if NPs induce hemolysis, there is a higher risk that blood constituents can react immunologically to inactivate the NPs, and thus, affecting their function and increasing their elimination by macrophages [25, 26].

In order to evaluate the impact of the modified-DNPs on RBCs, the hemocompatibility and the morphological studies of RBCs were determined after exposure to the modified-DNPs at increasing incubation times (1, 4, 24, and 48 h) and NP concentrations (25, 50, 100, and 200 µg/mL) [27]. The %-hemolysis determined by spectrophotometric analysis of the supernatants after 48 h incubation at the maximum concentration of modified-DNPs (200 µg/mL) was 34 % for DNP-APT, 7 % for DNP-PEG, and 1.3 % for CPP-DNP. This result clearly demonstrated that the biofunctionalization of the NPs improved the DNPs hemocompatibility (Figure 5.7).

The morphological changes of the RBCs after exposure to the modified-DNPs (200 µg/mL for 4 h, at RT) were examined by SEM characterization. The RBCs, in the presence of DNP-APT, completely altered their morphology, changing from the biconcave-like disks to shrinked shape, with consequent hemolysis (Figure 5.8). The DNPs-APT hemotoxicity is attributed to the free positive amine groups existing on the surface of the NPs, which strongly interact with the negative charge surface of the RBCs, resulting in hemolysis and changing of the cell's

shape. In the case of PEGylated particles, no severe change was observed in the RBCs morphology, but the cell membrane locally wrapped around with the appearance of small holes without significant hemolysis. The relevant decrease of the DNPs-APT hemotoxicity after PEGylation is due to the improved biocompatibility of the NPs as a result of the presence of PEG on their surface, which is known to be relatively non-cytotoxic, non-immunogenic, non-antigenic, and decrease the protein interaction [28, 29]. In the case of DNPs-APT-PEG-CPP, there was not relevant change observed in the RBCs' morphology due to the low cytotoxicity of CPP-peptide, which improved the DNPs biocompatibility [30]. Therefore, both the amino function and also the charge density (the number and special arrangements of the cationic residues) is an important factor for toxicity [31].

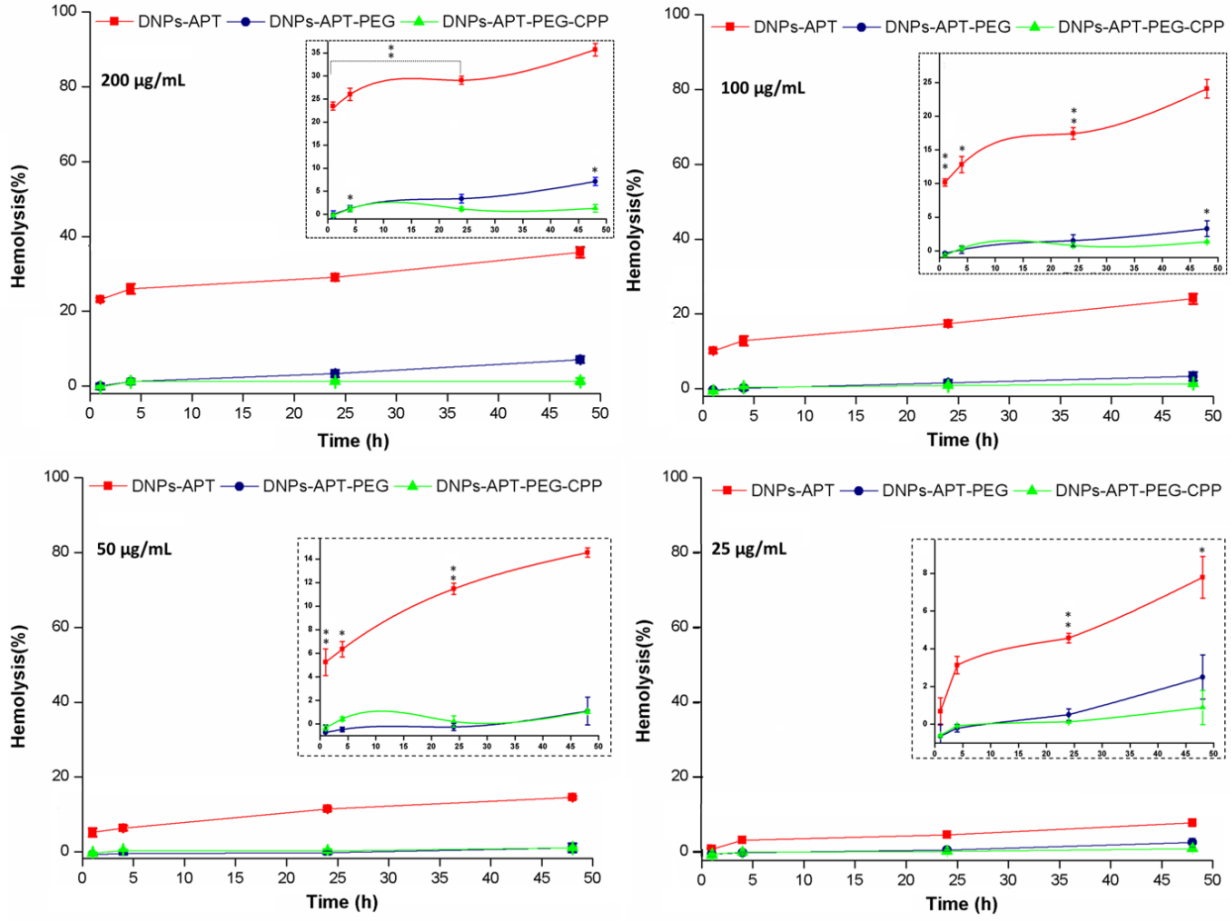

Fig. 5.7. *Hemocompatibility of the modified-DNPs. Hemotoxicity of APT-, PEG- and CPP-modified DNPs incubated for 48 h at different concentrations (25, 50, 100, and 200 µg/mL) with RBCs, estimated by spectrophotometric methods (577 nm) to analyse the amount of lysed-hemoglobin in the supernatants. The insert Figures show the magnifications of the graphs. Statistical analysis was made by ANOVA. The level of significance from negative control was set as probabilities of *p < 0.05**p < 0.01 and ***p < 0.001. Error bars represent s.d. (n = 3).*

A three-point attachment are necessary for eliciting a biological response on cell membranes and the activity of a molecule decreases when the space between reactive amino groups increases in the primary structure [31]. The arrangement of cationic charges on the molecules structure determines the accessibility of their charges to the cell surface [30]. This study confirms these observations, where APTES showed more toxicity than PEG and CPP, due to the simple molecule structure formed by short amino-alkyl chains of APTES, and thus, more accessibility of amino groups to interact with the cells. As shown in Figure 5.8, very small amounts of APT- and PEG-modified DNPs (indicated by white arrows) were adsorbed onto the RBCs' surface, while a considerable amount was observed for CPP-DNPs, thus this biofunctionalization significantly improved the DNPs–cells membrane interactions.

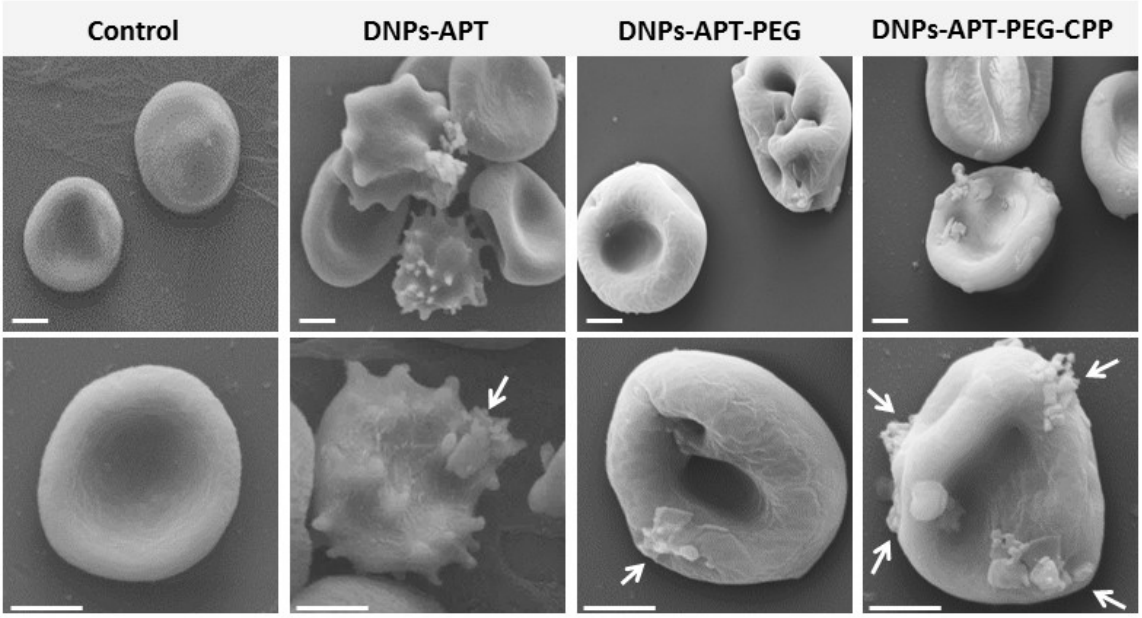

Fig. 5.8. *SEM pictures of the RBCs morphological modification after the exposure to the modified-DNPs. The modified DNPs (100 µg/mL) were incubated with RBCs for 4 h at RT. The DNPs-APT showed the higher toxicity than the PEG and CPP-modified DNPs, resulting in severe morphological changes of cell. The CPP-bioconjugation improved significantly the DNPs–cells membrane interactions, as indicated by white arrows. Scale bars are 3 µm.*

5.2.2 *In vitro* cell viability assay

The biocompatibility and toxicity of the DNPs were assessed by measuring the adenosine triphosphate (ATP) activity of the MCF-7 and MDA-MB-231 cells exposed to the bare and modified-DNPs, after 6 and 24 h of incubation time at different NP concentrations (25, 50, 100, and 200 µg/mL). The exposure of MCF-7 and MDA-MB 231 cells to increasing

concentrations of bare diatomite NPs within 24 h of incubation time induced very low toxicity, demonstrating their potential applicability as nanovectors in nanomedicine (data not shown). The modified-NPs showed the same degree of cytotoxicity on both cell lines, as shown in Figure 5.9. The DNPs-APT showed significant cytotoxic activity after 6 h of incubation and at lower concentration (25 µg/mL). By increasing the incubation time and the NPs concentration, in an increased cytotoxicity of the NPs, was observed. After PEGylation and CPP-bioconjugation to the DNPs-APT, the cytotoxicity was significantly decreased after 24 h of incubation compared to the negative control (HBSS–HEPES, pH 7.4). In addition, no significant dependency on the exposure time and NPs concentration was observed on the cytotoxicity of the PEGylated and CPP-biofunctionalized NPs. The toxicity of DNPs-APT can be attributed to the positive charge of free amino groups of APTES, as discussed previously. These results are in agreement with the hemotoxicity data, confirming an increase in the DNPs' biocompatibility after the functionalization with PEG and biofunctionalization with the CPP-peptide. These results further suggest that DNPs-APT-PEG-CPP could be used as nanocarrier for long incubation times and high concentrations.

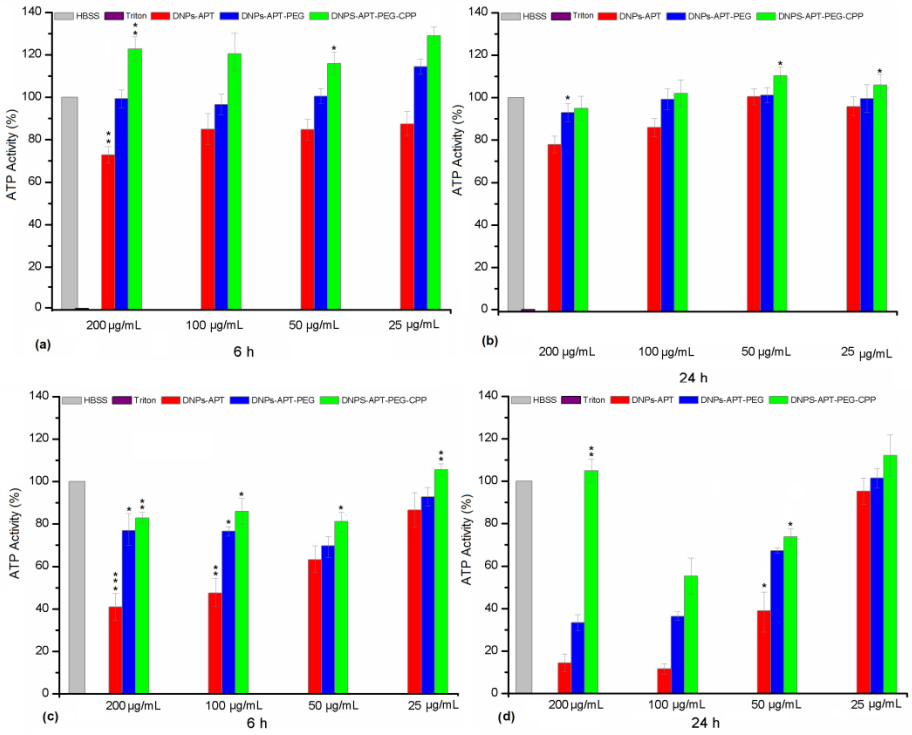

Fig. 5.9. *Cell viability of MCF-7 (a and b) and MDA-MB-231 (c and d) cells after exposure to the modified-DNPs at different concentrations. Statistical analysis was made by ANOVA comparing all data sets to the negative control HBSS (pH 7.4). The HBSS–HEPES (pH 7.4) and Triton X-100 were used as negative and positive controls, respectively. The level of significance was set at probabilities of* $^{*}p< 0.05$, $^{**}p< 0.01$, *and* $^{***}p< 0.001$. *Error bars represent s.d. (n = 3).*

5.2.3 Cellular uptake of the modified-DNPs

Another key requirement of the nanocarriers for drug delivery is the cellular internalization into cancer cells without damaging the cellular integrity of healthy cells; therefore, the surface chemistry of the NPs has a significant impact on the NPs performance in biomedical applications. Several peptides, capable of translocation in cellular membranes, have been used to improve the NPs' cellular uptake [32, 33]. The CPP-peptide used, consists of a short basic amino acid sequence with a net positive charge sequence and has the ability of facilitating the delivery into the cells of various molecular cargos, such as oligonucleotides, small molecules, siRNA, NPs, peptides and proteins [34]. The cellular uptake was evaluated by confocal fluorescence microscopy after DNPs and cellular membrane labelling with Alexa Fluor-488® and CellMask™ Deep Red, respectively. Initially, the cellular internalization of modified-DNPs was evaluated on MCF-7 at two different incubation times (6 and 12 h) in order to determine the time required for a satisfactory uptake. The best incubation time, regardless of the modified-DNPs type, was 12 h; while the NPs were localized prevalently in the cellular membranes after 6 h. In both the cell lines, an increase in the NPs' cellular uptake after CPP-bioconjugation was observed, as shown in Figure 5.10. The merge images of the CPP modified-DNPs showed a yellow colour, resulting from the co-localization of the green labelled-DNPs and red colour of cell membranes, which indicates the presence of the NPs inside the cells. In the case of the APTES-modified NPs, more cellular uptake was observed compared to the NPs functionalized with PEG, due to the presence of the free amino groups of APTES. The cellular uptake was also evaluated by TEM imaging of both cancer cells after 12 h of incubation with the modified-DNPs (50 μg/mL), confirming the results obtained for the confocal fluorescence microscopy studies. In Figure 5.11, the APTES-modified DNPs were mainly localized in the proximity of the cell membrane, while in the case of the DNPs-APT-PEG, no significant cellular uptake was observed. For the CPP-modified NPs, a considerable amount of DNPs was internalized into the cells with a homogeneous distribution into the cytoplasm and very close to the nucleus. All these results confirmed that the CPP bioconjugation is a valid functionalization strategy to increase the cell penetration of diatomite NPs. The benefit of CPP on the surface of the NPs is the ability to translocate into the intracellular compartment without causing any cell membrane damage, resulting in low cytotoxicity and high uptake efficiency [35–37].

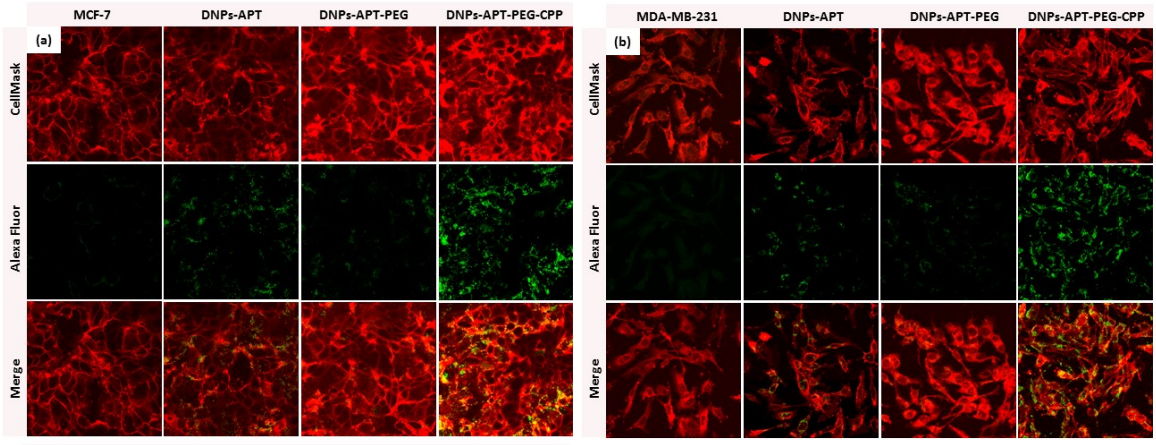

Fig. 5.10. *Confocal fluorescence microscopy of MCF-7 (a) andMDA-MB-231 (b) cells treated with APT-, APT-PEG, APT-PEG-CPP modified-DNPs for 12h at 37°C.*

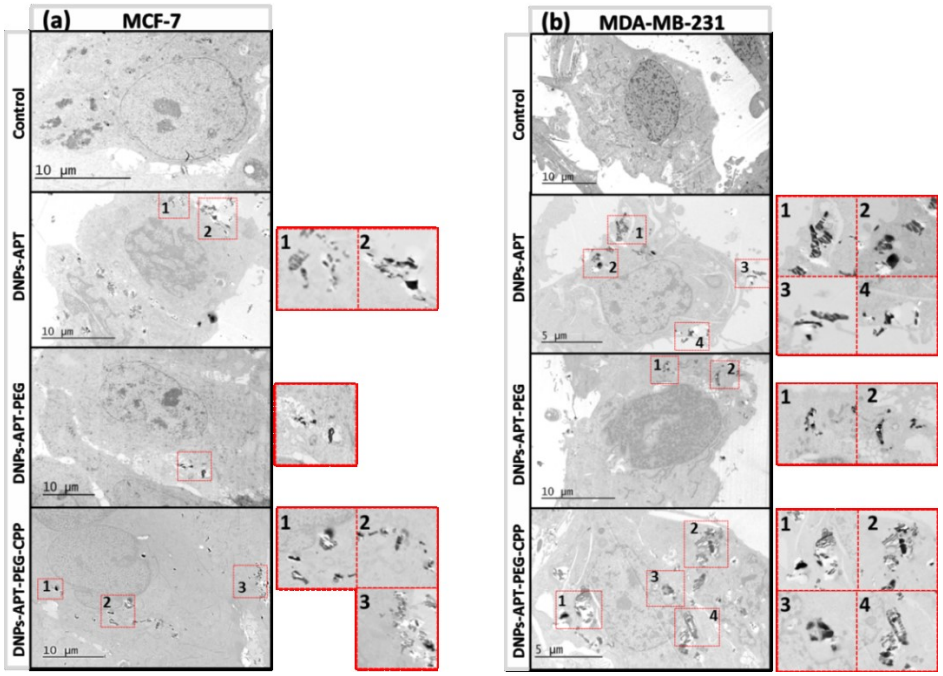

Fig. 5.11. *TEM images of MCF-7 (a) and MDA-MB-231 (b) cells treated with 50 µg/mL of DNPs-APT, DNPs-APT-PEG, and DNPs-APT-PEG-CPP for 12h at 37°C.*

5.2.4 Drug loading and release studies

The ultimate goal of targeted drug delivery is to deliver the administered drug to the target, while eliminating or minimizing the accumulation of the drug at any non-target site with minimal side effects [38]. In this context, the poorly water-soluble anticancer drug, sorafenib (SFN), was used as a model drug to investigate the loading efficacy in the modified-DNPs and the release profiles in aqueous buffer solutions at pH 7.4 and 5.5, mimicking the physiological and intratumoral pH, respectively. The multikinase inhibitor SFN, is considered a promising targeted protein kinase agent for the treatment of a broad range of cancers due to

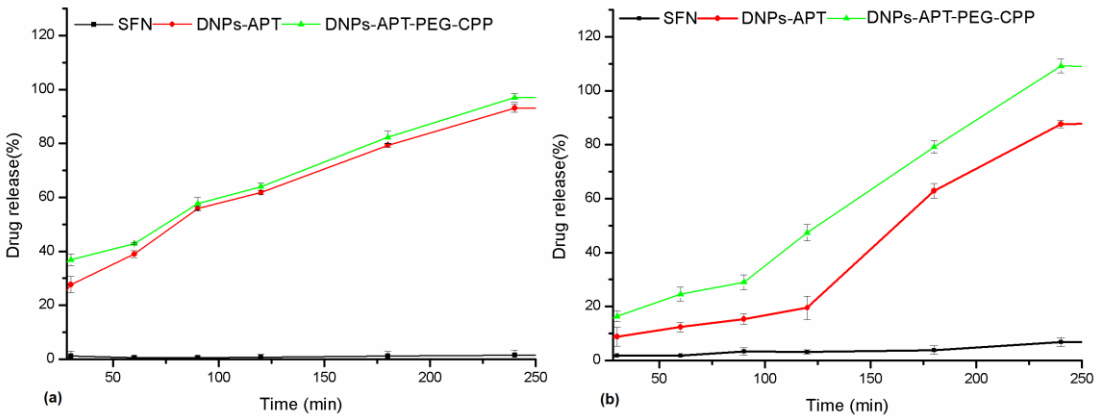

Fig. 5.12. *Drug release profiles of the SFN-loaded DNPs in HBSS-HEPES + 10 % FBS at pH 7.4 (a) and pH 5.5 (b) at 37 °C. Values represent the mean ± s.d. (n = 3).*

its significant both *in vitro* and *in vivo* antitumor activity, resulting in the tumor growth inhibition and disruption of tumor microvasculature through antiproliferative, antiangiogenic, and/or proapoptotic effects [39, 40]. Firstly, the loading degree of SFN in APT-, PEG-, CPP-modified DNPs was evaluated in order to determine the influence of the surface biofunctionalization on the drug loading. The loading degree of SFN was 10.4 ± 1.1% in the DNPs-APT, 22 ± 2 % in the DNPs-APT-PEG, and 17 ± 2% in the DNPs-APT-PEG-CPP. The surface biofunctionalization improved the drug loading, entrapping higher amounts of drug into the modified DNPs than in APTES alone. In the case of PEG-modified DNPs, an higher amount of the drug was loaded than in DNPs-APT, probably due to weak interactions (e.g., Van der Waals forces) between PEG and the SFN [43]. The CPP-conjugation step, even if it requires overnight bioconjugation time and several washes after the reaction, causes only a very small decrease in the drug loading, possibly due to some removal of the adsorbed PEG molecules that are not covalently bound to the NPs surface. The release profiles of SFN were assessed in HBSS–HEPES + 10% FBS solution at pH 7.4 and 5.5 (Figure 5.12). The dissolution of pure SFN within 24 h (data not shown) in the aqueous solution (pH 7.4 and 5.5) was negligible. In the case of SFN-loaded in APT- and CPP-modified DNPs, the drug release in both buffer solutions (pH 7.4 and 5.5) was gradual and constant within 4 h. SFN is characterized by its very poor water solubility, and the results show that the surface modification of DNPs improved the solubility of drug in aqueous solution, but the functionalization of DNPs with CPP did not significantly influence the release profile of the drug loaded. However, in view of DNPs use for *in vivo* drug release and anticancer studies, it should be recommended to use CPP-modified DNPs for the remarkable results of stability, biocompatibility and cellular uptake obtained here.

References

1. M. Ferrari, *Nat. Rev. Cancer*, 2005, **5**, 161–171.
2. O. C. Farokhzad, R. Langer, *ACS Nano* 2009, **3**, 16–20.
3. P. Parhi, C. Mohanty, S. K. Sahoo, *Drug Discov. Today*, 2012, **17,** 1044–1052.
4. R. van der Meel, L. J. Vehmeijer, R. J. Kok, G. Storm, E. V. van Gaal, *Adv. Drug. Deliv. Rev.*, 2013, **65**, 1284–1298.
5. G. R. Devi, *Cancer gene therapy*, 2006, **13**, 819–829.
6. J. M. Lee, Y. Tae-Jong, C. Young-Seok Cho, *BioMed Res. Int*., 2013, **2013**, 1–10.
7. K. A. Whitehead, R. Langer, D. G. Anderson, *Nat. Rev. Drug Discov*., 2009, **8**, 129–138.
8. W. X. Mai, H. Meng, *Integr. Biol*., 2013, **5**, 19–28.
9. S. Sorrentino, M. Naddeo, A. Ruso, G. D'Alessio, *Biochemistry*, 2003, **42**, 10182–10190.
10. P. Kumar, H. Wu, J. L. McBride, K. Jung, M. H. Kim, B. L. Davidson, S. K. Lee, P. Shankar, N. Manjunath, *Nature*, 2007, **448**, 39–43.
11. M. C. Morris, P. Vidal, L. Chaloin, F. Heitz, G. Divita, *Nucleic Acids Res*. 1997, **25**, 2730–2736.
12. M. A. Shahbazi, P. V. Almeida, E. Mäkilä, M. Kaasalainen, J. Salonen, J. Hirvonen, H. A. Santos, *Biomaterials*, 2014, **35**, 7488–7500.
13. H. Otsuka, Y. Nagasaki, K. Kataoka, *Adv. Drug. Deliv. Rev.*, 2012, **64**, 246–255.
14. Q. Gao, Y. Xu, D. Wu, Y. Sun, X. Li, *J. Phys. Chem. C*, 2009, **113**, 12753–12758.
15. A. Verma, O. Uzun, Y. Hu, Y. Hu, H. S. Han, N. Watson, S. Chen, D. J. Irvine, F. Stellacci, *Nat. Mater*., 2013, **12**, 588–595.
16. E. Koren, V. P. Torchilin, *Trends Mol. Med*., 2012, **18**, 385–393.
17. M. C. Shin, J. Zhang, K. A. Min, K. Lee, Y. Byun, A. E. David, H. He, V. C. Yang, *J. Biomed. Mater. Res*. *A*, 2014, **102**, 575–587.
18. Milton Harris (Ed), Springer US, 1992.
19. N. A. Alcantar, E.S. Aydil, J. N. Israelachvili, *J. Biomed. Mater. Res*., 2000, **51**, 343–351.
20. Y. Z. Huang, Y. F. Jiang, J. X. Wang, M.C. Shin, Y. Byun, H. He, Y. Liang, V. C. Yang, *Adv. Drug. Deliv. Rev*., 2013, **64**, 1299–1315.
21. E. T. Vandenberg, L. Bertilsson, B. Liedberg, K. Uvdal, R. Erlandsson, H. Elwing, I. Lundström, *J. Colloid. Interface Sci.*, 1991, **147**, 103–118.
22. G. Socrates, John Wiley & Sons, 2004.
23. D. Liu, H. Zhang, E. Mäkilä, J. Fan, B. Herranz-Blanco, C. F. Wang, R. Rosa, A. J. Ribeiro, J. Salonen, J. Hirvonen, H. A. Santos, *Biomaterials,* 2015, **39**, 249–259.
24. D. Schaer, A. I. Alayash, P. W. Buehler, *Antioxid. Redox Sign*., 2007, **9**, 991–999.
25. T. Yu, A. Malugin, H. Ghandehari, *ACS Nano*, 2011, 5, 5717–5728.
26. M. A. Shahbazi, M. Hamidi, E. Mäkilä, H. Zhang, P. V. Almeida, M. Kaasalainen, J. J. Salonen, J. T. Hirvonen, H.nA. Santos, *Biomaterials*, 2013, **34**, 7776–7789.
27. H. Wu, G. Liu, S. Zhang, J. Shi, L. Zhang, Y. Chen, F. Chena, H. Chen, *J. Mater. Chem*., 2011, **21**, 3037–3045.
28. Z. Zhang, M. Zhang, S. Chen, T. A. Horbett, B. D. Ratner, S. Jiang, *Biomaterials*, 2008, **29**, 4285–4291.
29. D. Fischera, Y. Lib, B. Ahlemeyerc, J. Krieglsteinc, T. Kissela, *Biomaterials*, 2003, **24**, 1121–1131.

30. H. J. P. Ryser, *Nature*, 1967, **215**, 934–936.
31. H. He, J. Ye, Y. Wang, Q. Liu, H.S. Chung, Y.M. Kwon, M. C. Shin, K. Lee, V. C., Yang, *J. Control. Release*, 2014, **176**, 123–132.
32. E. Jin, B. Zhang, X. Sun, Z. Zhou, X. Ma, Q. Sun, J. Tang, Y. Shen, E. Van Kirk, W. J. Murdoch, M. Radosz, *J. Am. Chem. Soc*., 2013, **135**, 933–940.
33. J. Jo, S. Hong, W. Y. Choi, D. R. Lee, *Sci. Rep*., 2014, **4**, 4378.
34. L. Vasconcelos, F. Madani, P. Arukuusk, L. Pärnaste, A. Gräslund, Ü. Langel, *Biochim. Biophys. Acta,* 2014, **1838**, 3118–3129.
35. M. Zorko, Ü. Langel, *Adv. Drug. Deliv. Rev*., 2005, **57**, 529–545.
36. S. W. Jones, R. Christison, K. Bundell, C. J. Voyce, S.M.V. Brockbank, P. Newham and M. A Lindsay, *J. Pharmacol.*, 2005, **145,** 1093–1102.
37. F. Madani, S. Lindberg, Ü. Langel, S. Futaki, A. Gräslund, *Biophys. J*., 2011, **2011**, 1–10.
38. Y. S. Kim, H. O. Jin, S. K. Seo, S. H. Woo, T. B. Choe, S. An, S. I. Hong, S. J. Lee, K. H. Lee, I. C. Park, *Biochem. Pharmacol*., 2011, **82**, 216–226.
39. M. A. Shahbazi, N. Shrestha, E. Mäkilä, F. Araújo, A. Correia, T. Ramos, B. Sarmento, J. Salonen, J. Hirvonen, H. A. Santos, *Nano Res*., 2015, **8**, 1505–1521.
40. Y. C. Li, S. Rissanen, M. Stepniewski, O. Cramariuc, T. Róg, S. Mirza, A. Bunker, *J. Phys. Chem. B*, 2012, **116**, 7334–7341.

6 EVALUATION OF DIATOMITE NANOPARTICLES TOXICITY IN LIVING ORGANISM *HYDRA*

The use of nanoparticles in experimental and clinical settings has exponentially revolutionised medical imaging, diagnostics, therapeutics as well as carry out biological processes [1–3]. This highlights the need to consider not only the usefulness of NPs but also the potentially unpredictable and adverse consequences in humans [4]. NPs toxicity refers to the ability of the particles to adversely affect the normal physiology as well as to directly interrupt the normal structure of organs and tissues of humans and animals. It is widely accepted that toxicity depends on physiochemical parameters such as particle size, shape, surface charge and chemistry, composition, and subsequent NPs stability [5–8]. *In vitro* toxicity testing is the most common scientific analysis used to determine the effects of NPs toxicity on cultured mammalian cells. However, the successful of *in vitro* assays is not predictive for promising *in vivo* results; for this reason the *in vivo* evaluation of NPs toxicity is a crucial issue to develop nanodevices useful for biomedical applications. In this context, *Hydra vulgaris* (Cnidaria, Hydrozoa) was used as preliminary *in vivo* model to evaluate diatomite NPs toxicity, in order to compare the *in vitro* results with *in vivo* ones.

6.1 *Hydra Vulgaris* as *in vivo* model for toxicity assessing

Hydra is one of the simplest multicellular organism at the base of the metazoan evolution known, and consists of a tube made up of two connected epithelial cell layers: the outer ectoderm and inner endoderm, separated by an acellular mesoglea layer (Figure 6.1) [9]. As shown in Figure 6.1 A, at the top end of the tube, there is the hypostome composed by a mouth surrounded by 6-8 tentacles that contains the most part of stinging cells (cnidocytes or nematocytes) that let *Hydra* to catch its prey [10]. *Hydra* column has four distinctive sections: the gastric region located between the tentacles and the first (apical) bud; the budding section which produces the buds; the peduncle which is located between the lowest bud and basal disc and the basal disc which is the foot-like formation [11]. This structural complexity, simpler than vertebrates with central nervous system and specialized organs, but more complex than cultured cells, makes *Hydra* comparable to a living tissue whose cells and distant regions are physiologically connected. It possess a simple nervous system which include a nerve net that stretches throughout the body [12]. *Hydra* typically reproduces asexually resulting in the rapid production of a large number of new organisms that can be cultured in a short period of time. *Hydra* is sensitive to a range of pollutants and has been

used as a biological indicator of water pollution [13]. Metal pollutants such as copper, cadmium, and zinc have been tested against different *Hydra* species, and the relative toxicity based on the median lethal concentration (LC50) for all species was ranked from copper, the most toxic, to cadmium with zinc, the least toxic [13]. Drugs and pharmaceuticals targeted at mammalian receptors have also been shown to adversely affect *Hydra*, showing the feasibility to use this aquatic invertebrate to accurately assess the potential toxicological effect of pharmaceuticals entered into natural waters through sewage effluent and landfill leakages [14].

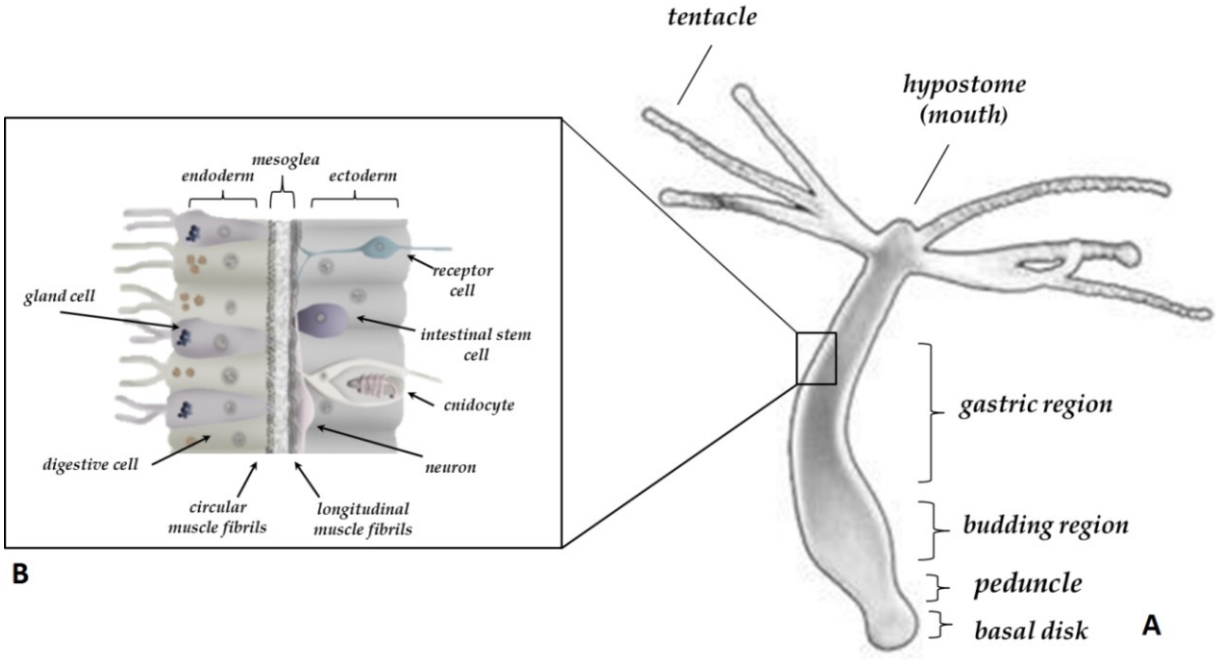

Fig. 6.1. *Anatomical structure of Hydra vulgaris. The inset shows the bilayer structure characterizing the whole body, from the foot to the tentacles, i.e. the ectoderm and endoderm layers separated by the mesoglea. The few specialized cell types differentiated by the interstitial stem cells are shown (neurons, cnidocyte, gland cells).*

Hydra has been used as alternative *in vivo* model, to study the toxicity of different NPs, as well as their uptake and fate [15]. Due to a simple tubular body and being diploblastic, an uniformity exposure of the whole animal to any given NPs by simple soaking is allowed [16, 17]. Several bioassays are available to assess the toxicity of a given substances in terms of acute or sub-lethal toxicity. *Hydra* exposure to different substances may cause (1) alteration of morphological traits and developmental programs, (2) alteration of regeneration or pattern formation; (3) alteration of population growth rates; measuring *Hydra* population growth by asexual reproduction. Moreover, the toxicity can also be analysed on single cells by macerating the hole animal in fixed cell suspension.

6.2 Impact of DNPs on *Hydra* morphology and cellular uptake

The toxicity of substances in *Hydra* is conventionally measured in observing changes in the animal morphology following Wilby's classification ranging from score 10 (normal, elongated tentacles and body), 8 (clubbed or bulbed tentacles), 6 (shortened tentacles), 5 (tulip phase), 2 (loss of osmoregulation) to score 0 (disintegrated) [18]. Scores 10–6 are reversible, sub-lethal indicators while the tulip phase (score 5 and below) is considered irreversible and used as the endpoint for lethality (Figure 6.2) [18, 19].

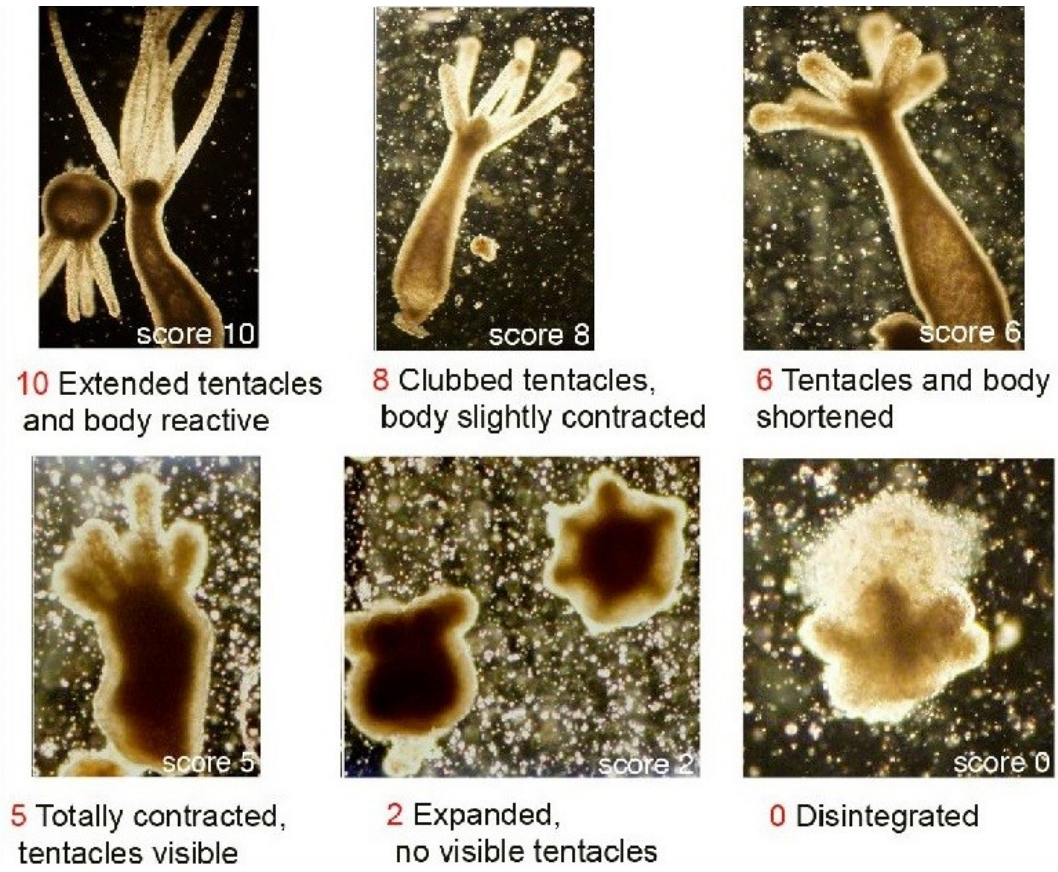

Fig. 6.2. *Score system to assess toxic effects on Hydra based on Wilby's classification [19].*

Toxicity of diatomite NPs in *Hydra* was investigated by monitoring changes in morphology after exposure to the DNPs at increasing incubation times (24, 48 and 72 h) and NP concentrations (0.5 mg/mL, 1 mg/mL, 1.5 mg/mL, 2.5 mg/mL, 3 mg/mL, 3.5 mg/mL, 4 mg/mL). *Hydra Vulgaris* were asexually cultured in physiological solution by the method of Loomis and Lenhoff with minor modifications [20]. The animals were kept at 18 °C and fed three times per week with freshly hatched *Artemia salina nauplii*. All animals were starved 24 h prior to the experiments. For each DNPs concentration twenty polyps were used. Either

control or treated animals were placed into plastic multiwells refreshing the medium every 24 h. The morphophysiological effects of DNPs on *Hydra* were recorded by microscopic examination of each polyp and used to extrapolate the Wilby's score key. A representative *in vivo* images of morphological characterization of *Hydra* after exposure to DNPs is reported in Figure 6.3. Any change in polyp morphology wasn't observed after exposure to DNP concentrations up 4 mg/mL for 72 h; this result corresponds to score 10 of Wilby's classification.

Fig. 6.3. *Morphological in vivo analysis of DNPs effects on Hydra morphology.Scale bar 1 mm.*

These data confirm *in vitro* toxicity results. The transparency of *Hydra* epithelium makes possible to track and localize the fluorescent nanoparticles in the animal body [17]. The internalization of DNPs in *Hydra* was evaluated by *in vivo* fluorescence microscopy analysis, after labelling DNPs by Alexa Fluor-488® (DNPs*). Ten living *Hydra* were treated with DNPs* (3.5 mg/mL) up to 72 h. Bright-field and fluorescence images of *Hydra* polyps treated with DNPs* for 24 (C, D) and 72 h (E, F) are reported in Figure 6.4; Figures 6.4 A and B show an untreated animal as control. In all figures, the foot is on the lower part of the panel, while a crown of tentacles surrounds the mouth. The image taken after 24 h (D) shows an intense fluorescence of DNPs, distributed in the whole body and confined to the outer ectoderm. After 72 h (F) of incubation the DNPs were mainly localized in the inner endodermal cells, due to inter-epithelial migration of free or cell- containing nanoparticles between the two cell layers [19]. These preliminary *in vivo* results are in agreement with the *in vitro* data, confirming that DNPs could be used as safe and biocompatible nanocarrier for long incubation times and high concentrations.

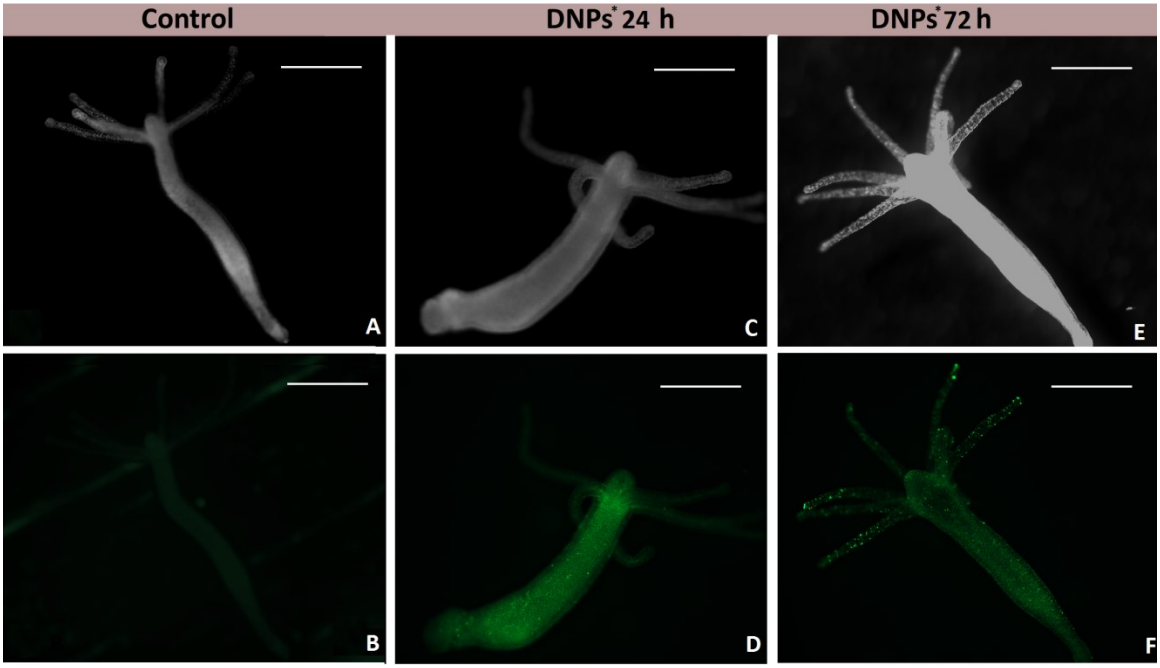

Fig. 6.4. *In vivo fluorescence imaging of Hydra polyps treated with labelled DNPs (3.5 mg/mL) for different incubation times. Scale bars 1 mm. The fluorescence pattern appears as rather uniform after 24 h of incubation, while at 72 h it appears as granulates covering most of body regions. They might represent storage vacuoles, as it has been shown for other fluorescent nanoparticles [16, 19].*

References

1. R. Cheng, F. Feng, F. Meng, C. Deng, J. Feijen, Z. Zhong, *J. Controlled Release*, 2011, **1**, 2–12.
2. C. Huang, K.G. Neoh, L. Wang, E. T. Kang, B. Shuter, *Contrast Media Mol. Imaging*, 2011, **4**, 298–307.
3. J. Pan, D. Wan, J. Gong , *Chem. Commun.*, 2011, **12**, 3442–3444.
4. L Yildirimer, N. T. Thanh, M. Loizidou, A. M. Seifalian, *Nano today*, 2011,**6**, 585–607.
5. L. M. Bimbo, L. Peltonen, J. Hirvonen, H. A. Santos, *Curr. Drug Metab*., 2012, **13**, 1068–1086.
6. M. A. Shahbazi, P. V. Almeida, E. Mäkilä, M. Kaasalainen, J. Salonen, J. Hirvonen, H. A. Santos, *Biomaterials*, 2014, **35**, 7488–7500.
7. T. Yu, A. Malugin, H. Ghandehari, *ACS nano*, 2011, **7**, 5717–5728.
8. A. Zoroddu, M. Medici, S. Ledda, A. Marina Nurchi, V. Lachowicz, M. Peana, *Current Medicinal Chem.*, 2014, **21**, 3837–3853.
9. L. B. Slobodkin, P. E. Bossert, *Ecology and Classification of North American Freshwater Invertebrates*, San Diego: Academic Press, 2001.
10. R. E. Steele, *Develop. biology,* 2002, **248**, 199–219.
11. D. A. Holdway, K. Lok, M. Semaan, *Environ. Toxicol.*, 2001,**16**, 557–565.
12. M. Sakaguchi, A. Mizusina, Y. Kobayakawa, *J. Comp. Neurol,* 1996, **373**, 41–54.
13. B. Quinn, F. Gagné, C. Blaise, *Int. J. Develop. Biology*, 2012, **56**, 613–625.

14. D. Pascoe, W. Karntanut, C. T. Müller, *Chemosphere*, 2003, **51**, 521–528.
15. A. Ambrosone, L. Mattera, V. Marchesano, A. Quarta, A. S. Susha, A. Tino, A. L. Rogach, C. Tortiglione, *Biomaterials*, 2012, **33**, 1991–2000.
16. C. Tortiglione, A. Quarta, M. A., Malvindi, A. Tino, T. Pellegrino, *PLoS ONE,* 2009, **4**, 7698.
17. C. Tortiglione, A. Quarta, A. Tino, L. Manna, R. Cingolani, T. Pellegrino, *Bioconjug Chem.*, 2007, **18**, 829–835.
18. O. K. Wilby, J. M. Tesh, *Toxicol. in vitro*, 1990, **4**, 582–583.
19. V. Marchesano, Y. Hernandez, W. Salvenmoser, A. Ambrosone, A. Tino, B. Hobmayer, J. M. de la Fuente, C. Tortiglione, *ACS Nano*, 2013, **7**, 2431–2442.
20. W. F. Loomis, H. M. Lenhoff, *J. Exp. Zoology*, 1956, **132**, 555–573.

7 CONCLUSIONS

The development of organic–inorganic hybrids with controlled morphology at the nanometer scale, represented a triumphant class of materials for progress of healthcare devices technology. Porous silicon is an appealing nanostructured material, largely used in biomedical applications, due to the ease of tuning its properties, such as pore morphology, photonic properties, biocompatibility, biodegradation and surface chemistry. This PhD thesis work was focused on the realization of porous silica based devices, paying particular attention to functionalization strategies, in order to obtain advanced systems for biosensing and drug delivery applications. Porous silicon structures are widely used by far as optical transducers for biosensors development in lot of laboratories, and even commercial applications. However, the main drawback of these easy-to-produce and sensitive devices is their low chemical stability in aqueous solutions, actually used in biochemical experiments. The realization of DNA-PSi devices with great stability, fast response time, high sensitivity and specificity was demonstrated in the first part of this PhD thesis work. Two common routes of passivation/functionalization by grafting alkylsilanes through the formation of Si–O–Si bonds between silanol groups induced on the oxidized PSi surface and hydrolysed organosilane molecules of APTES or APDMES was investigated. Both compounds, but with some differences, form a thin film on PSi surface, which can effectively protect the porous support against corrosion on exposure to aqueous solution. It is well known, that APTES can polymerize forming a multi-layered interface, while APDMES cannot do it. Despite this not negligible distinction, both silane-modified PSi devices shown good chemical resistance to reagents used for *in situ* synthesis. In particular, APDMES passivation, due to less steric hindrance of the pores, resulted in a better oligonucleotide (ON) functionalization quality with respect to APTES in case of mesoporous structures. Finally, hybridization to a target sequence of oligonucleotide synthetized on APDMES modified porous silica optical structure was demonstrated by complementary optical techniques, such as spectroscopic reflectivity and fluorescence microscopy. The development of DNA label-free optical biosensors through *in situ* synthesis of a 13-mer polythymine ON strand, deprotection and hybridization with a complementary ON, was successfully demonstrated, opening the prospective of PSi solid phase ON synthesis without any restriction on the ON sequence, giving more general significance to the proposed methodology. Starting from these results, a stable sensitive and reversible PSi-aptasensor realized by *in situ* synthesis for label-free optical detection of human thrombin, was developed. Thrombin is an allosteric serine protease with a crucial roles

in physiological and pathological coagulation, and also involved in various diseases, such as Alzheimer's disease and cancer. Anti-thrombin aptamer (TBA) was synthetized in silanized macroporous PSi structure which, due to an average pore size of about 140 nm allowed a correct synthesis of the bioprobe with proper yield. In order to enable thrombin biomolecular recognition, TBA was deprotected by dry ammonia in methanol thus preserving the structural integrity of the PSi matrix. The sensing mechanism based on high affinity between TBA aptamer and α-thrombin was monitored by label-free method based on spectroscopic reflectometry, showing a limit of detection of 4.0 ± 0.9 nM and high sensitivity for the thrombin, comparable to the other DNA devices realized using more complicated and expensive technologies. In addition, the reversibility of PSi-aptasensor was also demonstrated, proving the reusability of biosensor for subsequent sensing event, through its simple washing with heated water at melting temperature (53 °C). The encouraging results obtained suggest the potentiality to develop a wide range of stable and high sensitive PSi aptasensors by *in situ* synthesis for human disease early diagnosis. Porous silicon is also one of the most commonly used material for the development of drug-delivery systems. In recent years, there was a need to explore alternative porous silica materials for drug-delivery applications in order to address some disadvantages of the synthetic porous materials, finding in diatomite a great surrogate. Diatomite is a natural nanostructured silica material of sedimentary origin formed by fragments of diatom skeletons, characterized by chemical inertness, thermal stability, high surface area, non-toxicity and biocompatibility. Although, its peculiar properties, diatomite has been explored for a large number of applications ranging from photonics to water filtration, but it is underestimated in nanomedicine. In the second part of this PhD thesis work, diatom frustules reduced to nanoparticles (NPs) were explored, for the first time, as potential nanocarriers for drug delivery applications. A procedure based on mechanical and chemical treatments for preparing diatomite NPs (DNPs) with an average size of 300 nm and to make them safer for medical applications, was developed. The nanosize of the DNPs, obtained after the processing of the raw diatomite powder was evaluated by scanning electron microscopy (SEM), transmission electron microscopy (TEM), and dynamic light scattering (DLS) analysis. The variation in the chemical composition of diatomite powder before and after purification treatment was evaluated by photoluminescence (PL), Fourier transform infrared spectroscopy (FTIR) and energy dispersive X-ray spectroscopy (EDS) analyses, confirming the improvement of the silica nanopowder quality due the removal of impurities. Preliminary tests of cytotoxicity and cellular uptake demonstrated the biocompatibility of the DNPs and their capability to penetrate inside cancer cells. Since the

silica surface of diatomite is covered by silanol (SiOH) groups, it can be easily modified with functional reactive groups ($-NH_2$, $-COOH$, $-SH$, and $-CHO$) for the conjugation of biomolecules in order to prepare advanced devices. Two different functionalization approaches based on covalent bond for bioengineered DNPs fabrication were developed, in order to transport therapeutic molecules (smoll interfering RNA (siRNA) and poorly water-soluble anticancer drug sorafenib) into cancer cells. The first functionalization process based on covalent bond between DNPs' surface and siRNA-peptide complex, demonstrated an effective uptake of the engineered siRNA nanovectors into human epidermoid carcinoma cells. An enhancement of gene silencing in cancer cells due to siRNA delivered by DNPs was also demonstrated. In the second functionalization approach, a dual-biofunctionalization based on covalent conjugation of polyethylene glycol (PEG) and cell penetrating peptide (CPP) onto the NPs' surface, was developed. An improvement of the DNPs' physicochemical properties, biocompatibility, cellular uptake and sorafenib drug release in aqueous solution, was demonstrated. After these positive *in vitro* results, *Hydra vulgaris* was used as simple model for preliminary *in vivo* studies of DNPs toxicity and cellular uptake, confirming the safety and the potentiality of diatomite NPs as new nanocarriers. The interesting experimental results reported in this PhD work demonstrate the potentiality of synthetic and natural porous silica as versatile material for the realization of healthcare smart systems.